

**IPL**

**escola superior de tecnologia e gestão**  
instituto politécnico de leiria

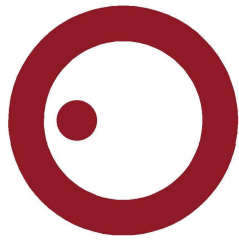
Polytechnic of Leiria  
School of Technology and Management  
Department of Electrical and Electronics Engineering  
Master in Electrical and Electronic Engineering – Electronics and  
Telecommunications

**ELECTROMAGNETIC LOG SHIELD FOR  
ROADSIDE APPLICATION**

**BRUNO ALVES TRIBOVANE**

Leiria, December of 2021

This page is intentionally left blank.



**IPL**

**escola superior de tecnologia e gestão**  
instituto politécnico de leiria

Polytechnic of Leiria  
School of Technology and Management  
Department of Electrical and Electronics Engineering  
Master in Electrical and Electronic Engineering – Electronics and  
Telecommunications

**ELECTROMAGNETIC LOG SHIELD FOR  
ROADSIDE APPLICATION**

**BRUNO ALVES TRIBOVANE**

Number: 2182462

Dissertation supervised by Professor Rafael F. S. Caldeirinha ([rafael.caldeirinha@ipleiria.pt](mailto:rafael.caldeirinha@ipleiria.pt)).

Leiria, December of 2021

This page is intentionally left blank.



## ACKNOWLEDGMENTS

---

First and foremost, I would like to express my gratitude to my supervisor Professor Rafael Caldeirinha, for proactively opening the doors to knowledge by granting me the opportunity to do research and for expertly guiding me over the course of this dissertation.

I'm also thankful to the School of Technology and Management of Polytechnic of Leiria and the Instituto de Telecomunicações - Antennas & Propagation Leiria (IT-AP Lr), for providing materials, access to facilities and necessary radio equipment.

I would like to recognize the help and camaraderie from my colleagues from the IT-AP Lr group, as they made possible to ease the difficulties felt throughout this work.

I also want to extend my sincere thanks to my family for their invaluable support over the years and finally, I want to thank my friends for their devotion, aptitude, vivacity, impartiality, dependability, optimism and politeness, which allowed me to maintain assertiveness and attain success.

This work is partially funded by the European Regional Development Fund (FEDER), through the Competitiveness and Internationalization Operational Programme (COMPETE 2020) of the Portugal 2020 framework project Hybrid Log Shield (*Projeto em copromoção n.o 33691*); and by the Portuguese Government, Foundation for Science and Technology, FCT, through the financial support provided under UID/EEA/50008/2021.

This page is intentionally left blank.

## ABSTRACT

---

In this dissertation, a highly sustainable barrier made of circular section timber of low industrial processing, is presented. This wooden structure allows the control of electromagnetic (EM) spectrum by fine-tuning the barrier's intrinsic parameters to shape shielding effectiveness (SE) in order to improve either EM shielding or transparency.

An algorithm is developed in MATLAB to design and generate the desired structural geometry within a simulation environment (CST MW), with the implementation of surface roughness and bending on the trunks. Simulations are performed at the frequency range of 0.3 to 10 GHz with the parametrisations such as the spacing between centre of poles, radius and moisture content (MC). The proposed real scale barrier prototype is assembled in the anechoic chamber and measurements are then performed at different transmitter (TX) and receiver (RX) antenna angles with both vertical and horizontal polarisation to better understand this structure's impact on radio propagation.

From this work, it was demonstrated that the wooden barrier's simulation and measurement results present a good agreement and how the shielding efficiency can be tailored by optimising the radius and spacing at frequencies of commercial interest.

**Keywords:** Wooden barrier, Shielding effectiveness, Structure modelling, Prototype measurement

This page is intentionally left blank.

## TABLE OF CONTENTS

---

Acknowledgments	i
Abstract	iii
Table of Contents	v
List of Figures	ix
List of Tables	xiii
List of Acronyms	xv
1 INTRODUCTION	1
1.1 Background study and motivation . . . . .	1
1.2 Aims and objectives . . . . .	2
1.3 Dissertation structure . . . . .	2
2 LITERATURE REVIEW	5
2.1 Introduction . . . . .	5
2.2 State of the art . . . . .	5
2.3 Moisture Content . . . . .	6
2.4 Permittivity . . . . .	7
2.5 Radio transmission and channel properties . . . . .	7
2.5.1 Radio signal and frequency domain . . . . .	7
2.5.2 Transmission parameters . . . . .	9
2.5.3 Near and Far-field . . . . .	10
2.6 S-Parameters . . . . .	11
2.7 Electromagnetic shielding effectiveness . . . . .	12
2.8 Interim conclusions . . . . .	13
3 SCRIPT DEVELOPMENT FOR BARRIER MODELLING	15
3.1 Introduction . . . . .	15
3.2 Environment settings and initialisation . . . . .	15
3.3 Modelling process flow . . . . .	16
3.3.1 Material definition . . . . .	18
3.3.2 Structural conception . . . . .	19
3.3.3 Surface roughness implementation . . . . .	21
3.3.4 Trunks' bending procedure . . . . .	22
3.3.5 Model's electromagnetic characteristics . . . . .	23

TABLE OF CONTENTS

3.4	Interim conclusions . . . . .	24
4	MODEL CHARACTERISATION AND ASSESSMENT	27
4.1	Introduction . . . . .	27
4.2	Early model design trials . . . . .	27
4.2.1	Structure sample analysis . . . . .	28
4.2.2	Large structure analysis . . . . .	29
4.3	Parametrisation study of an infinite barrier . . . . .	31
4.3.1	Trunks' spacing and radius analysis in a single layer . . . . .	31
4.3.1.1	Parametrisation of trunks' spacing and radius for increased transparency . . . . .	33
4.3.2	Double layer parametric study . . . . .	36
4.3.3	Triple layer parametric study and layers comparison . . . . .	38
4.3.4	Moisture content, surface roughness, trunks' bending and other parameters assessment . . . . .	44
4.4	Interim conclusions . . . . .	46
5	MEASUREMENT SETUP AND BARRIER VALIDATION	49
5.1	Introduction . . . . .	49
5.2	Barrier assembly and environment preparation . . . . .	49
5.3	Barrier evaluation and discussion . . . . .	51
5.3.1	Measurement post-processing . . . . .	52
5.3.2	Measurement results on normal incidence . . . . .	53
5.3.3	Measurement results on a multi-angular setting . . . . .	56
5.4	Interim conclusions . . . . .	60
6	CONCLUSION	63
6.1	Introduction . . . . .	63
6.2	Dissertation review . . . . .	63
6.3	Contributions to science . . . . .	64
6.4	Future work . . . . .	65
	BIBLIOGRAPHY	67
	<b>Appendices</b>	
A	SCRIPT FOR AUTOMATIC BARRIER MODELLING	73
A.1	Main code to generate the model in CST . . . . .	73
A.2	Material generation . . . . .	78
A.3	Trunks and irregularities definition . . . . .	81
A.4	Trunks' bending . . . . .	86

B RECORDED STATS OF WOODEN POLES	89
C FREE SPACE MEASUREMENTS	91
D NORMALISED BARRIER MEASUREMENTS	93
DECLARATION	99

This page is intentionally left blank.



## LIST OF FIGURES

---

Figure 1	Methods to acquire <b>MC</b> from wood (image extracted from the work presented in [1]). . . . .	6
Figure 2	Conversion of time domain signals to frequency domain (image extracted from [2]). . . . .	8
Figure 3	Diagram depicting a radio transmission. . . . .	9
Figure 4	Far-field and near-field regions generated by an antenna (image extracted from [3]). . . . .	11
Figure 5	Two port network (image extracted from [4]). . . . .	11
Figure 6	Defined environment setup in <b>CST</b> . . . . .	16
Figure 7	Flowchart depicting the developed script process for model creation. . . . .	17
Figure 8	Relation between real part of permittivity, <b>MC</b> and frequency with data taken from [5]. . . . .	18
Figure 9	Relation between loss tangent, <b>MC</b> and frequency with data taken from [5]. . . . .	19
Figure 10	Top view of a trunk depicting the attributed <b>MC</b> values. . .	19
Figure 11	Permittivity related curves of a material with $MC = 10\%$ and curve fitting in <b>CST</b> . . . . .	20
Figure 12	Generated structure containing trunks partially erased to retain trunk's spacing periodicity. . . . .	21
Figure 13	Trunk with marked separations. . . . .	21
Figure 14	Surface roughness implemented on a trunk. . . . .	23
Figure 15	Preview of a trunk bending over a virtual cylinder. . . . .	24
Figure 16	Ports placed located parallel to the barrier showing polarisation vectors. . . . .	25
Figure 17	Four case scenarios of a 3x3 structural sample. . . . .	28
Figure 18	Simulation results of the four case scenarios. . . . .	29
Figure 19	A 3x9 barrier where spacing is parametrised. . . . .	30
Figure 20	Schematic depicting the configuration used on the 3x9 structure. . . . .	30
Figure 21	Simulation results of a 3x9 structure with spacing between trunks parametrised from 160 to 180 mm. . . . .	30
Figure 22	Top view of the structural sample consisting of one layer (a) and the respective diagram (b). . . . .	31

LIST OF FIGURES

Figure 23	Simulation results with radius parametrised in a single layer composed of trunks with spacing between centre of trunks of 180 mm. . . . .	32
Figure 24	Simulation results with spacing between centre of trunks parametrised in a single layer composed of trunks with radius of 60 mm. . . . .	33
Figure 25	Simulation results with parametrisation of spacing between centre of trunks in a single layer composed of trunks with radius of 60 mm. . . . .	34
Figure 26	Simulation results with parametrisation of radius in a single layer with spacing between centre of trunks set to 220 mm. . . . .	35
Figure 27	Simulation results with parametrisation of radius in a single layer with spacing between centre of trunks set to 300 mm. . . . .	35
Figure 28	Top view of the structural sample consisting of two layers with no offset (a) and the same setup but with a layer offset (b). . . . .	37
Figure 29	Simulation results with parametrisation of trunks' radius and layer offset in a double layer configuration with the spacing between centre of trunks' set to 180 mm. . . . .	38
Figure 30	Simulation results with parametrisation of spacing between centre of trunks and layer offset in a double layer configuration with the trunks' radius set to 60 mm. . . . .	39
Figure 31	Top view of the structural sample consisting of three layers with no offsets (a), layer 2 with offset of 30 mm and layer 3 with offset of 60 mm (b), layer 2 with offset of 45 mm and layer 3 with offset of 90 mm (c), layer 2 with offset of 90 mm and layer 3 with no offset (d). . . . .	40
Figure 32	Simulation results with parametrisation of trunks' radius in a triple layer configuration with the spacing between centre of trunks' set to 180 mm. . . . .	40
Figure 33	Simulation results with parametrisation of spacing between centre of trunks in a triple layer configuration with the trunks' radius set to 60 mm. . . . .	41
Figure 34	Simulation results with parametrisation of layers offset in a triple layer configuration with the spacing between centre of trunks' set to 180 mm and radius of 60 mm. . . . .	43
Figure 35	Simulation results showing the comparison of number of trunk layers in the structure. . . . .	44
Figure 36	Simulation results showing the comparison of structures with different MC ranges in the trunks. . . . .	45

Figure 37	Simulation results showing the comparison of structures with diverse surface roughness parametrisations. . . . .	46
Figure 38	Five cases of unique degrees of bending on structures. . . . .	46
Figure 39	Simulation results showing the comparison of structures with different degrees of trunk bending. . . . .	47
Figure 40	Log barrier prototype assembled in the anechoic chamber. . . . .	50
Figure 41	Measurement geometry and setup. . . . .	50
Figure 42	Attenuation caused by used cables before the final setup. . . . .	51
Figure 43	The assembled barrier and equipment from the perspective of TX (a) and RX (b). . . . .	52
Figure 44	Setup for free space measurements. . . . .	52
Figure 45	Free space measurement in a multi-angular setup at 2.4 GHz, with antennas horizontally (a) and vertically (b) polarised. . . . .	53
Figure 46	Simulation results versus measurement results with both horizontal and vertical polarisation of a single layer with spacing between centre of trunks of 160 mm. . . . .	54
Figure 47	Simulation results versus measurement results with both horizontal and vertical polarisation of a single layer with spacing between centre of trunks of 180 mm. . . . .	54
Figure 48	Simulation results versus measurement results with both horizontal and vertical polarisation of a single layer with spacing between centre of trunks of 200 mm. . . . .	55
Figure 49	Graphs presenting normalised measurement results at 2.4 GHz with antennas horizontally polarised and spacing between centre of trunks of (a) 160, (c) 180 and (e) 200 mm, and antennas vertically polarised with spacing of (b) 160, (d) 180 and (f) 200 mm. . . . .	57
Figure 50	Graphs presenting normalised measurement results with antennas horizontally polarised and spacing between centre of trunks of 180 mm, at frequencies of (a) 1.8, (b) 2.4, (c) 3.7 and (d) 5.9 GHz. . . . .	58
Figure 51	CDF of normalised measurements with spacing between centre of trunks of 160 mm and antennas at angles ranging from $-20^\circ \leq \theta_1 \leq 20^\circ$ and $-20^\circ \leq \theta_2 \leq 20^\circ$ . . . . .	59
Figure 52	CDF of normalised measurements with spacing between centre of trunks of 180 mm and antennas at angles ranging from $-20^\circ \leq \theta_1 \leq 20^\circ$ and $-20^\circ \leq \theta_2 \leq 20^\circ$ . . . . .	59
Figure 53	CDF of normalised measurements with spacing between centre of trunks of 200 mm and antennas at angles ranging from $-20^\circ \leq \theta_1 \leq 20^\circ$ and $-20^\circ \leq \theta_2 \leq 20^\circ$ . . . . .	60

Figure 54	Free space measurement in a multi-angular setup with antennas horizontally polarised at 1.8 (a), 2.4 (b), 3.7 (c) and 5.9 GHz (d). . . . .	91
Figure 55	Free space measurement in a multi-angular setup with antennas vertically polarised at 1.8 (a), 2.4 (b), 3.7 (c) and 5.9 GHz (d). . . . .	92
Figure 56	Graphs presenting normalised measurement results at 1.8 GHz with antennas horizontally polarised and spacing between centre of trunks of 160 (a), 180 (c) and 200 mm (e), and antennas vertically polarised with spacing of 160 (b), 180 (d) and 200 mm (f). . . . .	94
Figure 57	Graphs presenting normalised measurement results at 2.4 GHz with antennas horizontally polarised and spacing between centre of trunks of 160 (a), 180 (c) and 200 mm (e), and antennas vertically polarised with spacing of 160 (b), 180 (d) and 200 mm (f). . . . .	95
Figure 58	Graphs presenting normalised measurement results at 3.7 GHz with antennas horizontally polarised and spacing between centre of trunks of 160 (a), 180 (c) and 200 mm (e), and antennas vertically polarised with spacing of 160 (b), 180 (d) and 200 mm (f). . . . .	96
Figure 59	Graphs presenting normalised measurement results at 5.9 GHz with antennas horizontally polarised and spacing between centre of trunks of 160 (a), 180 (c) and 200 mm (e), and antennas vertically polarised with spacing of 160 (b), 180 (d) and 200 mm (f). . . . .	97

## LIST OF TABLES

---

Table 1	Roughness parameters defined in the modelling script . . . .	27
Table 2	Bending parameters defined in the modelling script . . . . .	28
Table 3	Simulation results with data taken from Figure 23, at frequencies of commercial interest, where radius is parametrised in a single layer composed of trunks with spacing between centre of trunks of 180 mm. . . . .	32
Table 4	Simulation results with data taken from Figure 24, at frequencies of commercial interest, where spacing between centre of trunks is parametrised in a single layer composed of trunks with radius of 60 mm. . . . .	34
Table 5	Simulation results from the parametrisation of trunks' spacing and radius for increased EM transparency, at frequencies of commercial interest. . . . .	36
Table 6	Simulation results with data taken from Figure 29, at frequencies of commercial interest, where trunks' radius and layer offset are parametrised in a double layer configuration with the spacing between centre of trunks' set to 180 mm. . . . .	37
Table 7	Simulation results with data taken from Figure 30, at frequencies of commercial interest, where spacing between centre of trunks and layer offset are parametrised in a double layer configuration with the trunks' radius set to 60 mm. . . . .	39
Table 8	Simulation results with data taken from Figure 32, at frequencies of commercial interest, where trunks' radius is parametrised in a triple layer configuration with the spacing between centre of trunks' set to 180 mm. . . . .	41
Table 9	Simulation results with data taken from Figure 33, at frequencies of commercial interest, where spacing between centre of trunks is parametrised in a triple layer configuration with the trunks' radius set to 60 mm. . . . .	42
Table 10	Simulation results with data taken from Figure 34, at frequencies of commercial interest, where layers offset are parametrised in a triple layer configuration with the spacing between centre of trunks' set to 180 mm and radius of 60 mm. . . . .	42

LIST OF TABLES

Table 11	Simulation results with data taken from Figure 35, at frequencies of commercial interest, where the number of layers in the structure are compared. . . . .	43
Table 12	Mean SE acquired from measurements on normal incidence with spacing between centre of trunks from 160 to 200 mm with antennas vertically and horizontally polarised. . . . .	55
Table 13	RMSE based on mean SE between simulations and measurements on normal incidence with spacing between centre of trunks from 160 to 200 mm with antennas vertically and horizontally polarised. . . . .	56
Table 14	CDF of normalised measurements at commercial frequencies with antennas at angles ranging from $-20^\circ \leq \theta_1 \leq 20^\circ$ and $-20^\circ \leq \theta_2 \leq 20^\circ$ . . . . .	61
Table 15	Height assessment over a batch of thirty wooden poles. . . . .	90

## LIST OF ACRONYMS

---

CDF Cumulative Distribution Function.  
CST Computer Simulation Technology.

DUT Device Under Test.

EM Electromagnetic.

FSPL Free Space Path Loss.

FSS Frequency Selective Surface.

HLS Hybrid Log Shield.

LoS Line-of-Sight.

MC Moisture Content.

MWS Microwave Studio.

RMSE Root Mean Square Error.

RX Receiver.

SE Shielding Effectiveness.

SI Internation System of Units.

TX Transmitter.

VBA Visual Basic for Applications.

VNA Vector Network Analyser.

This page is intentionally left blank.



## INTRODUCTION

---

### 1.1 BACKGROUND STUDY AND MOTIVATION

Currently on motorways, the existing barriers serve only as a solution to mitigate acoustic noise generated by vehicles near residential areas. Most of these barriers are composed of non-ecological materials, such as, concrete, clay brick, plastic or metal, which also contributes to a negative visual impact. In the particular case of sub-urban and rural areas, it would be preferable that acoustic barriers were made of natural resources, such as wood trunks, which brings the possibility to merge the structure with the landscape [6].

The use of a multi-layered timber logs as sustainable acoustic noise mitigation solutions have been proposed [7, 8, 9, 10]. The use of sonic crystal propagation theory for acoustic waves, allowed a reduction of the signal level for more than 14 dB at frequencies around 3 to 4 kHz. Mitigation measures of noise are detailed in [9], which are often used along main roads, where the effects on human health are well understood to date.

On the other hand, society awareness to **Electromagnetic (EM)** exposure has been progressively raised due to the increasing number mobile radio devices and the evolution of multimedia applications. To this extent, the importance of **EM** shielding barriers has increased in the last decade, as a road **EM** fencing is thought as an exterior structure designed to protect sensitive land users or (autonomous driving) vehicles from EM noise pollution, allowing C-V2X communications as foreseen in the IEEE 802.11p and 3GPP Releases 16 and 17 networks with reduced interference [11, 12, 13].

The acoustic and **EM** shielding capabilities of such barriers, along with its ecological and low cost characteristics, makes it a very pleasant solution to be assembled in existing and new road infrastructure, to protect the surrounding environment of unwanted noise and **EM** pollution, while ensuring excellent wind permeability performance [14, 15].

## 1.2 AIMS AND OBJECTIVES

In this dissertation, an innovative and highly sustainable barrier made of circular section timber of low industrial processing, is presented as a hybrid (acoustic and electromagnetic) solution, a subject developed within the scope of the project [Hybrid Log Shield \(HLS\)](#). The proposed barrier is a relatively novel concept, built upon the work presented in [16] which presents the state-of-the-art of log based electromagnetic barriers, consists of a multi-layer configuration of periodically arranged poles of *Pinus Pinaster* where the influence of trunks' [Moisture Content \(MC\)](#), spacing, radius and the structure's imperfections on the [Shielding Effectiveness \(SE\)](#) and number of layers are studied.

The main objectives of this work are described as follows:

- Development of a barrier modelling algorithm in MATLAB;
- Characterisation of the structure intrinsic parameters in [Computer Simulation Technology \(CST\) Microwave Studio \(MWS\)](#);
- Measurement setup and procedure of a real scale barrier prototype;
- Dissemination of the work being performed in conferences with relevant scientific reputation.

## 1.3 DISSERTATION STRUCTURE

This document is divided in 6 chapters with the following structure:

Chapter 1 aims to situate this dissertation, with a brief explanation of motivation and objectives of the proposed barrier, following by the dissertation layout.

Chapter 2 presents the current state of the art on [EM](#) characteristics of wood, along with the radio propagation fundamentals and the acquisition of [SE](#) of a structure.

Chapter 3 details the development of a script for automatic barrier modelling with a thorough explanation on diverse implementations such as surface roughness and bending on trunks.

Chapter 4 presents the structure's design and characterisation within the simulation environment, followed by the analysis of simulation results.

Chapter 5 aims to explain the measurement setup and process, along with the measurement results of the proposed prototype, with statistical analysis at frequencies of commercial interest.

Chapter 6 is dedicated to the conclusions and final remarks of the presented work, with the report of contributions to the scientific community and proposals for future work.

This page is intentionally left blank.

## LITERATURE REVIEW

---

### 2.1 INTRODUCTION

This chapter will address the current literature on electromagnetic barriers, the principles to characterise the properties of wood, such as acquisition of moisture content within wood and the dielectric properties of a material. The basis behind radio propagation will also be presented, mainly the components of a radio transmission system, transformation of time signals to the frequency domain and radio wave settings. The S-parameters of a linear network and the SE of a structure are also presented.

### 2.2 STATE OF THE ART

The current literature presents large scale electromagnetic barriers made of metal, concrete or wood, with the purpose of shielding a defined area from the radiation source. The authors in [17] present a solution composed of reinforced concrete to reduce EM fields of industrial frequency, where it is observed the behaviour of a Faraday cage by the barrier, as it reflects and absorbs part of the energy of EM fields due to the steel reinforcements within it. In [18], a solution composed by a metallic fence of galvanized steel wires with a diameter of 1 cm and height of up to 24 m to shield EM fields, is proposed. Here it is visualised that the increase of height provided the highest shielding, with high frequency electric field strength being suppressed from 50 V/m to below 28 V/m. Regarding log-based electromagnetic barriers, it is viewed in [16] the simulation and on-site measurement of SE of a structure composed of four layers of *Pinus Pinaster* at the frequency range of 0.7 to 2.5 GHz, where the results present a good agreement between simulation and measurement, with a Root Mean Square Error (RMSE) of 7.2659 at frequencies of commercial interest such as 0.9, 1.575, 2.1 and 2.4 GHz, being 17.55 dB the mean attenuation obtained from the measurement at the specified frequencies. Additionally, it is observed how manipulating the structure geometry and spacing can result in spectrum shaping, which can find use in specific application and deployment scenario.

## 2.3 MOISTURE CONTENT

Wood is a porous material and its hygroscopic nature allows the reception of water in the air [1]. The humidity percentage within the wood is defined by **MC**, and this relates the weight of water with the weight of the material.

The diverse methods to extract **MC** values from wood are presented in Figure 1, where within indirect methods, in short, the capacitive and microwave method consists in applying a frequency signal which is transmitted and received through electrodes inserted in the wood. The electrical resistance method is similar to the previous case, but only the resistance is measured. Radiometric method measures the deceleration caused by the H-atoms in water when striking atoms with the use of radiation-counter tubes. The spectrometric method is determined by how much light can be absorbed by water. Colour-reaction method is performed with the insertion of an indicator paper in a hole drilled into the wood, which changes colour according to **MC**, and finally, the sorption isotherms method involves measurements with capacitative hygrometers.

From the direct methods, the distillation/extraction method consists in heating a sample extracted from wood and measuring the generated condensation. Kiln-drying/oven-drying method is the most widely used which is performed by weighing a sample of wood before being dried at a temperature of  $103^{\circ}C \pm 2K$  until its mass becomes constant. Here, **MC** can be calculated in Equation 1, where  $W_g$  is the total weight of wood and  $W_d$  is the oven-dry weight of the wood [19].

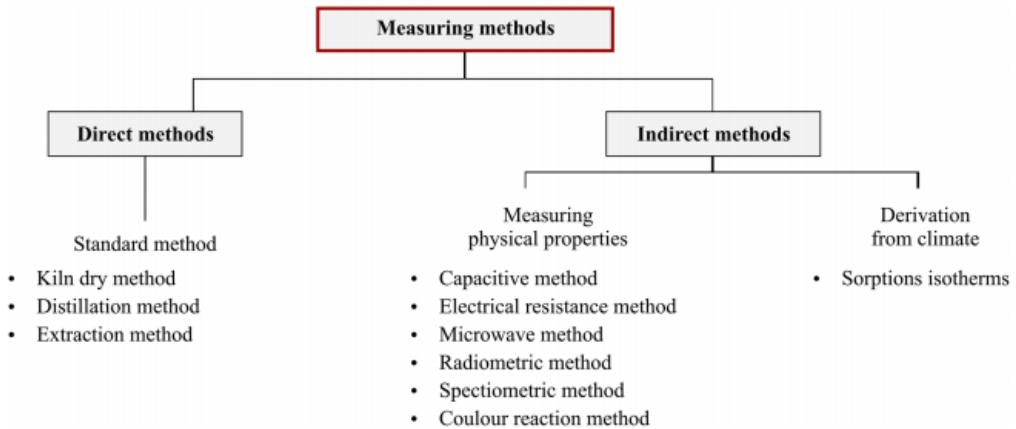


Figure 1: Methods to acquire **MC** from wood (image extracted from the work presented in [1]).

$$W_g = W_d \left( 1 + \frac{MC}{100} \right) \quad (1)$$

## 2.4 PERMITTIVITY

The dielectric properties of a material is related to its permittivity, a quantity which describes reflection of EM waves, energy absorption and attenuation of wave energy [20]. Within the frequency domain, a material's dielectric parameters can be determined through complex relative permittivity [5], as defined in Equation 2.

$$\epsilon^* = \epsilon' - j\epsilon'' = \epsilon'(1 - jtg\delta) \quad (2)$$

Where:

$\epsilon^*$  is the complex relative permittivity;

$\epsilon'$  is the relative permittivity (real part);

$\epsilon''$  is the loss factor (imaginary part);

$j = \sqrt{-1}$ ;

$tg\delta$  is the loss tangent.

Furthermore, the loss tangent specify the dissipation of electric energy [21], and it can be expressed according to Equation 3.

$$tg\delta = \frac{\epsilon''}{\epsilon'} \quad (3)$$

## 2.5 RADIO TRANSMISSION AND CHANNEL PROPERTIES

Wireless communications are designed with the elements that compose the radio circuit such as Transmitter (TX), Receiver (RX) and the medium between those. To ensure that the radio signal is transmitted and received effectively, it must be devised a radio system to fulfil the minimum conditions which allows a decent signal reception [22].

## 2.5.1 Radio signal and frequency domain

The radio wave propagated in a medium can be characterised by three parameters:  $\epsilon$ ,  $\mu$  and  $\sigma$  (permittivity, permeability and conductivity respectively) [23]. These waves are subject to phenomena that introduces signal losses such as diffraction, reflection, refraction, which can be interpreted by Huygens–Fresnel principle [24], and dispersion [25].

Generally, radio waves are represented by sinusoids and are subject to modulation [26], but in practice, EM signals with diverse frequencies exists in many environments, which makes the determination of the signal from a specific source difficult in scenarios such as when using an oscilloscope, with the representation of all captured signals on a time axis. The Fourier transform allows the conversion of signals in time domain to frequency domain, which eases the calculation and visualisation of all signals [2], as shown in Figure 2.

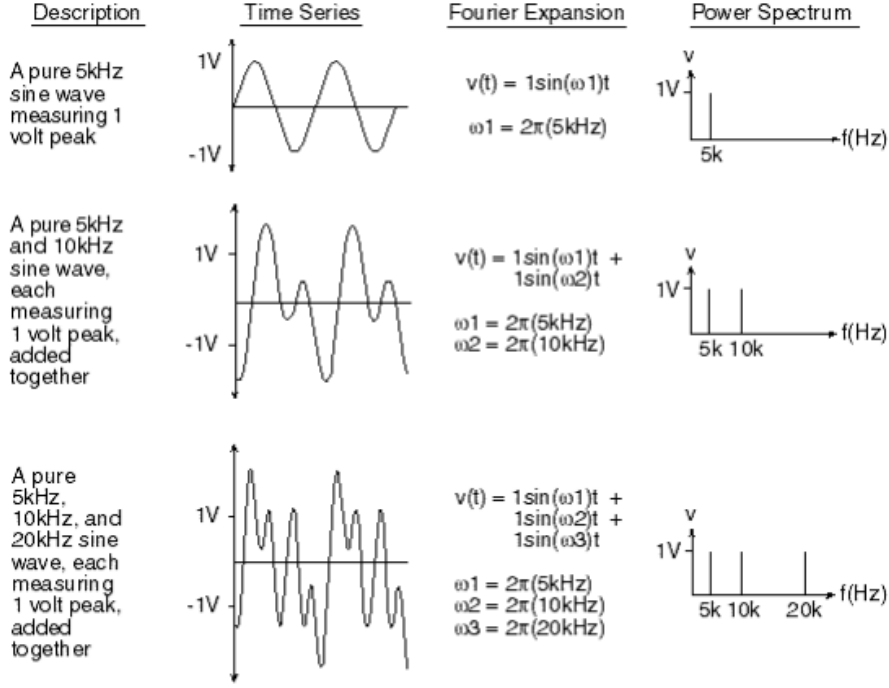


Figure 2: Conversion of time domain signals to frequency domain (image extracted from [2]).

The Fourier series can be expressed by the sum of elementary periodic functions such as sines and cosines, or complex exponentials. Thus, being  $f$  a real or complex function of a real variable  $x$ , and  $X$  being the period, it is written the Fourier series according to Equation 4 [27]:

$$f(x) = \sum_{n=0}^{\infty} a_n \cos(2\pi nx/X) + \sum_{n=1}^{\infty} b_n \sin(2\pi nx/X) = \sum_{-\infty}^{\infty} c_n \exp(2\pi jnx/X) \quad (4)$$

By integration over one cycle of the function, the coefficients of the Fourier series can be obtained in Equation 5:

$$c_n = \frac{1}{X} \int_{x_0-X/2}^{x_0+X/2} f(x) \exp(-2\pi jnx/X) dx \quad (5)$$



When  $X$  is increased towards infinity,  $n/X \rightarrow y$ ,  $1/X \rightarrow dy$  and  $c_n \rightarrow g(y)dy$ . With this, Equations 4 and 5 becomes, respectively, Equations 6 and 7, where  $g(y)$  is the Fourier transform of  $f(x)$ .

$$f(x) = \int_{-\infty}^{\infty} g(y) \exp(2\pi jxy) dy \quad (6)$$

$$g(y) = \int_{-\infty}^{\infty} f(x) \exp(-2\pi jxy) dx \quad (7)$$

### 2.5.2 Transmission parameters

To create a link budget depicting the gains and losses of a radio channel, the Friis transmission equation is used to calculate the power received at the terminals of a **RX** based on the power transmitted from the **TX**, the distance between antennas and its characteristics [28, 29], as stated in Equation 8. Figure 3 presents a basic radio transmission diagram with the main elements.

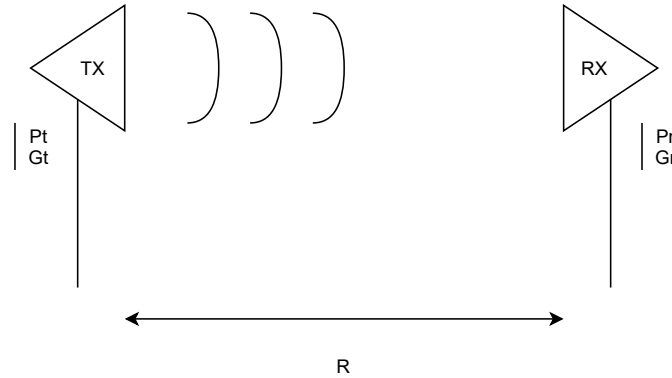


Figure 3: Diagram depicting a radio transmission.

$$\frac{P_r}{P_t} = e_r e_t \left( \frac{\lambda}{4\pi R} \right)^2 D_r D_t = \left( \frac{\lambda}{4\pi R} \right)^2 G_r G_t \quad (8)$$

Where:

$P_r$  is the received power in Watts;

$P_t$  is the transmitted power in Watts;

$e_r$  is the **RX** antenna efficiency;

$e_t$  is the **TX** antenna efficiency;

$\lambda$  is the electromagnetic wavelength;

$R$  is the far-field **Line-of-Sight (LoS)** distance between antennas;

$D_r$  is the **RX** antenna directivity relative to an isotropic antenna;

$D_t$  is the TX antenna directivity relative to an isotropic antenna;

$G_r$  is the RX antenna gain;

$G_t$  is the TX antenna gain.

In a radio channel, the distance between antennas imply signal losses. By knowing the value of such losses, it is possible to characterise the TX and RX antennas parameters to achieve optimal connectivity conditions. This is described as **Free Space Path Loss (FSPL)** [30], and it can be derived from Equation 8, as shown in Equation 9:

$$FSPL = \left(\frac{4\pi R}{\lambda}\right)^2 \quad (9)$$

To calculate FSPL in dB, it is used Equation 10, where  $f$  is frequency,  $f = c/\lambda$  and  $c$  is the speed of light ( $c = 3 \times 10^8$  m/s).

$$FSPL(dB) = 20\log_{10}(R) + 20\log_{10}(f) - 147.55 \quad (10)$$

### 2.5.3 Near and Far-field

The EM radiation generated by a transmitting antenna can be divided in two regions [3]: near-field and far-field, which can be seen in Figure 4. The near-field region can also be divided in two more regions: reactive near-field and radiating near-field. Ideally, the distance between TX and RX antennas must be established in the far-field region since EM electric and magnetic waves are in-phase, whereas in the near-field region, the relation between the electric and magnetic waves are complex. The minimum distance can be calculated according to Equation 11 [31].

$$r = \frac{2D^2}{\lambda} \quad (11)$$

Where:

$r$  is the distance from the antenna to the start of the far-field region;

$D$  is the antenna largest dimension;

$\lambda$  is the electromagnetic wavelength.

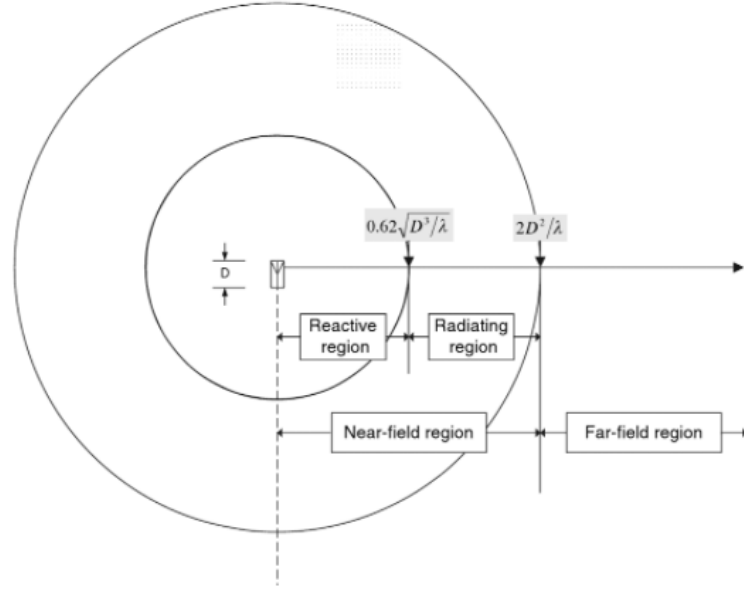


Figure 4: Far-field and near-field regions generated by an antenna (image extracted from [3]).

## 2.6 S-PARAMETERS

Scattering parameters, or S-parameters in short, define the reflected waves to incident waves in a linear network [32]. Figure 5 presents a two port network, which can be described by equivalent circuit parameters such as transfer matrix, impedance matrix, admittance matrix and scattering matrix[4].

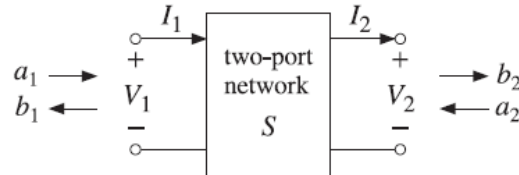


Figure 5: Two port network (image extracted from [4]).

The transfer matrix relates the voltage and current from port 1 with those at port 2, and the impedance matrix relates the voltages  $V_1$  and  $V_2$  to the currents  $I_1$  and  $I_2$ . Equations 12 and 13 present the transfer matrix and impedance matrix respectively.

$$\begin{bmatrix} V_1 \\ I_1 \end{bmatrix} = \begin{bmatrix} A & B \\ C & D \end{bmatrix} \begin{bmatrix} V_2 \\ I_2 \end{bmatrix} \quad (12)$$

$$\begin{bmatrix} V_1 \\ V_2 \end{bmatrix} = \begin{bmatrix} Z_{11} & Z_{12} \\ Z_{21} & Z_{22} \end{bmatrix} \begin{bmatrix} I_1 \\ -I_2 \end{bmatrix} \quad (13)$$

It can thus be concluded in Equations 14 and 15 that to two port systems, the transfer matrix and the impedance matrix are 2x2 matrices.

$$T = \begin{bmatrix} A & B \\ C & D \end{bmatrix} \quad (14)$$

$$Z = \begin{bmatrix} Z_{11} & Z_{12} \\ Z_{21} & Z_{22} \end{bmatrix} \quad (15)$$

The admittance matrix is the inverse of the impedance matrix ( $Y = Z^{-1}$ ), and the scattering matrix consists in the relation of the outgoing waves  $b_1$  and  $b_2$  with the incoming waves  $a_1$  and  $a_2$ , incident on the two port, as seen in Equation 16. Equation 17 presents the scattering matrix.

$$\begin{bmatrix} b_1 \\ b_2 \end{bmatrix} = \begin{bmatrix} S_{11} & S_{12} \\ S_{21} & S_{22} \end{bmatrix} \begin{bmatrix} a_1 \\ a_2 \end{bmatrix} \quad (16)$$

$$S = \begin{bmatrix} S_{11} & S_{12} \\ S_{21} & S_{22} \end{bmatrix} \quad (17)$$

## 2.7 ELECTROMAGNETIC SHIELDING EFFECTIVENESS

To analyse whether a material is transparent or opaque to EM radiation, it is used the SE, which is a normalised result of signal power attenuation caused by a Device Under Test (DUT) in the radio propagation path [16, 33, 34], which is acquired from conducted S-parameters measurements, preferably in a controlled environment, such as an anechoic chamber, to decrease unwanted signals level. Two  $S_{21}$  measurements must be performed, one with a structure and the other without it, and the remaining components position within the scenario such as TX and RX must not be altered. SE is calculated according to Equation 18, where  $S_{21}(DUT)$  is the measurement with a DUT and  $S_{21_0}$  without it (free space).

$$SE(dB) = S_{21_0} - S_{21}(DUT) \quad (18)$$

## 2.8 INTERIM CONCLUSIONS

This chapter presents methods and concepts regarding wood related parameters and radio propagation characteristics. More specifically, it is reviewed the direct and indirect processes in the acquisition of moisture content of wood and its electrical properties, namely permittivity. The EM signals are characterised, with the importance of Fourier transformation being demonstrated here. It is described the radio propagation system, with the key components being the TX, RX and the medium between these two, and its relation. The distance between RX to the radiating regions of the TX is explained, being the ideal RX placement in the far-field region. A deduction of S-parameters is shown as well as its relation in a linear network, and finally it is described how SE can be extracted from  $S_{21}$  measurements of the structure and free space.

This page is intentionally left blank.

## SCRIPT DEVELOPMENT FOR BARRIER MODELLING

---

### 3.1 INTRODUCTION

This chapter presents a solution to improve the structure modelling process and greatly decrease the model building time. This consists in a script developed in MATLAB, which sends the structure's construction commands to the simulation environment [CST MWS](#), a software dedicated to 3D modelling and [EM](#) simulations. By pairing the mathematical capabilities of MATLAB with the [EM](#) solver, it is possible to generate the desired geometry and [EM](#) related parameters such as boundary conditions and ports. Such tool proves to be very time efficient since one can design a barrier with the preferred variables within seconds, whereas if the model was to be manually built, it could take an hour or more.

The overall functionality of the developed script will be presented and the various sections that constitute it will be detailed thoroughly in this chapter.

### 3.2 ENVIRONMENT SETTINGS AND INITIALISATION

Prior to the script execution, there are steps regarding initialisation in [CST](#) which must be realised. This consists in setting up a project template with the necessary parameters, which goes as follows:

- Select a workflow;
- Pick the preferred solver;
- Choose the magnitude of the units to be used, according to [International System of Units \(SI\)](#);
- Define minimum and maximum frequency.

Typically, the selected workflow is "Microwaves & RF/ Optical" as it's related to the expected setup. The picked solver is "Time Domain" since it provides the necessary simulation accuracy at high frequencies, whereas "Frequency Domain" is faster only if the number of frequency samples are small. The main units are set to default (dimensions in mm and frequency in GHz) and minimum/maximum

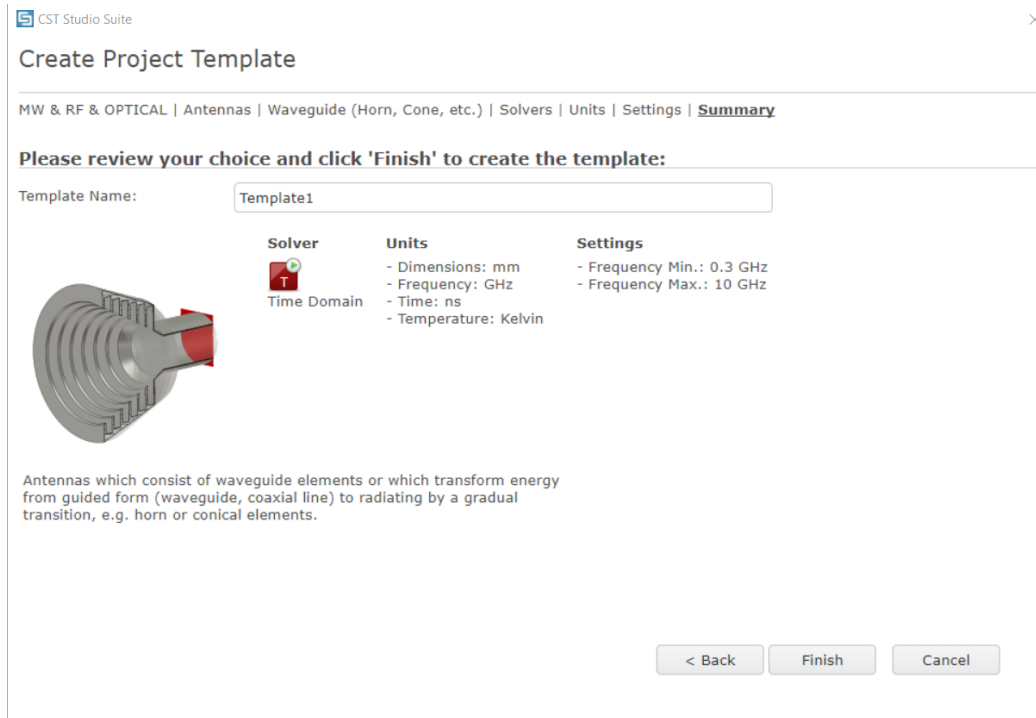


Figure 6: Defined environment setup in CST.

frequency is chosen according to the desired simulation scenario. Figure 6 presents the defined parameters in CST.

### 3.3 MODELLING PROCESS FLOW

The modelling script and its associated functions are developed in MATLAB, which can be found in Appendix A. After setting up the simulation environment according to the previous subchapter, the parameters that describe the model such as trunks' spacing and MC must be defined in the script and then the program can be run to build the model in CST. This consists in a series of "invoke" commands containing Visual Basic for Applications (VBA) instructions, which can be seen in "history list" within CST, a monitor where the performed actions are recorded.

Figure 7 presents a flowchart depicting the general actions of the script, and the sequence can be summarised as follows: the process is started by accessing CST with the use of commands presented in the code block 3.1, to allow communication from MATLAB to the simulation software. Afterwards, variables used for parametrisations and MC data used to create materials (wood), are loaded into CST and thus, from this point, the 3D modelling begins. A stacked quantity of tube shaped objects, each with a specific MC value and radii, are created to define the main trunk, and surface roughness around the trunk is then implemented according to the user's choice. The main trunk is multiplied in one direction, forming a layer, which can



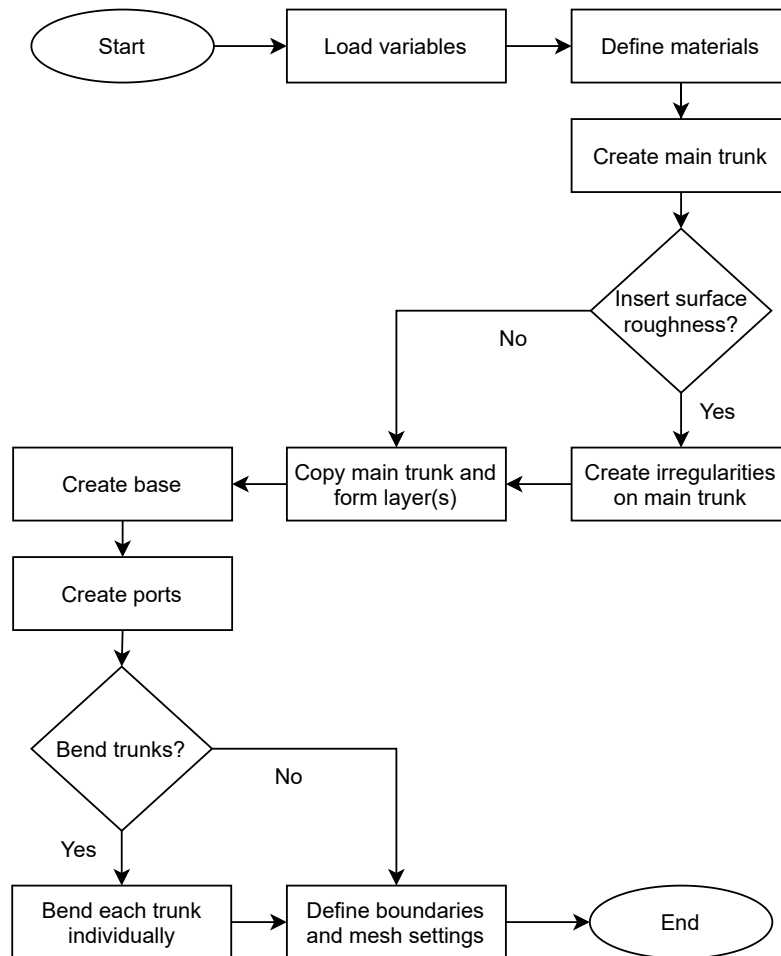


Figure 7: Flowchart depicting the developed script process for model creation.

then be multiplied to form a multilayered structure, and finally, the base is added to the bottom of the constructed geometry. Two ports that puts the built structure in between are placed to allow S-parameters simulation and every single trunk can then be bent in different directions if the user desires to. The script process is concluded with the definition of **EM** boundaries to allow specific simulation scenarios and the mesh settings are tuned.

The following subchapters details extensively the steps presented in Figure 7 to further understand the geometry calculation and general implementations.

```

1 %% Access CST
2 cst = actxserver('CSTStudio.application');
3 mws = cst.invoke('Active3D');

```

Listing 3.1: Instructions to access **CST**

### 3.3.1 Material definition

Before forming the main trunk, the characteristics of the materials, in this case, wood, must be defined. This consists in associating **MC** values to the material and weight density of wood, with the latter being specified as  $\rho = 500\text{kg}/\text{m}^3$ , according to [35].

Appendix A.2 presents the function used to define materials in the simulation environment, where in order to implement humidity in trunks, **MC** data is taken from [5], which consists in tables with **MC** values of wood at the temperature of  $20^\circ\text{C}$ , being the available values 10, 20, 30 and 60%, at the frequencies of 1, 2.4 and 5.8 GHz. These tables, also relate the real part of permittivity and loss tangent values with **MC**, which are then interpolated in the script to allow more data points to be picked between the available **MC** values. Figures 8 and 9 present the graphs that relate the real part of permittivity and loss tangent respectively, with **MC** and frequency.

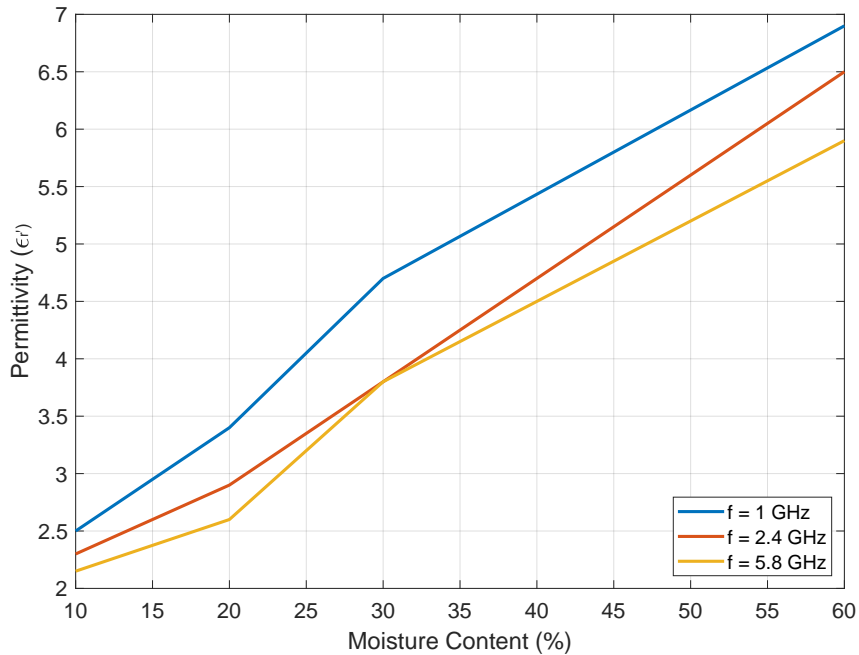


Figure 8: Relation between real part of permittivity, **MC** and frequency with data taken from [5].

In the main script, presented in Appendix A.1, the user can select the minimum and maximum **MC** values to be implemented in the main trunk, and the number of radial layers which the trunk will be composed of, where each radial layer is defined by a material with specific **MC** value. Afterwards it is generated a linearly spaced vector in the defined **MC** range that attributes a **MC** value to each radial layer. This can be seen in Figure 10, which shows a top view of a trunk in **CST**, illustrating some **MC** values defined to radial layers. Figure 11 presents a graph

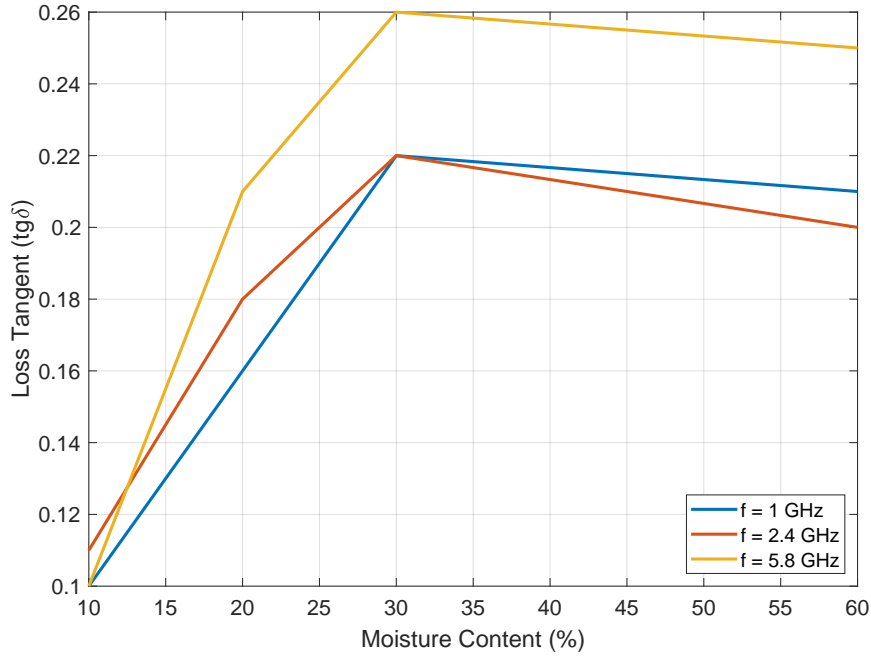


Figure 9: Relation between loss tangent,  $MC$  and frequency with data taken from [5].

upon material definition in *CST* with different curves relating to the permittivity of a material with  $MC = 10\%$  and here, it can be seen that since the frequency range is much higher than that of the available data, the software performs curve fitting automatically.

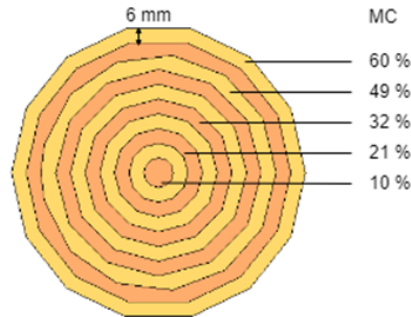


Figure 10: Top view of a trunk depicting the attributed  $MC$  values.

### 3.3.2 Structural conception

Here, all the structural geometry is generated according to the parameters previously specified by the user in the main script, which are the trunks' height, radius, number of radial layers (see previous subchapter for reference), number of trunks in a layer, number of layers, spacing between centre of trunks and spacing between layers. The trunk modelling function can be seen in Appendix A.3 and the process is started by creating the main trunk, composed by a number of cylindrical objects equal to the defined amount of radial layers, each with different internal and external radius,

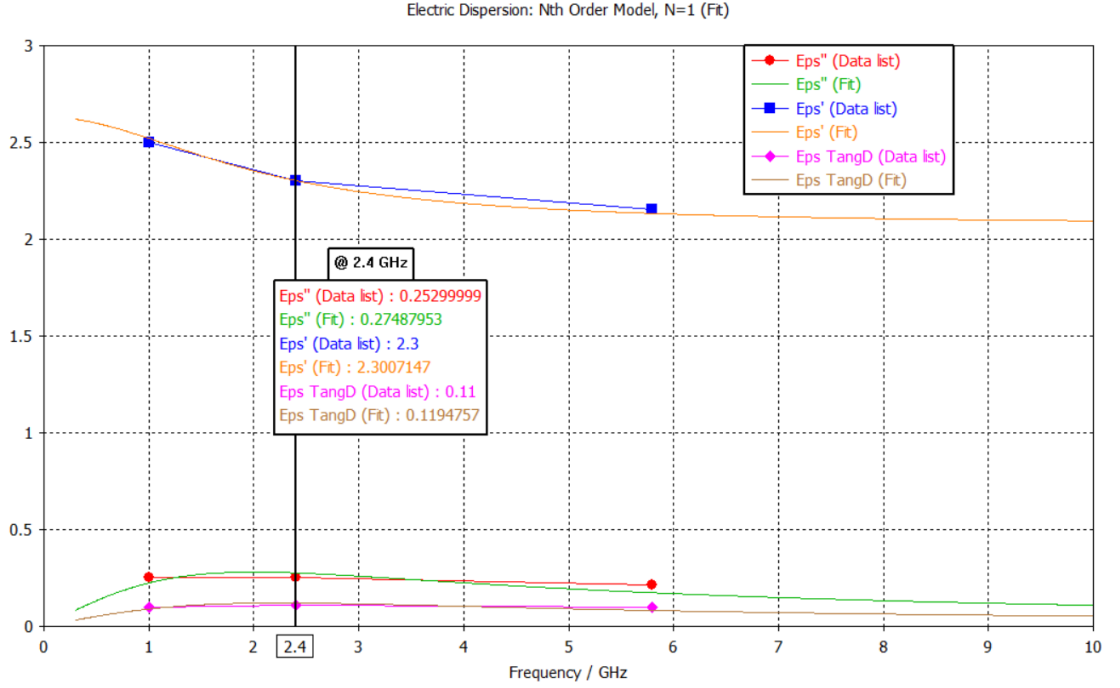


Figure 11: Permittivity related curves of a material with  $MC = 10\%$  and curve fitting in CST.

and material associated to a  $MC$  percentage. Next, irregularities on the trunk's surface can be added, being this implementation detailed in the next subchapter. Then one layer is formed by copying the main trunk in one direction on  $x$ -axis and spaced accordingly, and subsequently the layer can be replicated along the  $y$ -axis to form a multilayered structure.

Following the structure's construction, it is realised a solution in the case of the structure being a periodic sample to be simulated with periodic boundaries, and layers being shifted along  $x$ -axis. This would cause the shifted layer to exceed the model sample volume and therefore creating distortion, as the spacing between trunks would be compromised. As such, an extra trunk is added to the sides of the second and third layer, outside the structural sample, and if a layer is shifted in a way that an original trunk within a layer is partially out of the sample, part of the extra trunk enters the structure volume and the exceeding portions on either side of the model are erased. Figure 12 presents the explained solution, where it can be seen trunks partially erased in order to maintain the periodicity of trunk's spacing on second and third layer.

The final step of the model conception consists in adding a thin base below the structure, which is used as an auxiliary object to define the computational volume and to keep the spacing between centre of trunks constant on the  $x$ -axis, meaning that if the structure sample is to be replicated, the trunks' spacing wouldn't be affected with the added structural clone to the model. Similarly to the solution

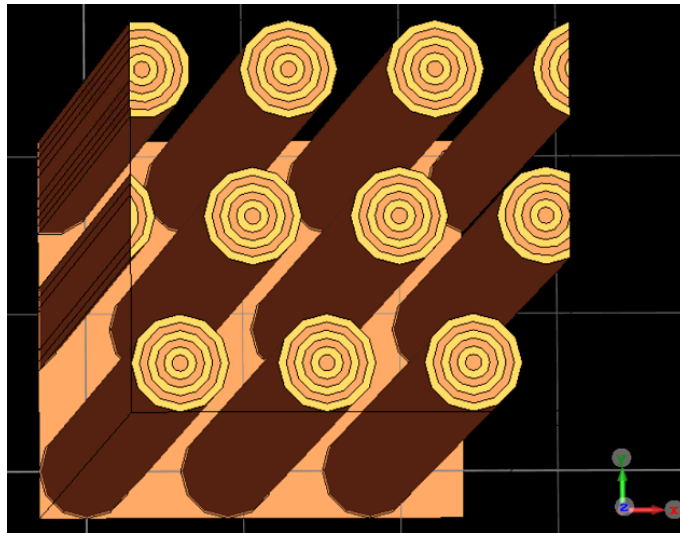


Figure 12: Generated structure containing trunks partially erased to retain trunk's spacing periodicity.

explained earlier, this is important in the case of simulations being performed with periodic boundaries, which will be explained later in this chapter.

### 3.3.3 *Surface roughness implementation*

Irregularities can be added during the conception of the structure if desired. These consist in inserting small cylinders on the main trunk's surface and erasing the intersected volume. The function can be seen in Appendix A.3 and the sequence of this implementation begins by dividing the trunk in a defined amount of longitudinal layers, as illustrated in Figure 13. Next it is placed the cylinders with the layer's height and different radius centred on the different surface positions of the trunk in each layer. Afterwards it is eliminated each cylinder and the volume it occupied before.

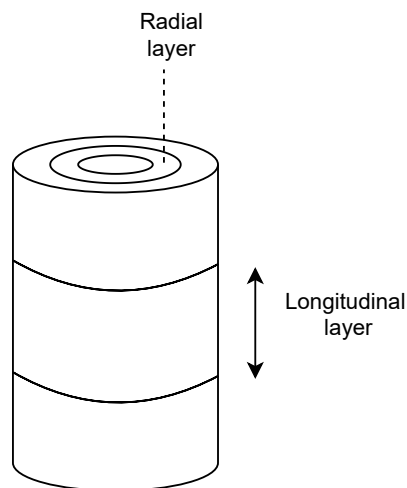


Figure 13: Trunk with marked separations.

Uniform distributions are used with mean ( $\mu$ ) and standard deviation ( $\sigma$ ) values specified for the number of cylinders in each longitudinal layer, the cylinders' height increase and radius in millimetres, and location on the layer's surface in radians. This is done by using the function "rand" in MATLAB, which can be seen in the code block 3.2, where it is shown an example with all irregularities' radius computed using uniform distribution. Here, an array with  $n\_irrlayers(\sigma + \mu + 1)$  indexes of random values between 0 and 1 is created, being  $n\_irrlayers$  the number of longitudinal layers, then these values are normalised to be between 1 and -1, which are then multiplied by  $\sigma$  and summed by  $\mu$ .

```

1 % rnd_r -> array defining the radius of all irregularities
2 % std_dev_r -> standard deviation of radius
3 % av_r -> mean radius
4 % n_irrlayers -> number of longitudinal layers
5 rnd_r = std_dev_r.*(2*rand(1,n_irrlayers*(std_dev_cyl+av_cyl+1))-1) +
    av_r;

```

Listing 3.2: Computation of irregularities radius using uniform distribution

The irregularities location within a longitudinal layer consists in dividing this part of the trunk in slices equal to the number of cylinders to be placed in the layer. Then, the location between every two slices (e.g. a layer with two slices have two locations, at 0 rads and  $\pi$  rads), is shifted according to a value acquired for the cylinder location using uniform distribution and the cylinder is inserted. The division of the longitudinal layer in slices is particularly necessary in the case of the  $\sigma$  of cylinders location being equal to zero, as all irregularities would be placed in the same point. Figure 14 demonstrates the surface roughness being applied on the trunk with the execution of this implementation.

### 3.3.4 *Trunks' bending procedure*

Bending of trunks is a natural occurrence due to its' weight and wind exposure [36], hence the introduction of such deformation in the model. This is performed after the layer formation in the structure and here, each trunk is bent with the parameters associated to uniform distribution, similarly to the previous subchapter. As such, values for  $\mu$  and  $\sigma$  are defined for the height location for the point of bending, the degree and direction of bending, being calculated in a similar way to code block 3.2.

The bending function can be found in Appendix A.4 and the sequence goes as follows: first, it is set up the coordinate system of CST to be centred on the trunk at the height to be bent and rotated according to the bending direction. Then, a cylindrical bend is performed by curving the upper part of the trunk over a virtual cylinder with its radius being  $r = 3500 \times bending\_degree$  mm. Next, the

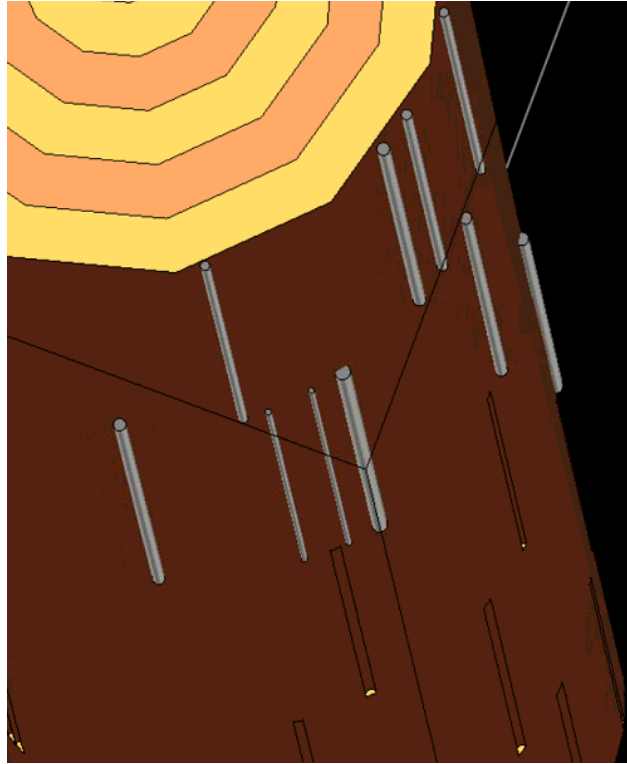


Figure 14: Surface roughness implemented on a trunk.

coordinate system is adjusted to the next trunk accordingly and the explained process is repeated. Figure 15 shows the preview with the bending of the trunk over a virtual cylinder.

### 3.3.5 *Model's electromagnetic characteristics*

The **EM** parameters of the model are introduced during the final steps of the structure conception, which consist in ports, boundary and mesh settings. Such parameters define the simulation accuracy and computation time, which may need tuning according to the preferred scenario and available processing power.

Two waveguide ports are used to compute S-parameters and these are placed parallel the model on both sides, as seen in Figure 16. Here are shown green and purple vectors which refer to the direction of the electric fields and propagation direction of **EM** waves respectively, and here it is presented the electric field polarisation angle, a parameter defined by the user, being in this case horizontally polarised (angle of  $90^\circ$ ).

The boundary conditions define the radiating environment of the model and in the script, the user can define on either side of the structure, perpendicular to the ports, the desired boundary conditions. These consist in either open or periodic. The open condition specify that a selected boundary is a perfect **EM** waves absorber,

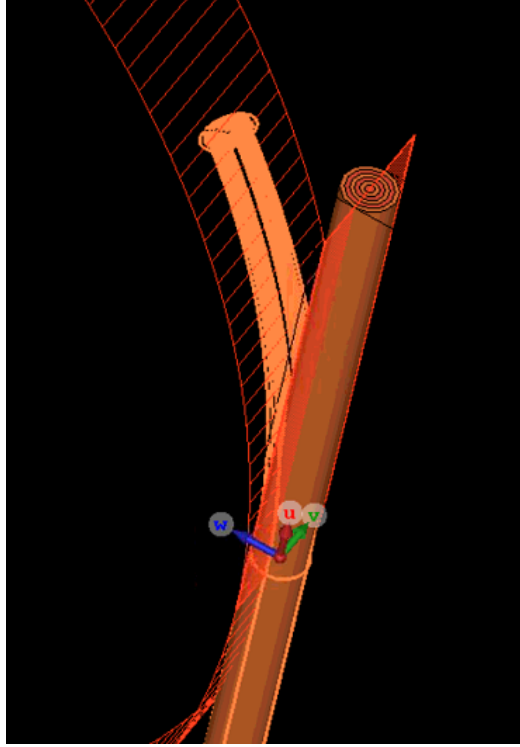


Figure 15: Preview of a trunk bending over a virtual cylinder.

being ideal to simulate a structure consisting in a single sample, while the periodic boundaries (a pair of boundaries parallel to each other) imply that the calculation domain is simulated to be periodically expanded which is ideal to simulate a barrier sample replicated to infinity on  $x$ -axis. However in this case, it is crucial to have a structural sample which can be replicated in a way that doesn't disrupt parameters such as spacing between centre of trunks, being this solved with trunks' partial erasure and a base below the model, as explained in subchapter 3.3.2.

Defining mesh properties of the model is necessary to find the right compromise between simulation time and the quality of results. By modelling a barrier and increasing the simulation frequency range, the total number of mesh cells tend to be high (over one million), which can results in many hours of processing, so the number of cells per wavelength is tuned gradually from 20 to 8.

### 3.4 INTERIM CONCLUSIONS

This chapter presents the script development in MATLAB and working sequence of a barrier modelling in CST. It is shown the creation of the environment in the simulation software, which is followed by loading defined barrier related parameters with the initialisation of the script. It is explained that the generated materials are specified with MC which are associated to permittivity values, that are then used to create the various radial layers which in total compose a single trunk. Surface



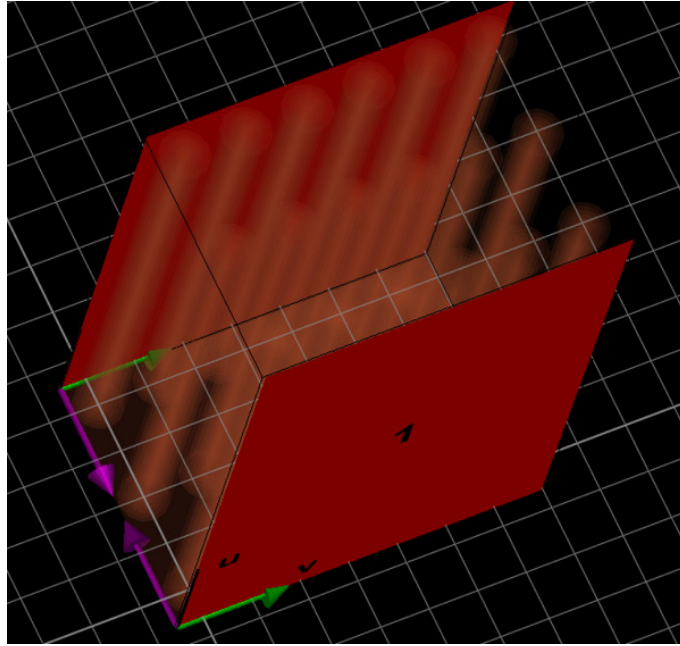


Figure 16: Ports placed located parallel to the barrier showing polarisation vectors.

roughness is shown to be implemented on a trunk's longitudinal divisions, where it is eliminated the intersected volume of the roughness with the trunk, being the irregularities parameters bound to uniform distribution. The structural conception and layer formation is presented with solutions in order to make the structural sample replicable. Trunks' bending is shown to be performed with the curving of the trunk over a virtual cylinder, with the bending parameters being associated to the uniform distribution. The electromagnetic parameters that define the model are presented for the ports used for simulations, it is shown the possibility of having either periodic or open boundary conditions and the reasoning behind balancing simulation accuracy with computation speed is explained.

This page is intentionally left blank.

## MODEL CHARACTERISATION AND ASSESSMENT

## 4.1 INTRODUCTION

This chapter presents the study and design of the wooden structure, where parametrisation of the structure's related variables are performed and simulations in CST are conducted, at the frequencies up to 10 GHz. The barrier is generated with up to three layers, either as a single unit or infinitely and from the simulation results, the model designs are compared, with the analysis of the barrier's optimal configurations for EM shielding and transparency in specific scenarios, mainly at frequencies of commercial interest.

## 4.2 EARLY MODEL DESIGN TRIALS

This subchapter presents two of the first barrier designs with tuned environment parameters, implemented with the developed script, which is explained in the previous chapter. These consist in a triple layered formation of trunks simulated at the frequencies of 0.7 to 5.9 GHz, with ports horizontally polarised and the scenario boundaries set to open condition in all directions. The poles have a height of 1 m, a radius of 60 mm and 5 longitudinal layers for the implementation of irregularities. Through experimentation and observation of trunks used in measurements, the surface roughness and trunks' bending parameters are defined in Tables 1 and 2, with the specified  $\mu$  and  $\sigma$  values related to uniform distribution, as explained in the previous chapter.

Table 1: Roughness parameters defined in the modelling script

Description	$\mu^a$	$\sigma^a$
Number of irregularities in a longitudinal layer	10	0
Irregularities' radius	1 mm	0.5 mm
Irregularities' height increase (top and bottom)	0 mm	6 mm
Irregularities' location on longitudinal layer	0 rad	$\pi$ rad

<sup>a</sup>  $\mu$  is the mean and  $\sigma$  the standard deviation.

Table 2: Bending parameters defined in the modelling script

Description	$\mu^a$	$\sigma^a$
Bending location (based on trunks' height)	height/3 mm	height/6 mm
Bending degree (cylindrical bend)	5	2
Bending direction	0 rad	$\pi$ rad

<sup>a</sup>  $\mu$  is the mean and  $\sigma$  the standard deviation.

#### 4.2.1 Structure sample analysis

Here, an experimental sample composed of 3x3 trunks is presented, where four case scenarios are studied, as seen in Figure 17. Case A depicts a simple structure composed by cylinders with  $\epsilon'$  of 3.2, according to [16]. Case B introduces radial layers to the poles with MC linearly spaced from 10% to 60%, central layer to outer layer respectively. Case C adds to case B surface roughness and case D is composed by the case C with added bending of the trunks. In all case scenarios, the spacing between centre of trunks is 160 mm in  $x$  and  $y$  axis directions.

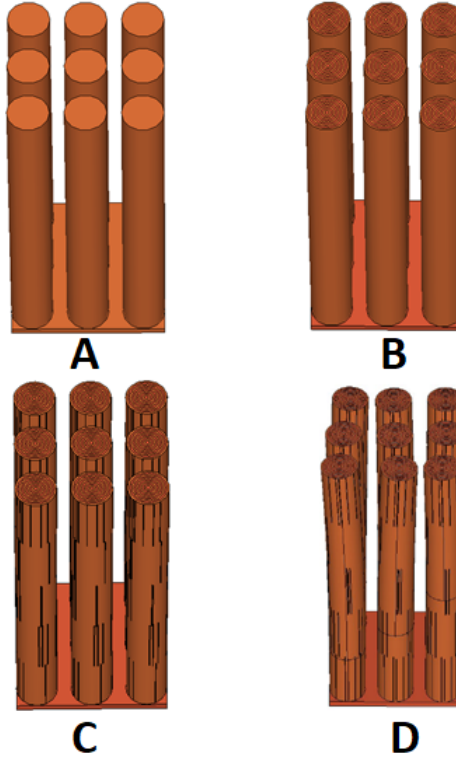


Figure 17: Four case scenarios of a 3x3 structural sample.

Figure 18 presents the simulation results, where it can be seen that the addition of MC to the model brings a noticeable influence throughout all of the observed frequency range, since the overall permittivity is greater, with an average attenuation of 17.81 dB in case B, when compared to case A. The combination of surface

roughness with MC in case C adds slightly more attenuation between 1.9 to 4.3 GHz and the minimum peak is shifted to the right in relation to case B. With added bending, the results are slightly different from that of case B and C, although it can be seen an increased attenuation at 3 GHz of 8 dB. In conclusion, it can be seen that besides having MC within the poles', surface imperfections enhances the SE of the barrier.

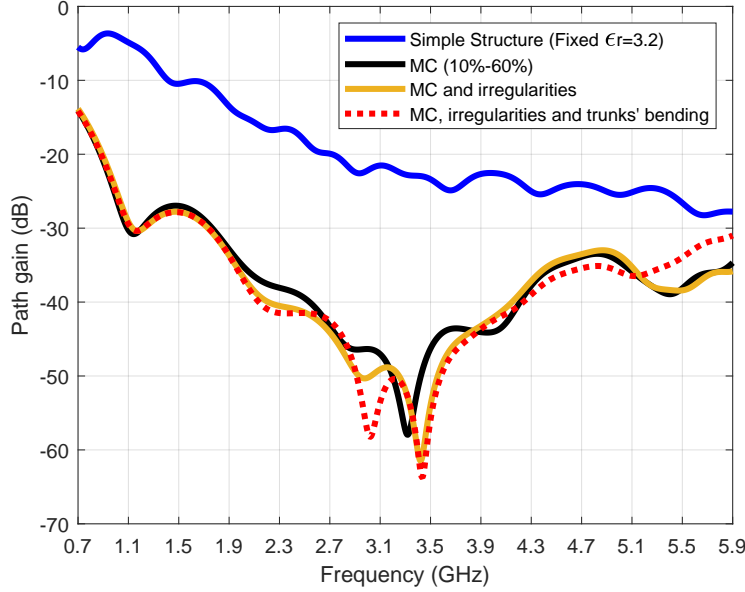


Figure 18: Simulation results of the four case scenarios.

#### 4.2.2 Large structure analysis

Figure 19 presents a 3x9 structure with hybrid properties (EM and acoustic), where it is parametrised the spacing between centre of trunks, which comprises the spacing used for acoustic assessments, according to [10]. The trunks have  $\epsilon'$  of 3.2, added bending and surface roughness. The spacing is parametrised from 160 to 180 mm on  $x$ -axis and on  $y$ -axis the spacing is kept constant, as seen in Figure 20.

Simulations results are presented in Figure 21, where it is seen that the frequency response appears to be shifted to the left as the poles' spacing is increased from 160 to 180 mm. This suggests that adjusting the spacing between the poles may be used to fine tune the desired shielding frequency range or to increase EM shielding performance in a given frequency. Moreover, at commercial frequencies, with the increase of spacing it can be seen a gain of 11 dB at 1.8 GHz (4G) and attenuation of 7 and 3.5 dB at 2.4 and 3.7 GHz (Wi-Fi and 5G) respectively, while at 5.9 GHz (IEEE 802.11p) it is seen a gain of 5 dB.

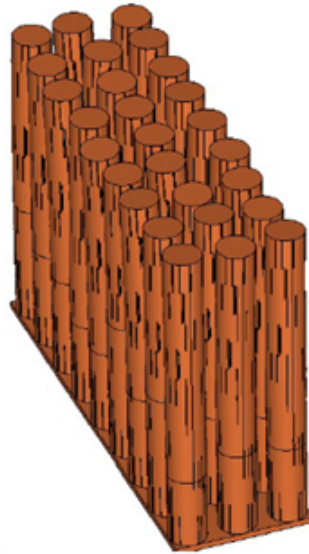


Figure 19: A 3x9 barrier where spacing is parametrised.

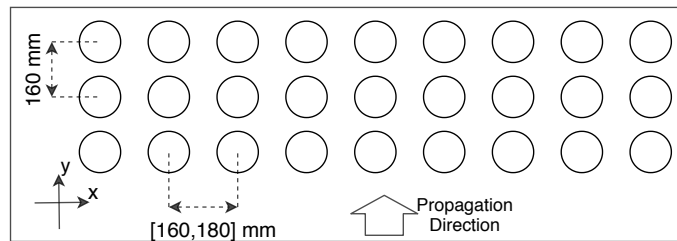


Figure 20: Schematic depicting the configuration used on the 3x9 structure.

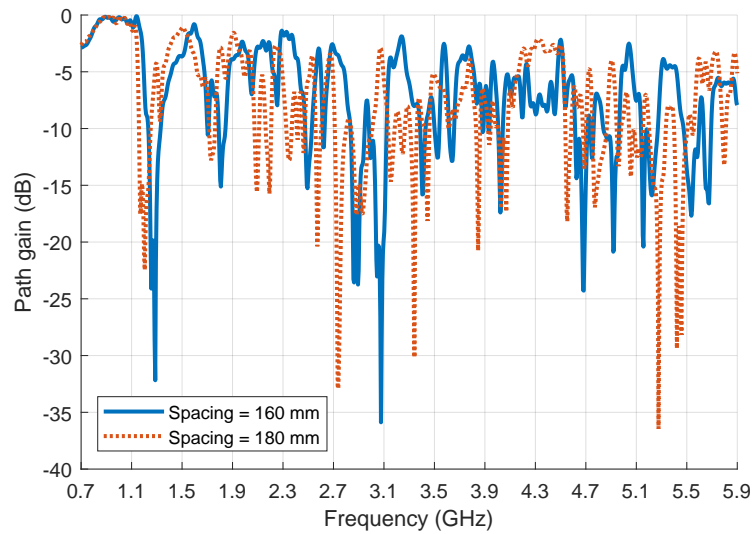


Figure 21: Simulation results of a 3x9 structure with spacing between trunks parametrised from 160 to 180 mm.

## 4.3 PARAMETRISATION STUDY OF AN INFINITE BARRIER

The scenarios and simulations setup in this subchapter are performed with the structural sample being replicated with the use of periodic boundaries, where the model's shielding and transparency capabilities are assessed through a thorough parametrisation of the generated geometry over the frequency range of 0.3 to 10 GHz, from one layer to three layers, with the trunks' MC ranging from 10% to 30%, from the centre to the outer layer. The trunks' height is of 2.27 m, according to Appendix B, where the height evaluation is executed on a batch of thirty log poles used for EM measurements, which will be detailed in the next chapter.

4.3.1 *Trunks' spacing and radius analysis in a single layer*

A single layered structure is generated where the spacing between trunks is parametrised from 120 to 200 mm and the trunk radius parametrised from 20 to 90 mm. The constructed geometry sample is replicated to infinity on x-axis, as seen in Figures 22a and 22b, where it is depicted the absence of irregularities and bending on the trunk.

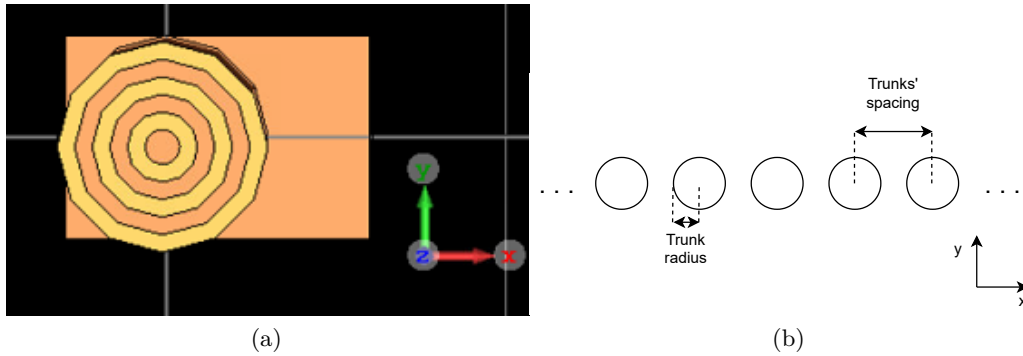


Figure 22: Top view of the structural sample consisting of one layer (a) and the respective diagram (b).

Figure 23 presents the simulation results with the parametrisation of radius from 20 to 90 mm, with spacing between centre of trunks fixated at 180 mm. From the obtained curves, it is seen that a radius of 90 mm causes an increased attenuation since there is no LoS between ports. The overall path gain is progressively reduced to -10 dB with the rise in radius, up to 50 mm, while increasing the radius past this value, a substantial attenuation is viewed mainly at frequencies ranging from 3.5 GHz onward. A valley shift is observed with a radius of 20 mm at 2.4 GHz, down to 1 GHz as radius increases, proving that this structure can be have Frequency Selective Surface (FSS) characteristics, as attenuation can be increased or decreased at specific frequencies. From this parametrisation, it is extracted data at frequencies of commercial interest, as seen in Table 3, where it can be seen that in general,

decreasing radius improves EM transparency, especially with values of 20 and 30 mm. However, trunks with a radius of 50 mm presents a good transparency when compared to neighbouring radii values, especially at 3.7 GHz. For EM shielding purposes, it is clear that having a higher radius is ideal to such effect since higher frequencies EM waves do not penetrate obstacles as much as low frequency waves.

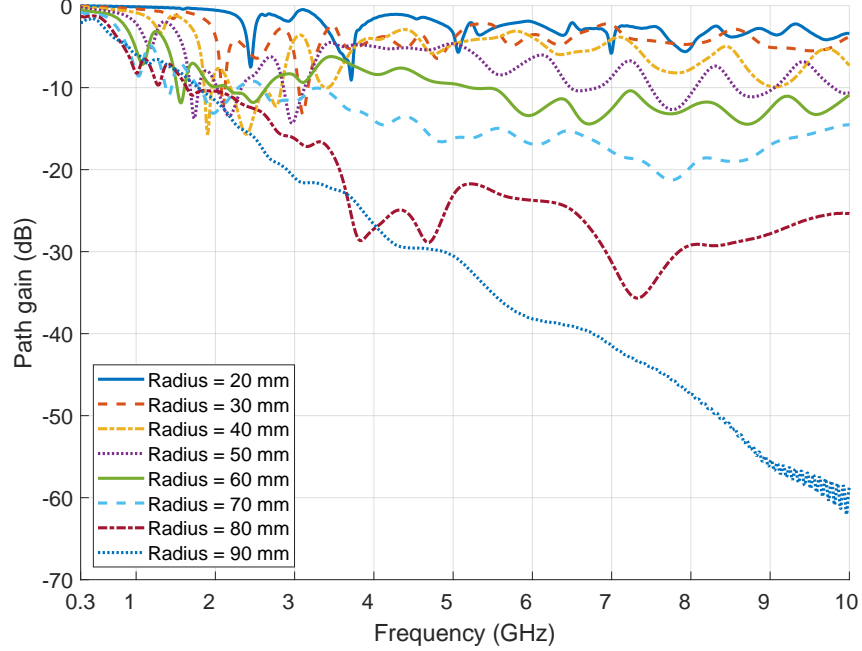


Figure 23: Simulation results with radius parametrised in a single layer composed of trunks with spacing between centre of trunks of 180 mm.

Table 3: Simulation results with data taken from Figure 23, at frequencies of commercial interest, where radius is parametrised in a single layer composed of trunks with spacing between centre of trunks of 180 mm.

Radius (mm)	Path gain (dB)			
	Frequency (GHz)			
	1.8	2.4	3.7	5.9
20	-0.4	-4	-8.7	-1.9
30	-1.3	-5.4	-5.3	-4
40	-5.3	-15.7	-5.7	-3.4
50	-9.5	-9	-4.9	-6.9
60	-7.9	-11.2	-7.2	-13.3
70	-10.1	-9.4	-12.8	-16.5
80	-10.4	-12.3	-25.1	-23.6
90	-10.2	-15.4	-23.3	-37.8

In Figure 24 it is presented the simulation results with the parametrisation of spacing between centre of poles from 120 to 200 mm, with radius fixated at 60 mm. The LoS between ports is blocked with a spacing of 120 mm, showing an almost linear curve where it can be seen that path gain is greatly reduced at the



frequencies starting from 3 GHz onward. The curve with 140 mm of spacing also presents this phenomenon, although its effect is not as severe. The results with spacing from 160 to 200 mm show similarities in SE and shape throughout the EM spectrum, despite the curve relating to 160 mm presenting an increased attenuation. By comparing these results with the ones in Figure 23, it can be seen the curves relating to radius of 50 to 70 mm are similar to the curves with spacing of 160 to 200 mm and the valley shifts at lower frequencies are more noticeable with the parametrisation of radius. Data from simulation results in Figure 24 are extracted at commercial frequencies, as seen in Table 4. Here, it can be seen clearly that even though having no LoS as spacing set to 120 mm, it is observed high transparency capabilities of the structure at 1.8 and 2.4 GHz, when compared to the remaining spacing values. Increasing spacing between centre of trunks causes a decrease in SE of the structure at 3.7 and 5.9 GHz. However, at 1.8 and 2.4 GHz, the highest difference in path gain is of 4.6 dB, proving a nearly constant behaviour imposed by the barrier at these frequencies.

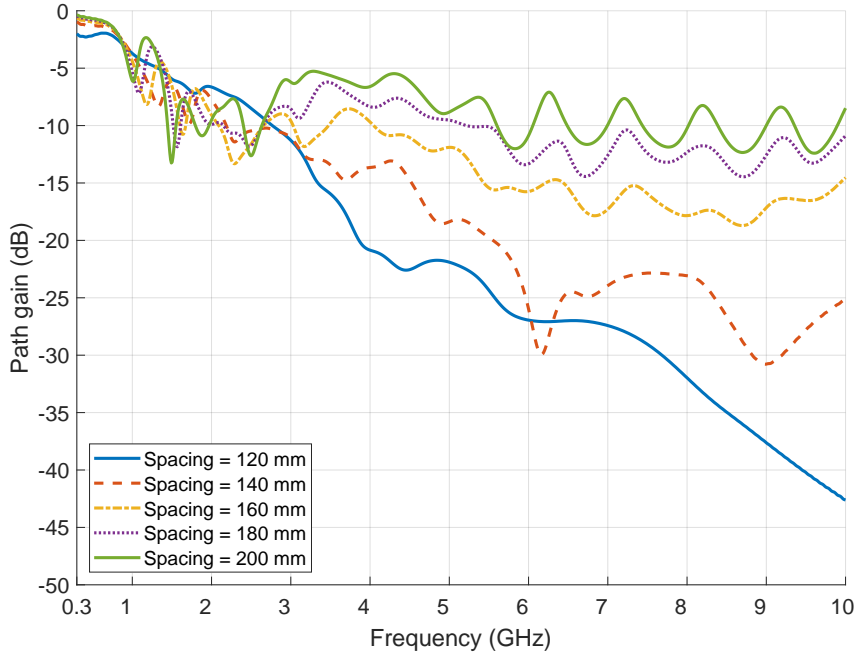


Figure 24: Simulation results with spacing between centre of trunks parametrised in a single layer composed of trunks with radius of 60 mm.

#### 4.3.1.1 Parametrisation of trunks' spacing and radius for increased transparency

Here, the spacing between centre of trunks is parametrised to values beyond that of optimal for acoustic performance. Such parametrisation is performed from 220 to 300 mm, with radius being also parametrised, from 50 to 70 mm, which results in a total of 15 curves.

Table 4: Simulation results with data taken from Figure 24, at frequencies of commercial interest, where spacing between centre of trunks is parametrised in a single layer composed of trunks with radius of 60 mm.

Spacing (mm)	Path gain (dB)			
	Frequency (GHz)			
	1.8	2.4	3.7	5.9
120	-7.2	-7.9	-17.8	-26.8
140	-7.9	-10.8	-14.7	-23.5
160	-6.8	-12.5	-8.6	-15.7
180	-7.9	-11.2	-7.2	-13.3
200	-10.1	-9.8	-6.1	-11.9

Figure 25 presents the results with pole’s radius fixated at 60 mm and spacing parametrised from 220 to 300 mm. Here it can be seen that by increasing the spacing, path gain is also increased by nearly 5 dB, starting from 4.5 GHz. These results also shows how the barrier can function as a band-rejection filter between the frequencies of 1.1 to 2.2 GHz, with SE increased up to -30.88 dB at 1.697 GHz for a spacing of 260 mm. However, the spectrum shape is similar at high frequencies.

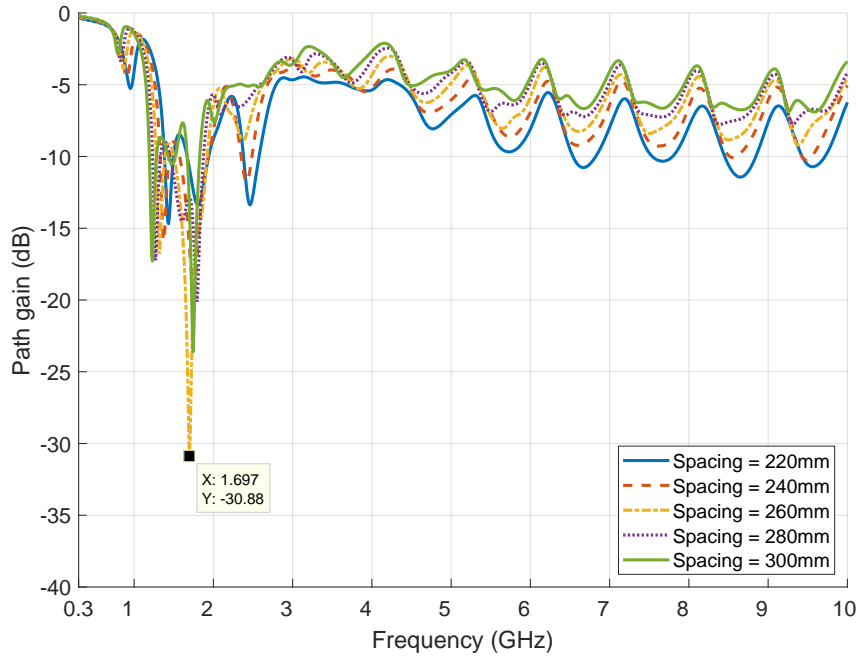


Figure 25: Simulation results with parametrisation of spacing between centre of trunks in a single layer composed of trunks with radius of 60 mm.

Figure 26 presents the results with spacing between centre of poles set to 220 mm and radius parametrised from 50 to 70 mm. It is clear how reducing the radius increases transparency at frequencies starting from 3 GHz onward. However, the structure’s SE is increased at frequencies ranging from 1.2 to 3 GHz. Figure 27 presents the same settings as the previous figure, with the exception of spacing, as

it is set to 300 mm. Overall, this spacing results in a more transparent barrier to radio propagation at frequencies starting from 2 GHz, but higher radius reduces the gain, with abrupt valleys at 1.47 and 1.75 GHz with values of -38 and -23.6 dB for a radius of 70 and 60 mm respectively.

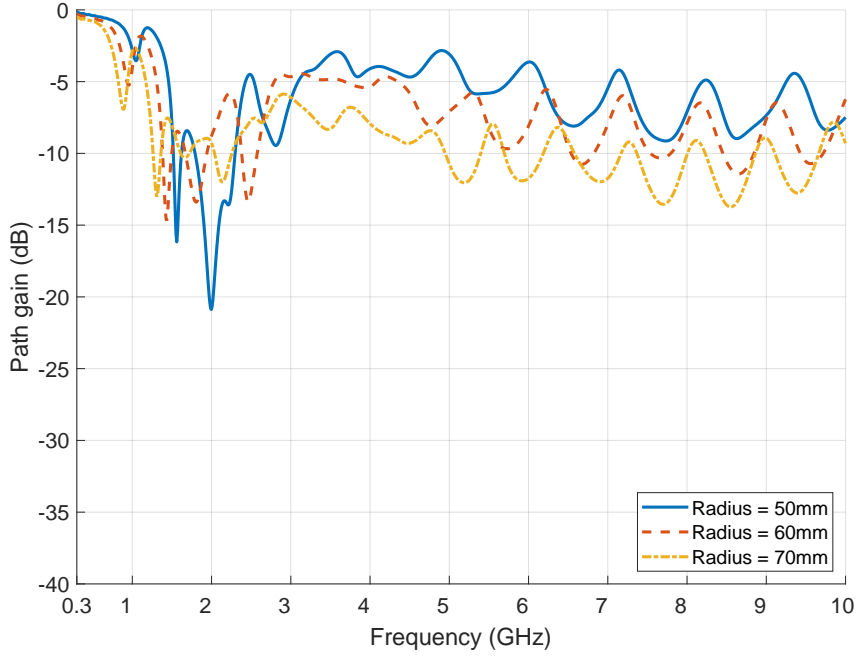


Figure 26: Simulation results with parametrisation of radius in a single layer with spacing between centre of trunks set to 220 mm.

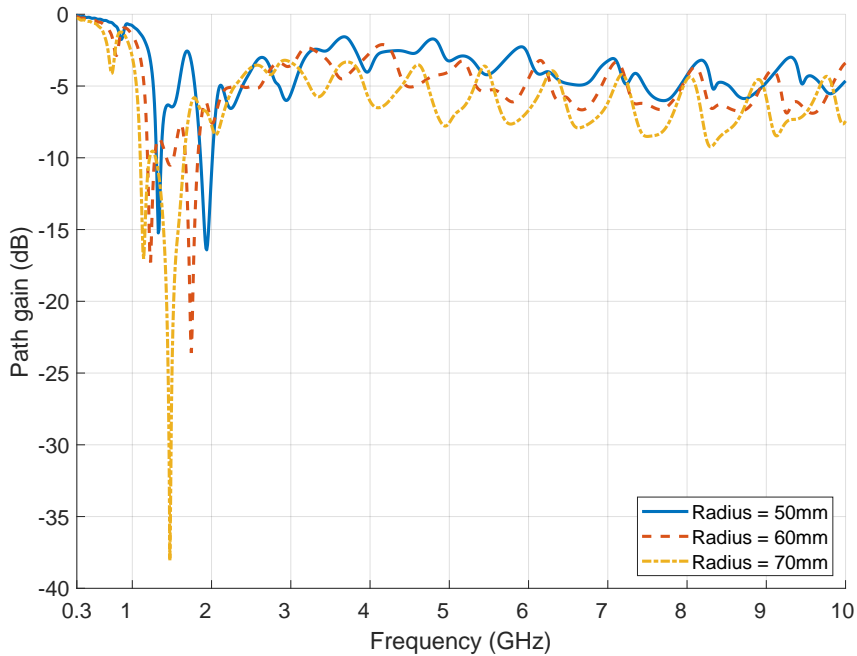


Figure 27: Simulation results with parametrisation of radius in a single layer with spacing between centre of trunks set to 300 mm.

Table 5 presents the simulation results summarised at frequencies of commercial interest, where it is seen a transparency increase with the reduction of radius at

frequencies of 3.7 and 5.9 GHz, while at 1.8 GHz, the results show higher SE with trunk’s radius of 60 mm. By comparing different pole radius cases at 2.4 GHz, as spacing increases, gain values become similar. Overall, with the increase of spacing and reduction of radius, the structure’s transparency capabilities are enhanced, especially at higher frequencies. From this table, the ideal parameters for reduced SE are radius set to 50 mm and spacing set to 280 mm, which yields an average gain of -3.55 dB.

Table 5: Simulation results from the parametrisation of trunks’ spacing and radius for increased EM transparency, at frequencies of commercial interest.

		Path gain (dB)			
		Frequency (GHz)			
Radius (mm)	Spacing (mm)	1.8	2.4	3.7	5.9
50	220	-10.34	-5.73	-3.48	-4.06
	240	-11.62	-4.86	-3.89	-3.56
	260	-7.46	-7.08	-2.41	-3.17
	280	-3.79	-5.88	-2.01	-2.53
	300	-5.79	-4.93	-1.62	-2.27
60	220	-13.4	-10.9	-5.07	-9.07
	240	-16.24	-11.5	-4.43	-7.93
	260	-15.43	-8.77	-4.68	-6.9
	280	-19.21	-6.31	-4.82	-5.98
	300	-12.42	-5.05	-4.32	-5.58
70	220	-9.25	-8.47	-6.88	-11.9
	240	-8.14	-6.81	-5.19	-10.44
	260	-6.98	-5.06	-5.04	-9.57
	280	-5.88	-4.56	-4.18	-8.38
	300	-5.91	-4.3	-3.32	-7.28

#### 4.3.2 Double layer parametric study

A double layered structure is proposed, where all trunks’ possess the same radius, and the spacing between centre of trunks on  $x$ -axis are equal to each layer but the spacing between layers (from the centre of trunks between each layer on  $y$ -axis), is fixated to 180 mm. The offset is applied on the upper layer, as depicted in Figure 28b, which consists in a shift along  $x$ -axis and here, the absence of an offset implies that the layers are symmetrical, as illustrated in Figure 28a. Surface roughness and bending on the trunks are not applied to the structure.

Figure 29 depicts the parametrisation of trunks’ radius from 50 to 70 mm and layer offset to 0 and 90 mm. Here, a layer offset of 90 mm indicates that the upper

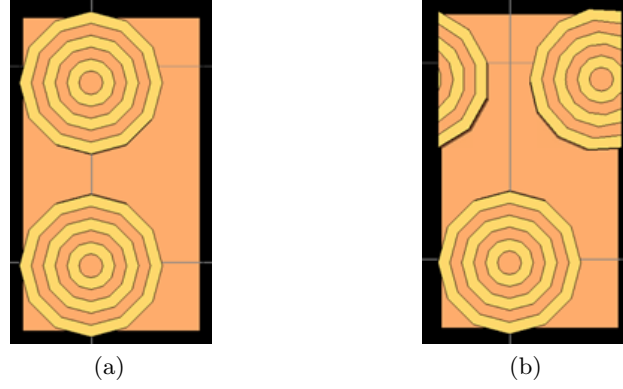


Figure 28: Top view of the structural sample consisting of two layers with no offset (a) and the same setup but with a layer offset (b).

layer is de-phased in relation to the bottom layer by half of the spacing between centre of trunks, which is best demonstrated in Figure 28b. It is seen that with either offset value for a radius of 70 mm, the SE is greater when compared to all other cases on central frequencies, with path gain below -20 dB. Having no offset results in a better overall EM transparency throughout the frequency range, although the opposite is seen with a radius increase. Valleys are most notorious at frequencies below 2 GHz, with increasing attenuation up to 40 dB as layer offset and radius are increased. From the data acquired in this simulation, values at commercial frequencies are extracted to Table 6, where it is clear that by either increasing radius or offset, the structure become more opaque to incident radiation at almost all presented frequencies. The trunks with a radius of 60 mm have a similar performance with either offset value, at 3.7 and 5.9 GHz, and for a radius of 50 mm, the structure is the least effective on shielding.

Table 6: Simulation results with data taken from Figure 29, at frequencies of commercial interest, where trunks' radius and layer offset are parametrised in a double layer configuration with the spacing between centre of trunks' set to 180 mm.

		Path gain (dB)			
		Frequency (GHz)			
Layer offset (mm)	Radius (mm)	1.8	2.4	3.7	5.9
0	50	-6.7	-10.4	-8.2	-11
	60	-10.7	-12.8	-15.3	-18.2
	70	-19.3	-26.5	-35.6	-26
90	50	-12.6	-10.8	-12.6	-14.4
	60	-14.7	-18.2	-15.2	-18.2
	70	-20.2	-18.1	-20.6	-31.6

Figure 30 presents the parametrisation of spacing between centre of trunks from 160 to 180 mm and layer offset, from 80 to 90 mm. Here, with each offset increase, the spacing is increased by 10 mm to retain the geometry aspect similar to the

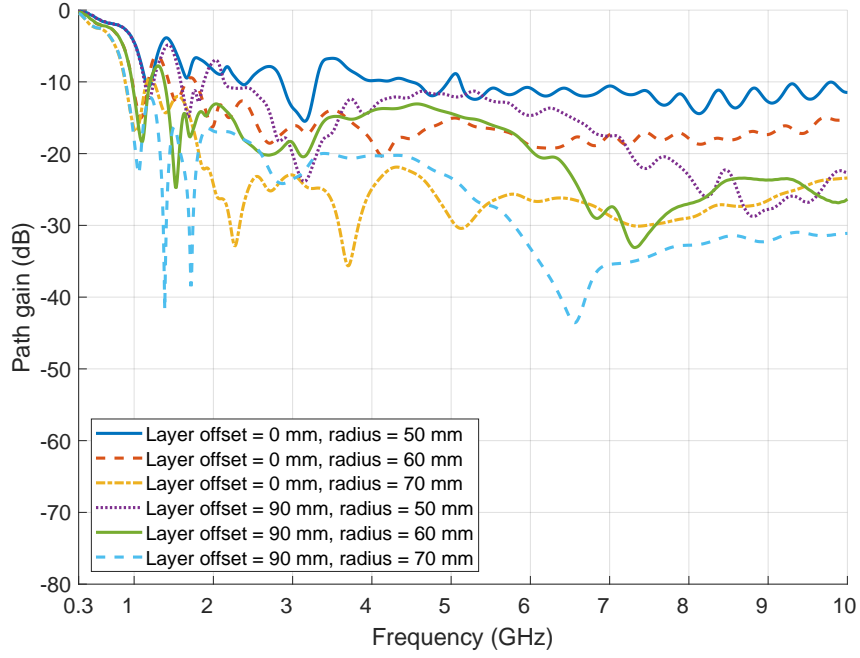


Figure 29: Simulation results with parametrisation of trunks' radius and layer offset in a double layer configuration with the spacing between centre of trunks' set to 180 mm.

one seen in Figure 28b. The curves related to the offset from 80 to 90 mm show similarities in shape and values to each other throughout most of the EM spectrum, with path gain going below -20 dB at higher frequencies, while without the presence of offsets, the transparency is generally better. The structure with a spacing of 160 mm and no offset presents higher SE at central frequencies, while it is seen a valley going below -30 dB in the case of the structure with offset of 80 mm and spacing of 160 mm. By comparing these results with the ones in Figure 29, it can be observed that by parametrising the radius, it is possible to cover a higher range of path gain, whereas with spacing parametrisation, the curve changes are less apparent. Table 7 presents the simulation results in Figure 30 at main frequencies of commercial interest, where the cases with 0 mm of offset at the frequency of 1.8 GHz, the path gain is nearly -10 dB with all spacings, whereas to other offset values, the path gain varies from -27 to -14.7 dB as spacing is increased. Overall, the SE of the structure is improved with the increase in spacing and at the frequencies from 2.4 to 5.9 GHz, the path gain is mostly comprised between -10 to -20 dB.

#### 4.3.3 Triple layer parametric study and layers comparison

In this subchapter, a triple layered structure is proposed, where similarly to the previous subchapter, the spacing between centre of trunks on  $x$ -axis are identical to each layer but the spacing between layers (from the centre of trunks between each

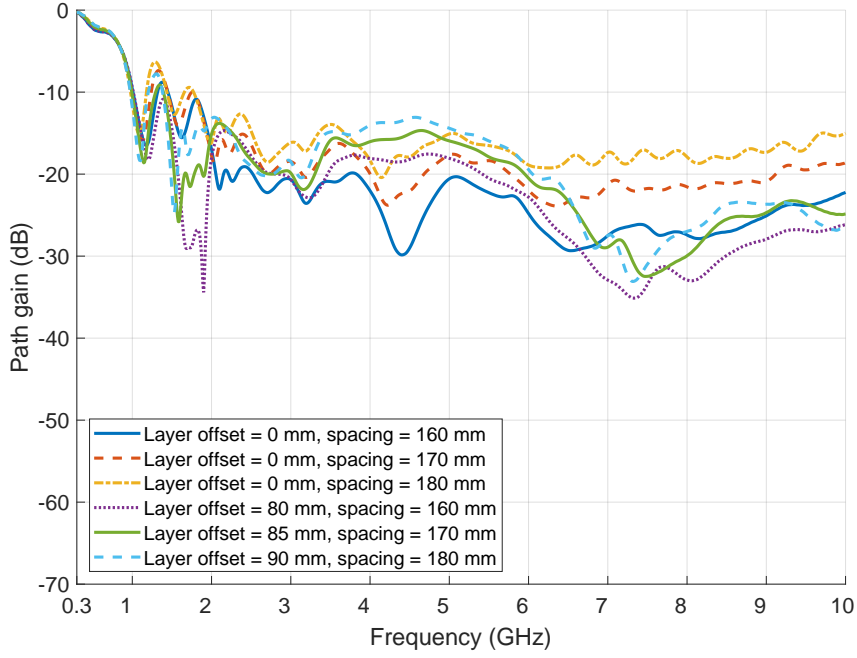


Figure 30: Simulation results with parametrisation of spacing between centre of trunks and layer offset in a double layer configuration with the trunks' radius set to 60 mm.

Table 7: Simulation results with data taken from Figure 30, at frequencies of commercial interest, where spacing between centre of trunks and layer offset are parametrised in a double layer configuration with the trunks' radius set to 60 mm.

Path gain (dB)		Frequency (GHz)			
Layer offset (mm)	Spacing (mm)	1.8	2.4	3.7	5.9
0	160	-10.8	-19.1	-20.1	-23.3
	170	-10.5	-15.1	-16.7	-21
	180	-10.7	-12.8	-15.3	-18.2
80	160	-27	-16.4	-17.9	-22.2
85	170	-19.4	-17	-16.1	-19.4
90	180	-14.7	-18.2	-15.2	-18.2

layer on  $y$ -axis), is fixated to 180 mm, all trunks' radius are equal, irregularities and bending on the poles are excluded from the models. The offset can be set on the middle and upper layer, as illustrated in in Figures 31b, 31c and 31d. This consists in a shift along  $x$ -axis but if the offset is set to 0 mm to both middle and upper layer, this results in symmetrical layers, as depicted in Figure 31a.

In Figure 32 it is presented the parametrisation of trunks' radius, with the spacing between centre of poles set to 180 mm in both  $x$  and  $y$  axis, where no layer offsets are applied. Here, it is observed that by increasing the radius, the shielding capabilities of the structure improves greatly mainly at central to high frequencies, with path gain going below -50 dB at specific points, however, this effect is not so present

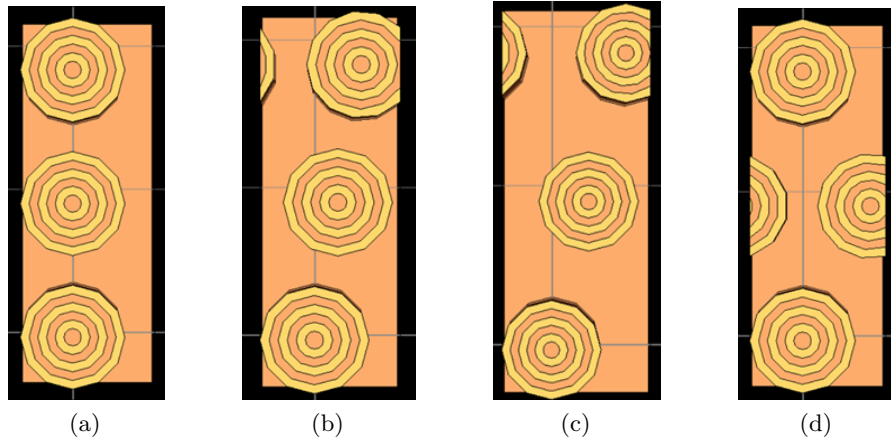


Figure 31: Top view of the structural sample consisting of three layers with no offsets (a), layer 2 with offset of 30 mm and layer 3 with offset of 60 mm (b), layer 2 with offset of 45 mm and layer 3 with offset of 90 mm (c), layer 2 with offset of 90 mm and layer 3 with no offset (d).

at frequencies below 2 GHz. With a radius of 50 mm, the curve is mostly within -10 to -20 dB, while with a radius of 60 mm this curve descends to the range of -20 to -30 dB and the last curve shows that the most of the amplitude can be well below -30 dB. From these simulation results it is obtained the data at commercial frequencies, as shown in Table 8, where at 1.8 GHz, with each increment in radius, the attenuation is increased by nearly 5 dB. This is also seen at 3.7 and 5.9 GHz, where such increments increases attenuation with each step by nearly 12 and 10 dB respectively.

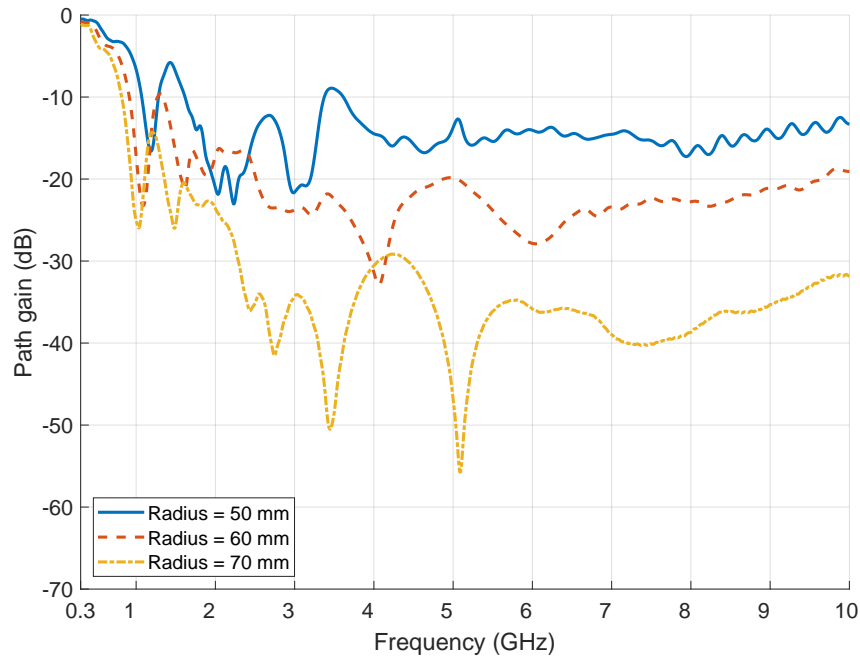


Figure 32: Simulation results with parametrisation of trunks' radius in a triple layer configuration with the spacing between centre of trunks' set to 180 mm.



Table 8: Simulation results with data taken from Figure 32, at frequencies of commercial interest, where trunks' radius is parametrised in a triple layer configuration with the spacing between centre of trunks' set to 180 mm.

Path gain (dB)	
Radius (mm)	Frequency (GHz)
	1.8 2.4 3.7 5.9
50	-13.5 -18.2 -11.6 -14.11
60	-18.2 -16.7 -24.9 -27.3
70	-23.2 -34.9 -36.5 -35.1

In Figure 33 it is presented the simulation results with spacing between centre of trunks within each layer parametrised on  $x$ -axis, and the radius fixated to 60 mm. Similarly to the previous results, no layer offsets, irregularities and poles' bending are introduced to the geometry. By reducing spacing, valleys become notable near 4 and 6.3 GHz, with SE above 50 dB. In general, path gain is increased almost linearly up to 10 dB at higher frequencies with the rise in spacing but this effect is diminished at lower frequencies. With the comparison of these results with the ones in Figure 32, a higher disparity in values is observed with the parametrisation of radius, similarly to the cases with the structure composed of one and two layers. The results in Figure 33 can be summarised to common commercial frequencies as seen in Table 9, where it is viewed small changes with spacing parametrisation at 1.8 and 2.4 GHz, however, it is clear that the structure can provide good shielding at 3.7 and 5.9 GHz since path gain is comprised between -25 to -35 dB.

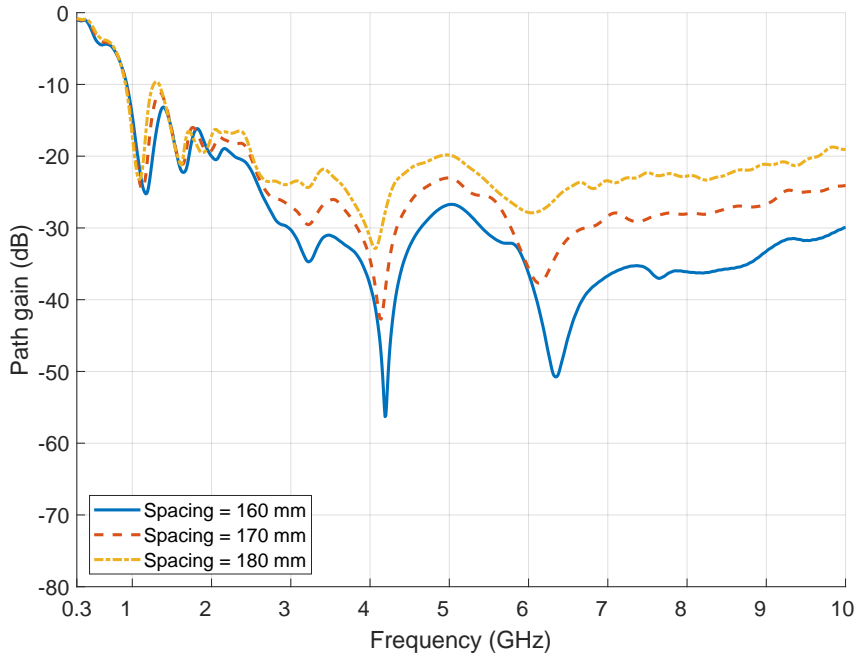


Figure 33: Simulation results with parametrisation of spacing between centre of trunks in a triple layer configuration with the trunks' radius set to 60 mm.

Table 9: Simulation results with data taken from Figure 33, at frequencies of commercial interest, where spacing between centre of trunks is parametrised in a triple layer configuration with the trunks' radius set to 60 mm.

Path gain (dB)				
Spacing (mm)	Frequency (GHz)			
	1.8	2.4	3.7	5.9
160	-16.2	-20.5	-32.5	-33.5
170	-16.4	-18.3	-27.8	-33
180	-18.2	-16.7	-24.9	-27.3

Figure 34 presents the simulation results obtained with parametrisation of layer offset from 0 to 90 mm, and with radius and spacing between centre of trunks fixated to 60 and 180 mm respectively. This shift is attributed separately to the middle layer (layer 2) and upper layer (layer 3) on  $x$ -axis, which corresponds to a de-phase in relation to the bottom layer. This is illustrated in Figure 31, where each model results in the curves seen from the simulation outcome. Here it is viewed that with any offset applied, the SE is improved throughout most of the EM spectrum, with path gain comprising between -20 to -30 dB. The case with offset on layer 2 and 3 of 90 and 0 mm respectively, presents the best shielding at higher and lower frequencies, whilst showing a good transparency at central frequencies in comparison to other cases. The data presented in Table 10 presents these results at specific frequencies where it is seen that at 1.8 and 3.7 GHz, the maximum variation in gain is small, of nearly 3 and 5 dB respectively. The case with layer 2 offset of 30 mm and layer 3 with 60 mm, presents the best general transparency, although the improvement isn't so apparent in these frequencies.

Table 10: Simulation results with data taken from Figure 34, at frequencies of commercial interest, where layers offset are parametrised in a triple layer configuration with the spacing between centre of trunks' set to 180 mm and radius of 60 mm.

Path gain (dB)					
		Frequency (GHz)			
Layer 2 offset (mm)	Layer 3 offset (mm)	1.8	2.4	3.7	5.9
0	0	-18.2	-16.7	-24.9	-27.3
30	60	-16.9	-19.2	-22.1	-21.3
45	90	-18.9	-22.5	-20.7	-32.9
90	0	-15.9	-24.4	-25.9	-25.3

In Figure 35 is presented the simulation results obtained from three models containing different number of layers. The trunks' radius is set to 60 mm, spacing between centre of trunks fixated at 180 mm and no layer offsets performed. With the addition of each layer, it is seen a drop in gain throughout all of the EM spectrum. It is also noticeable valleys at frequencies below 2 GHz, with path gain decreasing

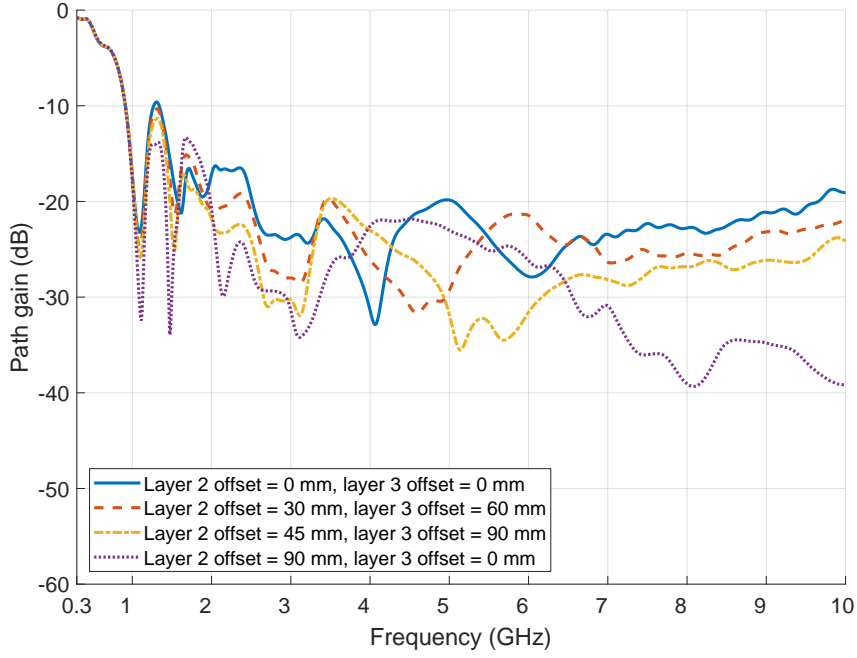


Figure 34: Simulation results with parametrisation of layers offset in a triple layer configuration with the spacing between centre of trunks' set to 180 mm and radius of 60 mm.

from -7 to -23 dB, and at nearly 4 GHz it is seen the same effect with a relative attenuation up to 25 dB. At higher frequencies, it is observed the curves of each structure resembling each other, with path gain being comprised within -10 to -20 dB. From these curves it is extracted the values at frequencies of commercial interest presented in Table 11, where an increased attenuation is seen of nearly 10 dB by implementing a third layer to a double layered structure. The SE of the barrier with increasing number of layers stands out the most at 3.7 and 5.9 GHz, although it is clear that a single layer provides the best transparency capabilities.

Table 11: Simulation results with data taken from Figure 35, at frequencies of commercial interest, where the number of layers in the structure are compared.

Number of layers	Path gain (dB)			
	Frequency (GHz)			
	1.8	2.4	3.7	5.9
1	-7.9	-11.2	-7.1	-13.3
2	-10.7	-12.8	-15.3	-18.2
3	-18.2	-16.7	-24.9	-27.3

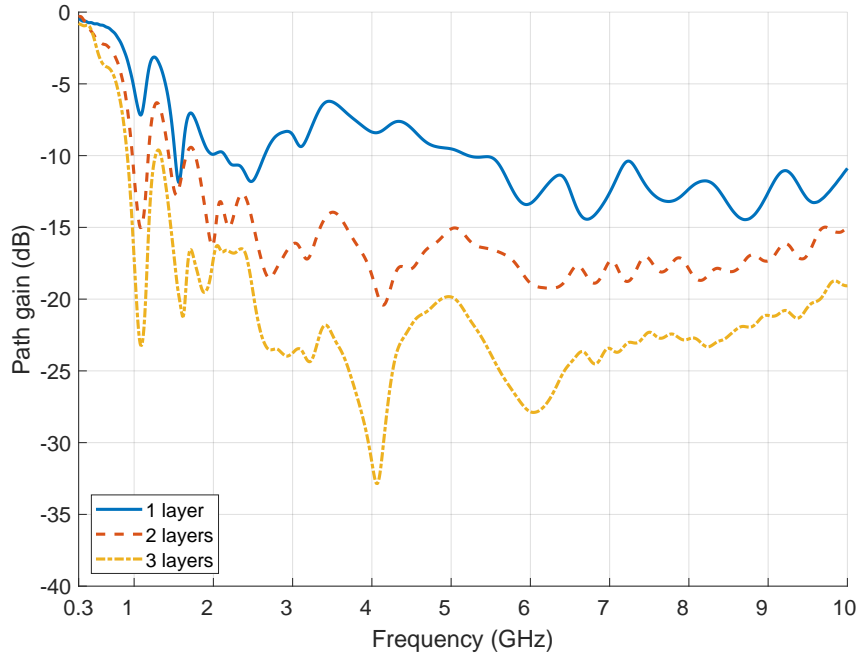


Figure 35: Simulation results showing the comparison of number of trunk layers in the structure.

#### 4.3.4 *Moisture content, surface roughness, trunks' bending and other parameters assessment*

In this subchapter, it is evaluated the behaviour on the EM spectrum caused parametrisations of MC within trunks, its irregularities, bending and polarisation in a structure composed by a single layer with spacing between centre of poles and its radius of 180 and 60 mm respectively, at the frequency range of 0.3 to 10 GHz. The trunks height is of 2.27 m and the structure is enclosed with periodic boundaries on  $x$ -axis.

Figure 36 presents the results with parametrisation of MC at the ranges of 10% to 30%, 20% to 40% and 30% to 60% on a structure without surface roughness and bending. It is viewed that increasing the MC range affects the SE of the structure greatly at frequencies below 2 GHz, with minimum peaks being presented with path gain below -25 dB since permittivity is higher at lower frequencies, however, the opposite is seen at frequencies above this threshold, where the curves are found between -10 to -15 dB. Since the range of 10% to 30% corresponds to values of  $\epsilon'$  around 3.2, which is the measured quantity in [16], it is used these MC values as a reference throughout most of this dissertation.

In Figure 37 is presented the simulation results of the structure with no added bending on trunks, where it is performed diverse parametrisations on irregularities. This includes parametrisations beyond the values associated to each default variable as seen in Table 1, with the inclusion of a default value of 5 for the number

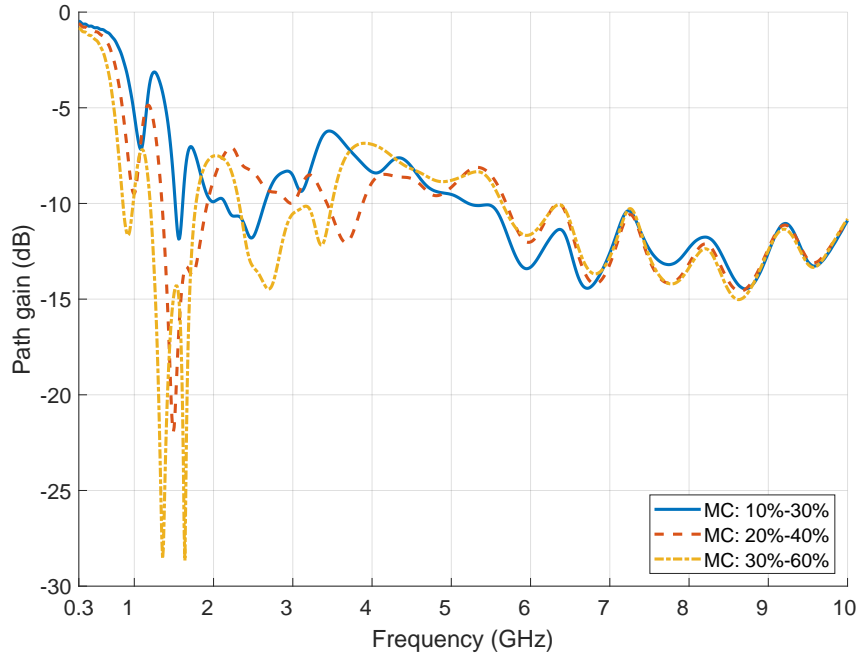


Figure 36: Simulation results showing the comparison of structures with different MC ranges in the trunks.

of longitudinal layers. In the results, besides one curve possessing solely default parameters on surface roughness, each curve corresponds to a model associated with the default parameters with specific exceptions on each simulated structure, which can be found ordered in the legend of the depicted figure. This consists in parametrisation of the number of longitudinal layers, number of irregularities in a longitudinal layer, the irregularities radius and height. The variables altered from its default value does not change the response of the barrier at all, however, there's a clear indication that by increasing the number of irregularities and its radius, this could lead to a different spectrum shape, mainly at higher frequencies, as seen in the bottom curve.

To simulate the effect of the bending on the trunks, five structures are constructed with the developed algorithm by running the same number of iterations with the default parameters presented in Table 2. The geometry consist in a layer composed by four trunks, as seen in Figure 38, where each generated case is unique. The resulting curves are seen in Figure 39, where each case presents similarities in gain throughout the spectrum, although close to the frequency of 2 GHz, it can be observed high attenuation valley on case 5 but despite this occurrence, path gain remains alike with each curve.

Parametrisation on polarisation is performed on the structure, with the electric field angle fixated to either  $0^\circ$  (vertical polarisation) or  $90^\circ$  (horizontal polarisation). The obtained results have shown to be exactly the same to either angle, which will be seen in the next chapter.

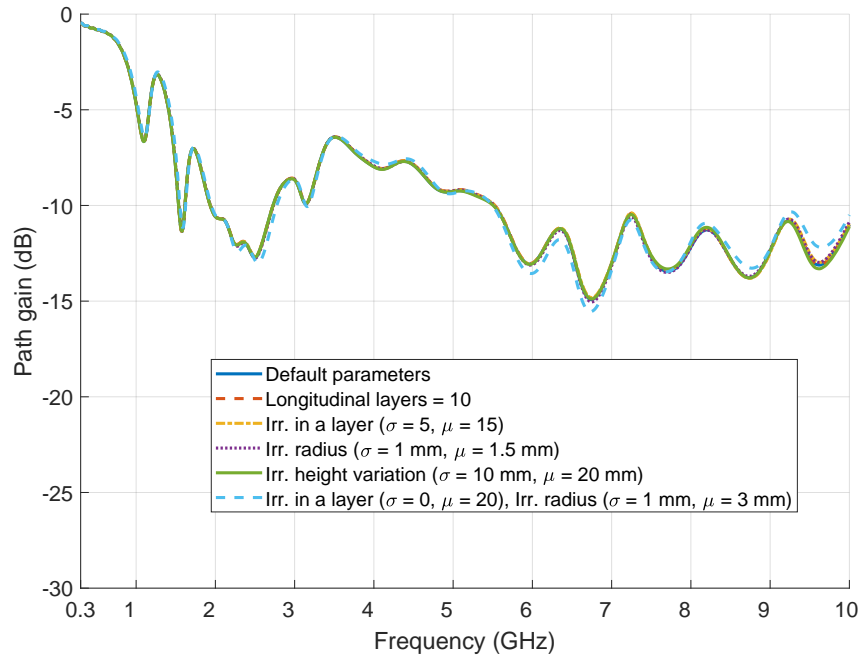


Figure 37: Simulation results showing the comparison of structures with diverse surface roughness parametrizations.

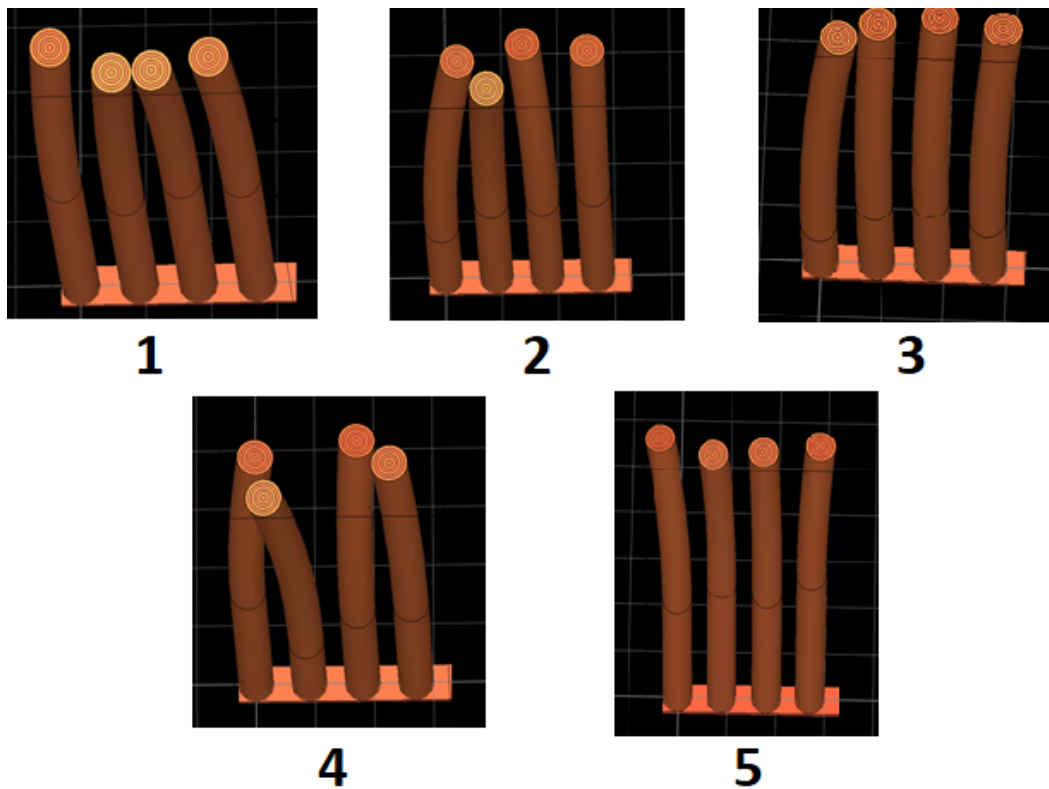


Figure 38: Five cases of unique degrees of bending on structures.

#### 4.4 INTERIM CONCLUSIONS

This chapter presents the developed models and its simulation results where it is performed parametrizations with the simulated frequency range comprised between

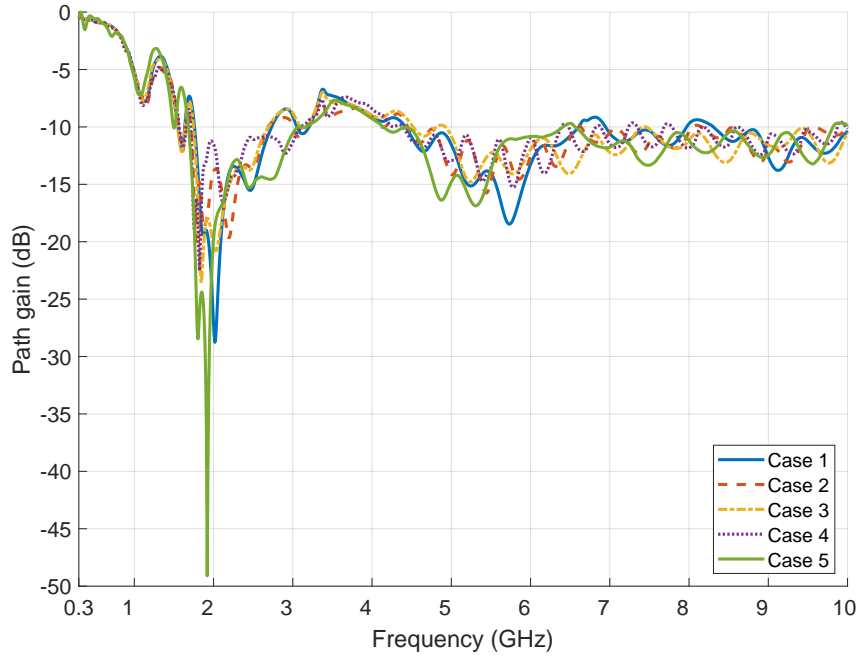


Figure 39: Simulation results showing the comparison of structures with different degrees of trunk bending.

0.3 to 10 GHz and boundary conditions set to either periodic or open on  $x$ -axis. It is viewed from the simulation results of a  $3 \times 3$  sample with open boundaries at the frequency range of 0.7 to 5.9 GHz, where MC, irregularities and bending of trunks are applied to the structure and here it can be seen that MC causes a drastic attenuation with an average of 17.81 dB, while irregularities and bending caused minor changes to the EM spectrum. With the same simulation settings and the absence of MC, a  $3 \times 9$  structure is studied with the parametrisation of spacing between trunks, which results in a spectrum shift with the increase of spacing. Simulation are performed with a structure composing of one to three layers with periodic boundaries, where it is seen that by increasing the trunks radius, valleys are shifted at lower frequencies and overall SE is improved, whereas increasing spacing between centre of trunks enhances the transparency capabilities of the structure, mainly at higher frequencies. Here it is also seen that introducing more layers and performing a layer shift generates a drop in gain across all of the spectrum. parametrisation results of MC shows how frequencies below 2 GHz are greatly affected since permittivity is higher as MC increases, while the insertion of irregularities on the trunks' surface does not cause any substantial change. The application of bending on the trunks results in a small shaping of the spectrum, although depending on the viewed case study, a great attenuation can be seen near 2 GHz.

This page is intentionally left blank.



## MEASUREMENT SETUP AND BARRIER VALIDATION

---

### 5.1 INTRODUCTION

This chapter presents the environment description with the equipment configurations and measurements conducted in the anechoic chamber of a real scale prototype composed of periodically arranged timber logs, where its EM shielding and transparency capabilities are assessed with different spacing between centre of trunks and multiple angles of radio propagation incidence.

### 5.2 BARRIER ASSEMBLY AND ENVIRONMENT PREPARATION

Prior to the installation of the wooden structure prototype, it is analysed a batch of thirty trunks whose characteristics can be found in Appendix B, where the mean height is of 2270 mm, and mean top, middle and bottom radius of 56, 58 and 62 mm respectively. Ten poles are selected to assemble a single layer in the anechoic chamber located in Polytechnic of Leiria, which can be visualised in Figure 40, and here it can be seen that the barrier is supported by two rods that cross the bottom of each pole and two metallic structural supports fixated to the sides. Two trunks are added as weight to the bottom of the structure to keep the barrier vertical and to avoid accidental tumbling.

The schematic for the measurement setup is presented in Figure 41, where the used TX antenna is Aaronia Hyperlog 60100 and RX antenna is an antipodal Vivaldi, where the latter's frequency range is comprised between 1.5 to 10 GHz. Both antennas are at a height of 1.2 m from the ground and are connected to a Rhode & Schwartz ZVM Vector Network Analyser (VNA), where the frequency response is acquired. The used high frequency cables contributes to a high attenuation at higher frequencies, as shown in Figure 42, mainly due to the length of the 15 m cable connected to the RX which causes an attenuation of up to 17 dB at 10 GHz, as this can lead to erroneous measurements as a result of the system's dynamic range. As such, the start and stop frequency are set to 1.5 and 6 GHz respectively, and the cable connected to the TX has been reduced to 4.4 m.

The TX and RX antennas rotate around the centre of turntables at angles  $\theta_1$  and  $\theta_2$ , to a minimum and maximum of  $-45^\circ$  and  $45^\circ$  respectively, being  $\theta_1 = \theta_2 = 0^\circ$

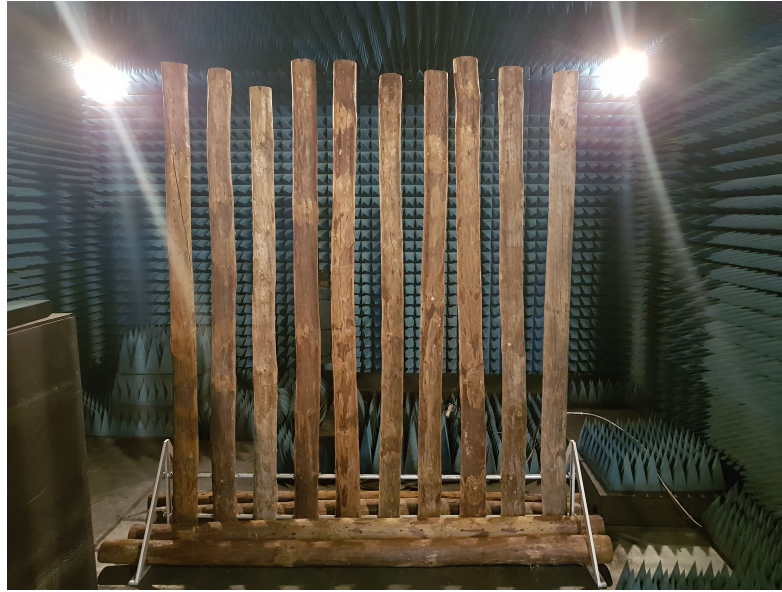


Figure 40: Log barrier prototype assembled in the anechoic chamber.

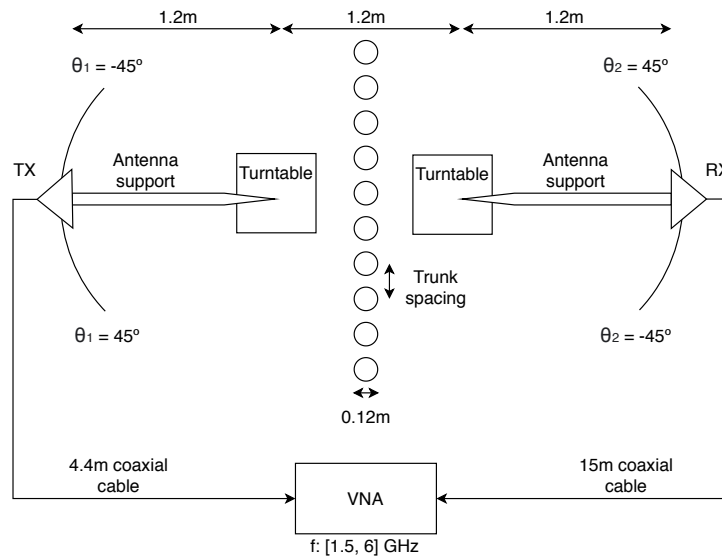


Figure 41: Measurement geometry and setup.

the angle at which the antennas are perpendicular to the barrier. Both antennas polarisation are set manually on their respective supportive structure. During measurements, it is obtained the frequency response three times at each angle and posteriorly it is calculated the mean value in order to reduce the possible effects of signal fluctuation. EM pyramidal absorbers are placed throughout all non obstructing areas, where special care is taken to cover all metallic surfaces to avoid signal reflection and therefore, data contamination. In Figures 43a and 43b it is seen the barrier along with the equipment covered with absorbers from the perspectives of TX and RX.

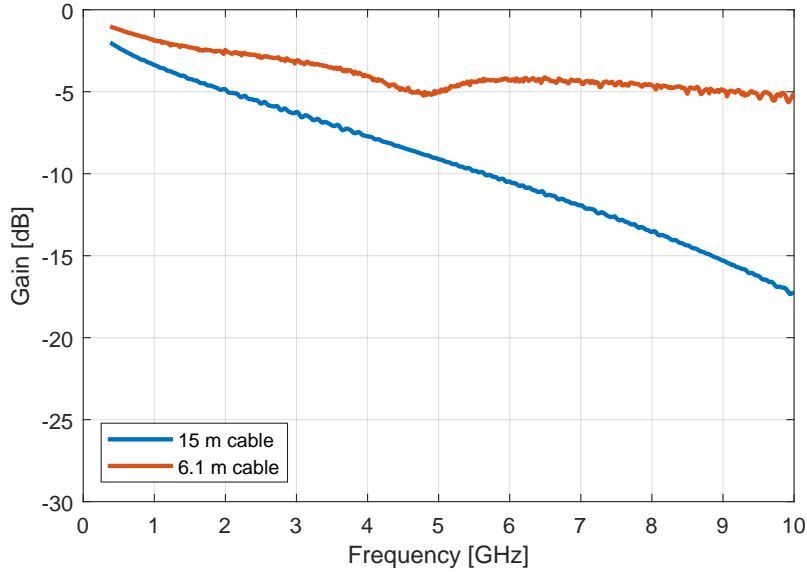


Figure 42: Attenuation caused by used cables before the final setup.

Before commencing a measurement campaign, it is crucial to calibrate the [VNA](#) so that the power transmitted at the plane of calibration of each port is 0 dB across all of the determined frequency range [37]. The calibration procedure consists in:

- Measurement of through-connection between ports 1 and 2;
- Measurement of open circuit at port 1 and 2;
- Measurement of short circuit at port 1 and 2;
- Measurement of matched termination at port 1 and 2;
- Calibration termination and data correction calculation.

### 5.3 BARRIER EVALUATION AND DISCUSSION

This subchapter presents the explanation on how data is processed and results from conducted measurements are compared with simulation results at the frequency range of 1.5 to 6 GHz, where spacing between trunks are parametrised from 160 to 200 mm at the antennas' height, being these rotated from  $-45^\circ$  to  $45^\circ$ , around the respective turntables.



Figure 43: The assembled barrier and equipment from the perspective of TX (a) and RX (b).

### 5.3.1 *Measurement post-processing*

In order to acquire the SE of the barrier, it must be removed the effects caused by the radiation pattern of antennas, the attenuation from cables and path between antennas. For this purpose, measurements with the same setup in Figure 41 and barrier excluded are performed to subtract the before-mentioned effects on the structure's measurements, as seen in Figure 44, and therefore, normalise the acquired data.



Figure 44: Setup for free space measurements.

The free space measurements at frequencies of commercial interest can be found in Appendix C, and in Figure 45 can be seen an example of these measurements at the frequency of 2.4 GHz, with vertical and horizontal polarisation, where most of the radiated power can be found near the angles  $\theta_1 = \theta_2$ , corresponding to antennas facing each other. Here it is also observed that vertical polarisation at this frequency provides a wider angular range when compared to that of the horizontal polarisation.

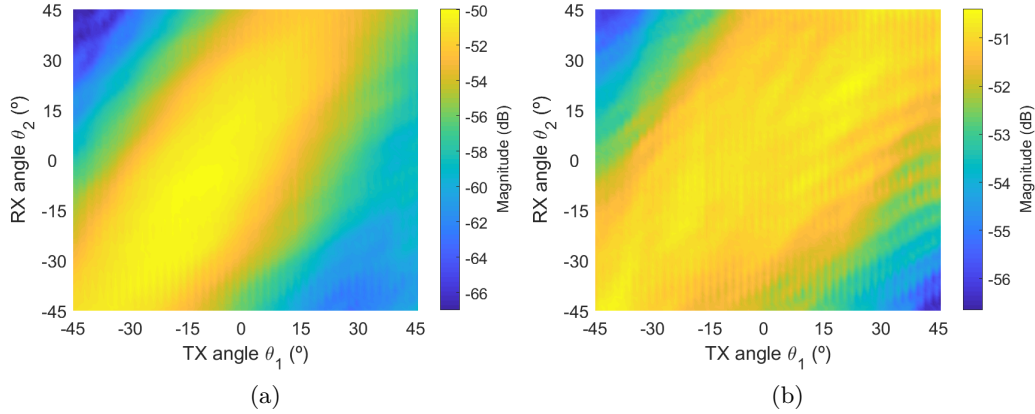


Figure 45: Free space measurement in a multi-angular setup at 2.4 GHz, with antennas horizontally (a) and vertically (b) polarised.

### 5.3.2 Measurement results on normal incidence

The measurement results are obtained with TX and RX antennas perpendicular to the wooden structure ( $\theta_1 = \theta_2 = 0^\circ$ ) which are then normalised, and compared to the simulation results presented in the previous chapter.

Figures 46, 47 and 48 present the simulation and measurement results with antennas vertically and horizontally polarised, and the barrier's pole spacing of 160, 180 and 200 mm respectively. The simulation results confirms no polarisation dependency for each pole spacing, as the curves are overlapped, while the measurements appears to be slightly different from the expected curve. However, it can be seen that the SE of both simulation and measurement shows a reasonably good agreement across the frequency band. It is notable the presence of deep fades, mainly starting from 5 GHz for horizontal polarisation, which ensures a better EM shielding. The measurement results performed with vertical polarisation are similar to horizontal, apart from the valleys seen at 1.9 GHz in Figure 46 and from 2.5 to 3,25 GHz in Figure 48. It should be noted that through the parametrisation of the spacing, the bending of the trunks was altered due to the structure's stability, which can cause significant impact on the spectrum, as seen in the simulations performed in Figure 39.



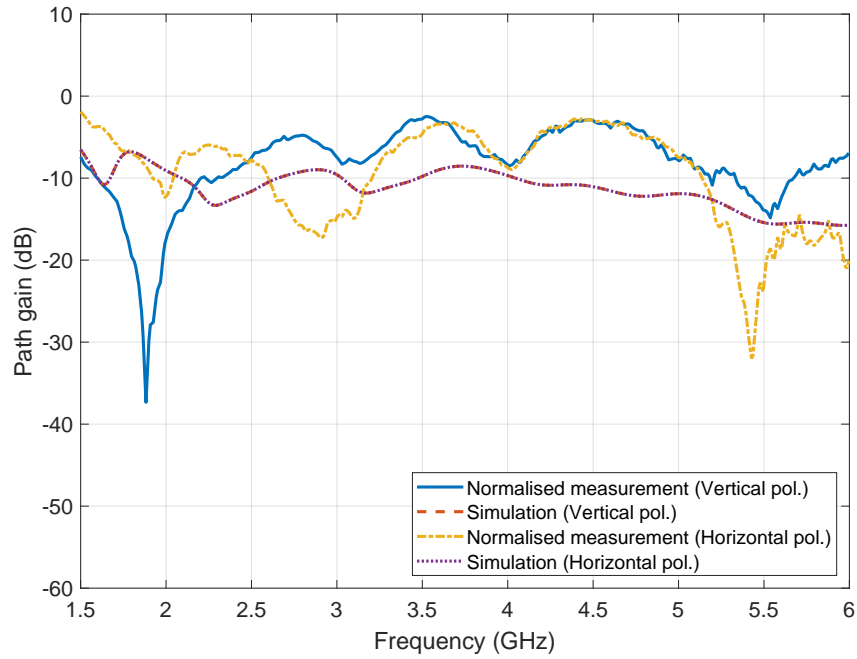


Figure 46: Simulation results versus measurement results with both horizontal and vertical polarisation of a single layer with spacing between centre of trunks of 160 mm.

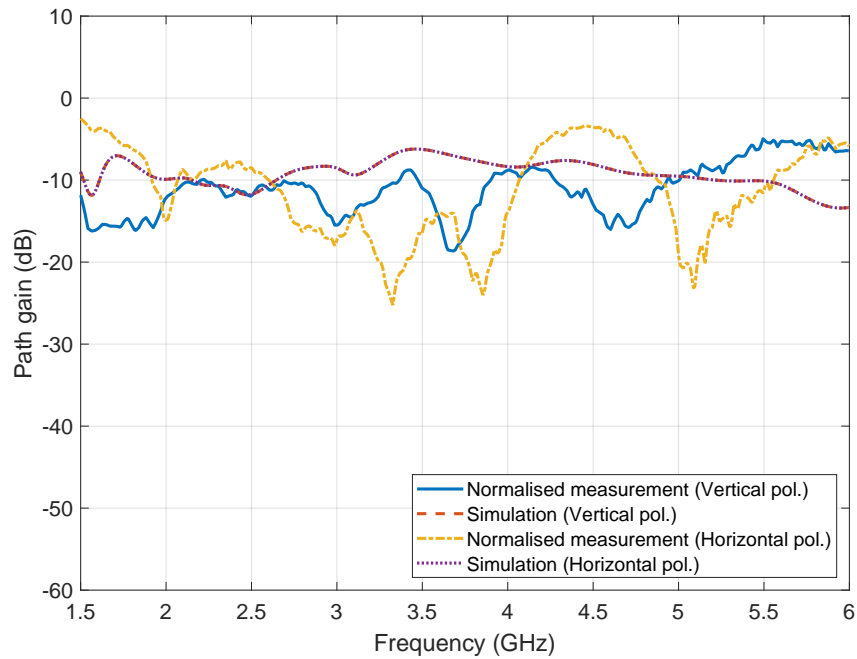


Figure 47: Simulation results versus measurement results with both horizontal and vertical polarisation of a single layer with spacing between centre of trunks of 180 mm.

From the Figures 46, 47 and 48, it is extracted the mean SE at frequency bands of 3.4 to 3.8 GHz and 5.855 to 5.925 GHz from the measurements performed in the anechoic chamber, as seen in Table 12. Here, The overall path gain of the structure is higher with vertical polarisation, especially at the frequency band of 5.855 to 5.925, whereas a good shielding is mostly viewed with horizontal polarisation. Increasing the spacing also generally improves the transparency of the barrier with vertical

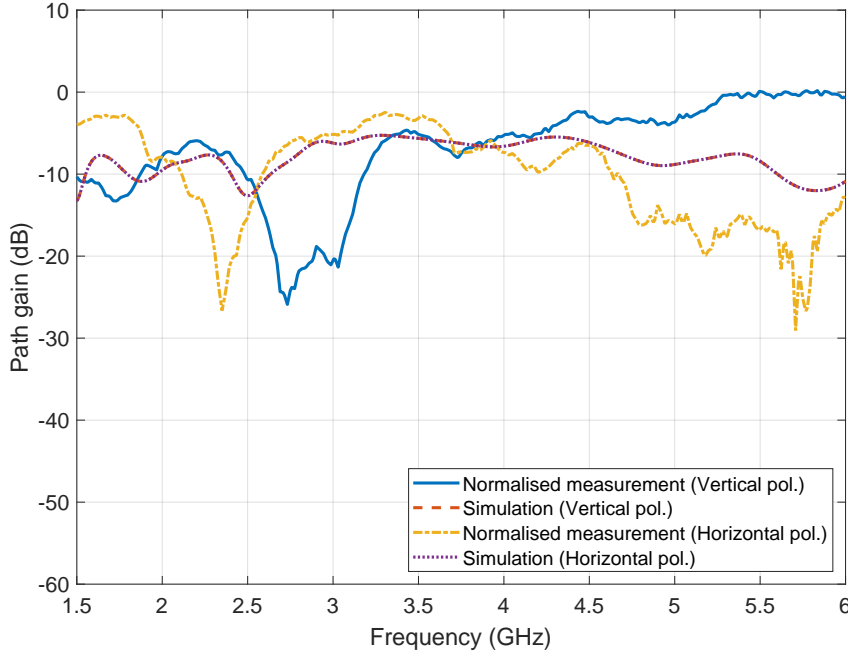


Figure 48: Simulation results versus measurement results with both horizontal and vertical polarisation of a single layer with spacing between centre of trunks of 200 mm.

polarisation, although it is seen high attenuation for a spacing of 180 mm. From these results, the best shielding configuration at the frequency band of 3.4 to 3.8 GHz consists in a structure set with spacing of 180 mm with either polarisation, and spacing of 160 mm at the frequency band of 5.855 to 5.925 GHz. The best transparency is obtained with a spacing of 160 mm at the frequency band of 3.4 to 3.8 GHz, while for the frequency band of 5.855 to 5.925 GHz it is a spacing of 200 mm for vertical polarisation and 180 mm with horizontal polarisation.

Table 12: Mean **SE** acquired from measurements on normal incidence with spacing between centre of trunks from 160 to 200 mm with antennas vertically and horizontally polarised.

		Path gain (dB)	
		Frequency band (GHz)	
Polarisation	Spacing (mm)	3.4 - 3.8	5.855 - 5.925
Vertical	160	-3.6	-8.1
	180	-12.7	-6.1
	200	-6.0	-0.1
Horizontal	160	-4.0	-16.6
	180	-16.2	-5.4
	200	-4.3	-15.4

Table 13 presents the **RMSE** based on mean **SE** obtained from the simulation and measurement results presented in Figures 46, 47 and 48 at frequency bands of 3.4 to 3.8 GHz and 5.855 to 5.925 GHz, where the error is minimal with a spacing of 200

mm at the frequency band of 3.4 to 3.8 GHz and the error is higher at frequency band of 5.855 to 5.925 GHz, with vertical polarisation. Overall, the measurements presents a reasonable agreement with the simulation results at the specified bands, despite the poles having some degree of bending which causes variable spacing throughout the length of the trunks and **MC** needing to be confirmed since humidity measurements could not be performed during the period of **EM** measurements campaign.

Table 13: **RMSE** based on mean **SE** between simulations and measurements on normal incidence with spacing between centre of trunks from 160 to 200 mm with antennas vertically and horizontally polarised.

<b>RMSE</b>			
		<b>Frequency band (GHz)</b>	
<b>Polarisation</b>	<b>Spacing (mm)</b>	3.4 - 3.8	5.855 - 5.925
Vertical	160	5.5	7.5
	180	6.0	7.1
	200	0.2	11.7
Horizontal	160	5.2	0.9
	180	9.4	7.9
	200	1.6	3.5

### 5.3.3 *Measurement results on a multi-angular setting*

Here, measurements are performed and normalised with horizontal and vertical polarisation, at **TX** and **RX** angles of  $-45^\circ \leq \theta_1 \leq 45^\circ$  and  $-45^\circ \leq \theta_2 \leq 45^\circ$  for a total of 91 x 91 angles, with the results being shown at the frequencies of 1.8, 2.4, 3.7 and 5.9 GHz, where the obtained results are briefly explained. Additionally, statistical analysis of the measured data is realised to evaluate the structure's impact on radio propagation.

The complete normalised measurement results at commercial frequencies can be found in Appendix D, and the figures in 49 present an example of measurement results performed with spacing parametrised, horizontal and vertical polarisation at 2.4 GHz, where it is visible the barrier's pattern since it effectively lowers signal level. Increasing spacing with horizontal polarisation shows an increased overall transparency, while with vertical polarisation, a higher transparency is notable with a spacing of 160 mm. The results with vertical polarisation presents a generally higher **SE** when compared to that of horizontal polarisation. With a spacing of 180 mm, it is viewed less values variation with either polarisation. In these figures it is also observed positive path gain, which could be due to the reflective and dispersive



characteristics of the barrier as these factors can improve signal concentration at the RX on specific angles.

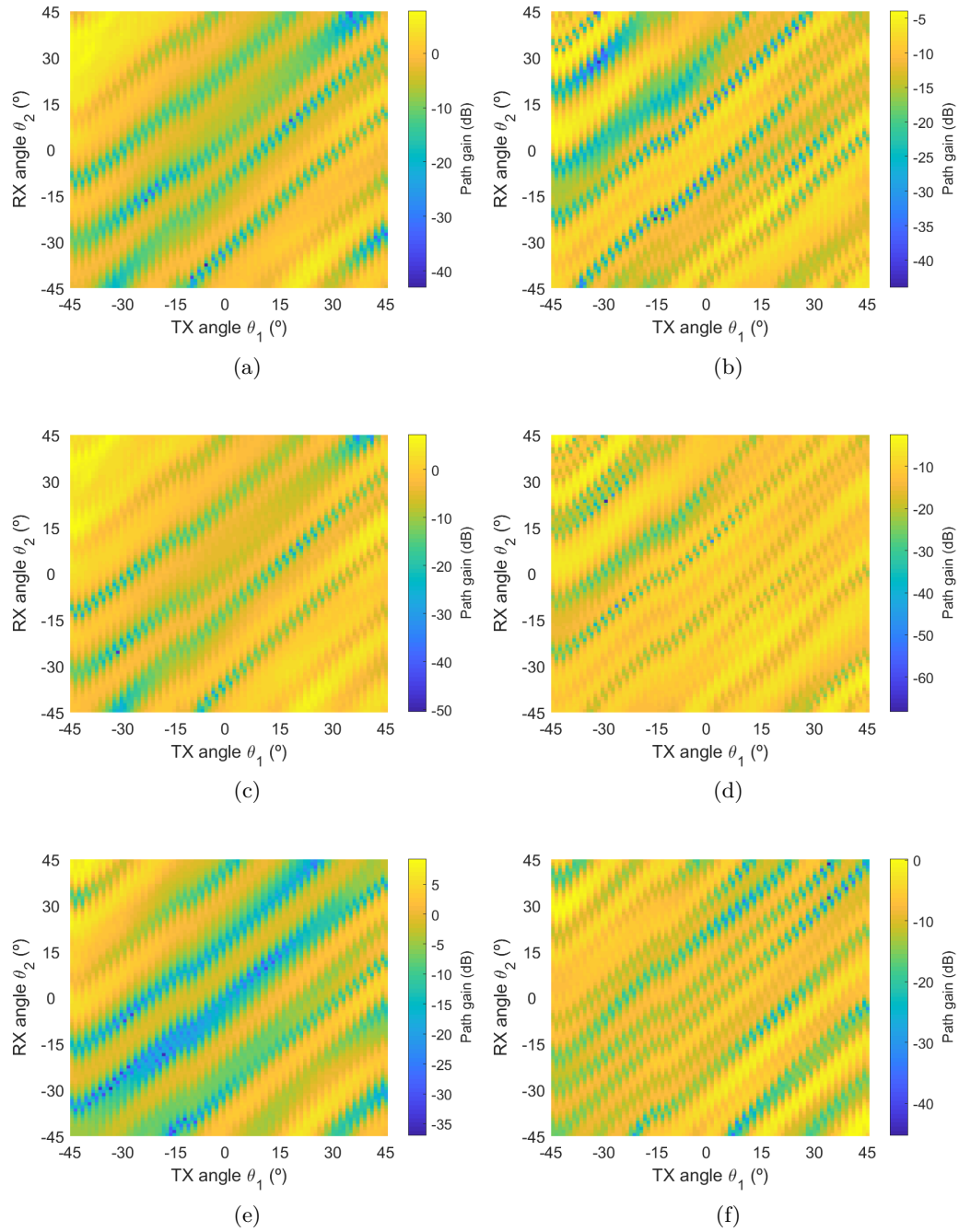


Figure 49: Graphs presenting normalised measurement results at 2.4 GHz with antennas horizontally polarised and spacing between centre of trunks of (a) 160, (c) 180 and (e) 200 mm, and antennas vertically polarised with spacing of (b) 160, (d) 180 and (f) 200 mm.

The figures in 50 present the normalised measurement results at the frequencies of 1.8, 2.4, 3.7 and 5.9 GHz, with horizontal polarisation and spacing between centre of trunks set to 180 mm. Here it is seen an increased transparency with a smooth variation throughout most of the angles at 1.8 and 2.4 GHz, whereas at 3.7 and 5.9

GHz the data value discrepancy between angles is higher. However, a noticeable consistency in SE is observed near TX and RX antenna angles  $-\theta_1 = \theta_2 = 15^\circ$  at all presented frequencies, where the attenuation is relatively lower when compared to neighboring angles.

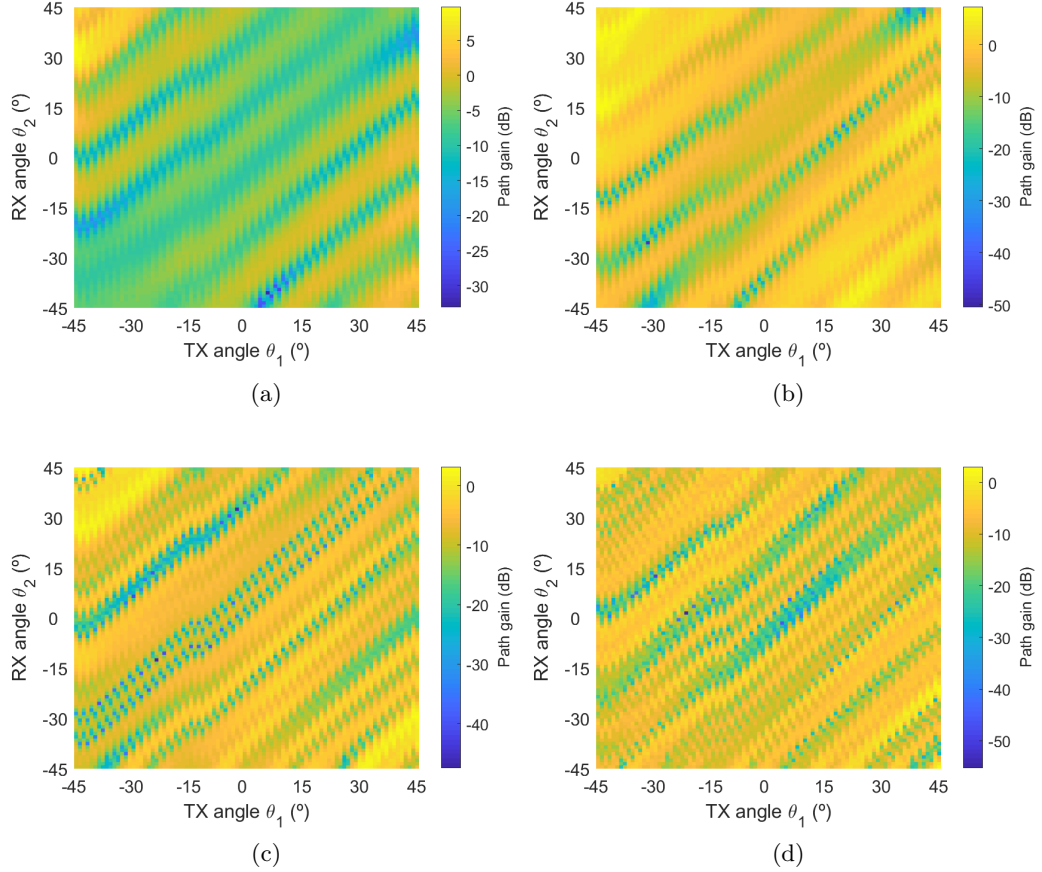


Figure 50: Graphs presenting normalised measurement results with antennas horizontally polarised and spacing between centre of trunks of 180 mm, at frequencies of (a) 1.8, (b) 2.4, (c) 3.7 and (d) 5.9 GHz.

In the figures presented in 49 and 50, the antennas' LoS is not obstructed by the trunks at all near the angles  $-\theta_1 = \theta_2 = 45^\circ$  and  $-\theta_1 = \theta_2 = -45^\circ$ . To diminish this undesired effect, a Cumulative Distribution Function (CDF) is applied on the data at angles  $-20^\circ \leq \theta_1 \leq 20^\circ$  and  $-20^\circ \leq \theta_2 \leq 20^\circ$  for a total of 41 x 41 angles, which also eases the measurements analysis.

Figures 51, 52 and 53 present the CDF performed on measurement data at 160, 180 and 200 mm respectively, where it is observed an overall path gain decrease with vertical polarisation when compared to horizontal polarisation, especially at lower frequencies. The cumulative probability associated to the path gain of -10 dB is seen to be around 20% to 30% for horizontal polarisation and 40% to 60% for vertical polarisation, which suggests a generally good transparency with the shown trunks' spacings.

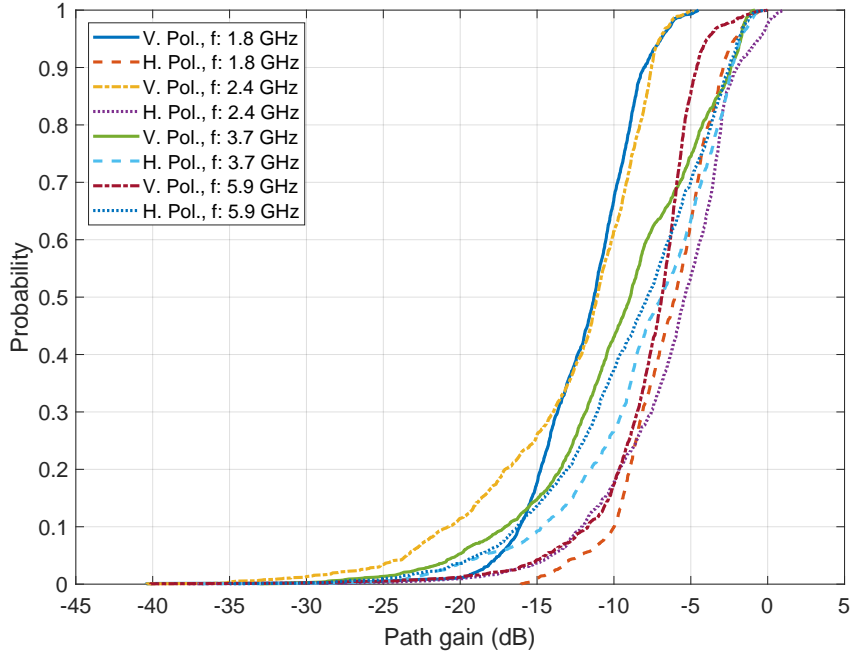


Figure 51: CDF of normalised measurements with spacing between centre of trunks of 160 mm and antennas at angles ranging from  $-20^\circ \leq \theta_1 \leq 20^\circ$  and  $-20^\circ \leq \theta_2 \leq 20^\circ$ .

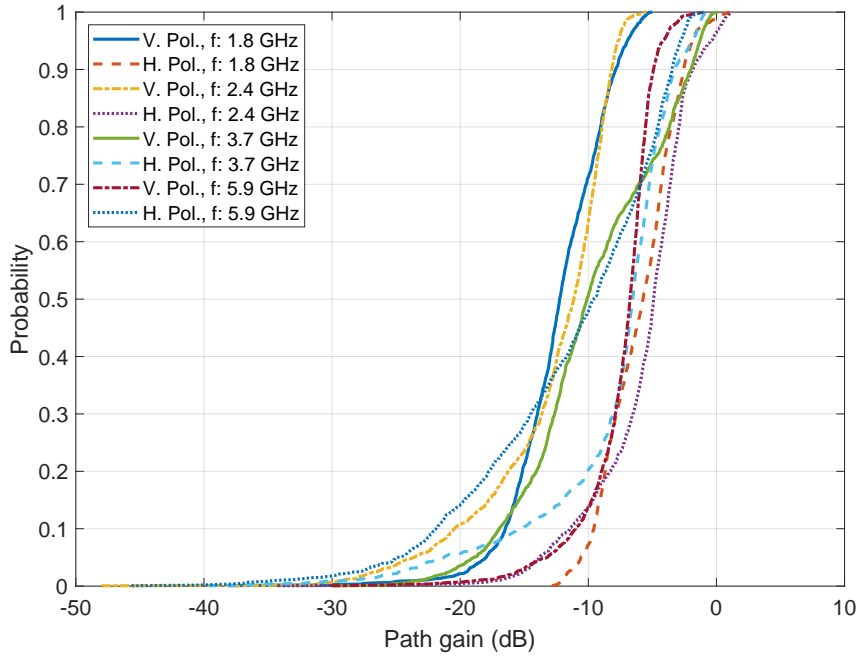


Figure 52: CDF of normalised measurements with spacing between centre of trunks of 180 mm and antennas at angles ranging from  $-20^\circ \leq \theta_1 \leq 20^\circ$  and  $-20^\circ \leq \theta_2 \leq 20^\circ$ .

From the Figures 51, 52 and 53, it is extracted the values at the cumulative probabilities of 5%, 50% and 95%, as seen in Tables 14. With a cumulative probability of up to 5%, path gain is mostly decreased at 1.8 and 5.9 GHz with the raise in spacing for vertical polarisation, while the opposite is visualised at 2.4 and 3.7 GHz, even though the cases with a spacing of 160 and 180 mm present similar magnitude. With horizontal polarisation, path gain is lowest at 1.8 and 2.4 GHz

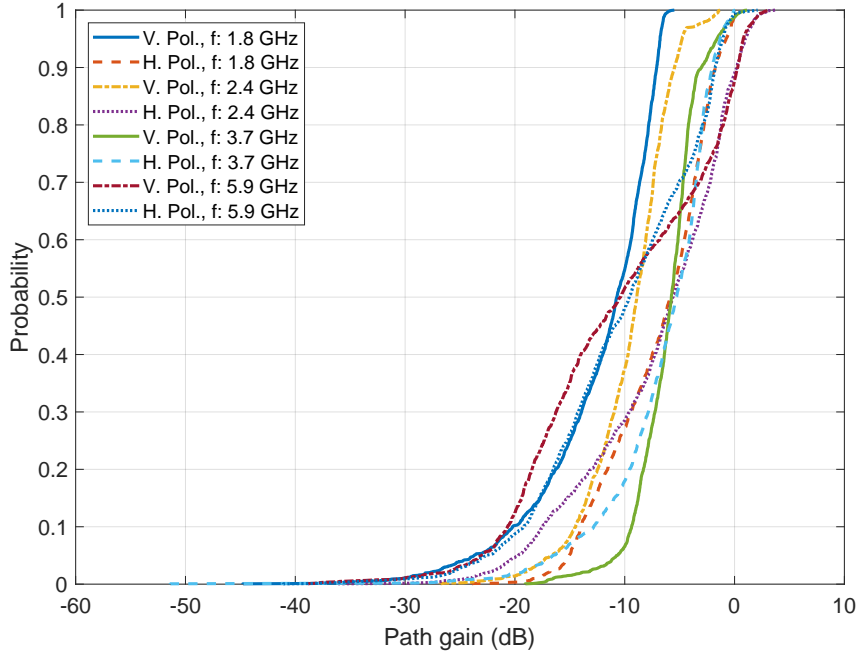


Figure 53: CDF of normalised measurements with spacing between centre of trunks of 200 mm and antennas at angles ranging from  $-20^\circ \leq \theta_1 \leq 20^\circ$  and  $-20^\circ \leq \theta_2 \leq 20^\circ$ .

of all presented spacings, while at 3.7 and 5.9 GHz it is the highest, with a nearly 10 dB increase. At all presented frequencies it is viewed a generally low variation in path gain with probability up to 50%, as each spacing between centre of trunks increases with either vertical or horizontal polarisation, where it is also observed a gain equal to nearly -10 dB in most cases, similarly to the simulation results examined in the previous subchapter. The cases with cumulative probability up to 95% also presents low fluctuation and by comparing these numbers to the ones with cumulative probability of 50%, the values are seen to range by nearly 5 dB, between each probability case, while comparing with a cumulative probability up to 5%, the variation goes as high as nearly 13 dB.

In conclusion, with the analysis of this results, the ideal configuration for a better general transparency at the discussed frequencies is with a spacing between centre of poles set to 200 mm for either polarisation, while the best spacing for increased shielding is of 180 mm, albeit being quite comparable to a structure with a spacing of 160 mm.

#### 5.4 INTERIM CONCLUSIONS

This chapter presents the measurement setup with the equipment used and main parameters, followed by the normalisation procedure of the results. Afterwards, comparison of measurement results with parametrisation of spacing between centre of trunks and simulation results are studied on normal incidence, where a reasonable

Table 14: CDF of normalised measurements at commercial frequencies with antennas at angles ranging from  $-20^\circ \leq \theta_1 \leq 20^\circ$  and  $-20^\circ \leq \theta_2 \leq 20^\circ$ .

		Path gain (dB)							
Freq. (GHz):		1.8		2.4		3.7		5.9	
Pol. <sup>a</sup> :		V	H	V	H	V	H	V	H
Spacing	5%*	-17.4	-12.3	-23.5	-14.1	-20.2	-18.5	-14.5	-18.9
of	50%*	-11.3	-6.1	-11.1	-5.4	-8.9	-6.9	-6.9	-7.8
160 mm	95%*	-6.9	-2.1	-7.0	-0.6	-1.7	-1.8	-3.9	-1.9
Spacing	5%*	-18.0	-10.6	-23.6	-13.8	-18.9	-21.3	-13.2	-24.9
of	50%*	-12.2	-5.7	-11.1	-4.9	-10.1	-6.5	-6.7	-9.6
180 mm	95%*	-6.9	-1.9	-7.7	-0.4	-1.3	-1.9	-4.2	-2.8
Spacing	5%*	-23.7	-15.1	-16.7	-19.7	-10.7	-16.5	-23.1	-22.5
of	50%*	-10.7	-5.8	-8.9	-5.6	-5.8	-5.3	-10.4	-9.6
200 mm	95%*	-6.8	-0.8	-4.8	1.0	-1.6	-1.3	0.8	-1.0

<sup>a</sup> Vertical (V) polarisation or horizontal (H) polarisation.

\* Cumulative probability.

agreement is seen across the frequency band and RMSE being generally lower with vertical polarisation at the frequency band of 5.855 to 5.925 GHz, although it presents best transparency in measurements. The results of measurements performed in a multi-angular configuration with TX and RX angles of  $-45^\circ \leq \theta_1 \leq 45^\circ$  and  $-45^\circ \leq \theta_2 \leq 45^\circ$  are shown, where it is seen a higher SE with vertical polarisation and high discrepancy of values between angles at higher frequencies. A CDF is applied on the measured data on angles  $-20^\circ \leq \theta_1 \leq 20^\circ$  and  $-20^\circ \leq \theta_2 \leq 20^\circ$ , where it is observed that the overall path gain is decreased at lower frequencies, with vertical polarisation. A low variation of values are also visualised with higher cumulative probability, and finally, it is concluded that the spacing of 200 mm presents best transparency at the presented frequencies for either polarisation, while with a spacing of 160 or 180 mm, the results are similar and with a generally improved SE.

This page is intentionally left blank.

## CONCLUSION

---

### 6.1 INTRODUCTION

This chapter addresses the conclusions of the work presented in this dissertation. A summary of the performed work is shown with a review of each chapter, followed by the contributions to the knowledge and finally, the future work is proposed.

### 6.2 DISSERTATION REVIEW

The main scope of this dissertation aimed at the **EM** characterisation of a wooden barrier for roadside application. To achieve this objective, a literature review was presented to better understand wood related parameters and radio propagation definitions. A script was developed in MATLAB to build and characterise the barrier with multiple configurations within the simulation environment. Different barrier designs and parametrisations were performed to assess the **SE** capabilities of the structure throughout the defined frequency range, where it was seen in general, the increase of number of layers and radius, and decrease of spacing resulted in a better shielding. Finally, measurements with parametrisation of spacing between centre of trunks were conducted with diverse **TX** and **RX** angles, and the results were analysed at the frequencies of commercial interest. here it was seen that the best structure configuration for a better transparency is with spacing between centre of poles set to 200 mm for the frequencies of 1.8, 2.4, 3.7 and 5.9 GHz, while the spacing of 180 mm increases shielding, although the results with this spacing is very similar to the case with a spacing of 160 mm.

In Chapter 1, background study and motivation behind the proposed barrier was presented, with the enumeration of this work's objectives and dissertation layout.

Chapter 2 provided a literature review on wood related parameters such as acquisition of **MC** and permittivity. The characteristics of radio propagation and a radio channel was studied, along with the attainment of **SE** of a structure.

The contents of Chapter 3 focus in the development of a script for automatic barrier modelling in **CST**. Here it was seen the how the geometry is generated

and humidity in the poles are introduced, with the possibility of adding surface roughness and bending on trunks.

In Chapter 4, simulations were performed with the parametrisation of spacing between centre of trunks and radius, along with parametrisation of MC, irregularities, bending and number of layers. Here it was also done an analysis on the obtained results throughout the frequency range and at specific frequencies.

Chapter 5 presented the measurement geometry and setup, followed by the measurements performed on a real scale prototype within the anechoic chamber, with parametrisation of spacing between poles. A statistical analysis with the use of CDF was performed on the measured data at commercial frequencies.

### 6.3 CONTRIBUTIONS TO SCIENCE

The work carried out in this dissertation has contributed to the knowledge with scientific publication in various international conferences, containing most of the work presented throughout the chapters of this dissertation.

At the time of submission of this document, the work presented in this dissertation contributed to the knowledge with five papers, as follows:

- B. A. Tribovane, W. Conniott, N. Leonor, and R. F. Caldeirinha, “**Hybrid Log Shield**”, *Antennas and Propagation Conference (APC 2019)*, 2019;
- B. A. Tribovane, J. Louro, and R. F. Caldeirinha, “**Timber log based barrier for electromagnetic site shielding**”, *2021 Telecoms Conference (ConfTELE)*, 2021;
- B. A. Tribovane and R. F. Caldeirinha, “**A Physical Tuneable Wooden Pole Fence for Radio Transparency Control**”, *International Conference on Electromagnetics in Advanced Applications (ICEAA–IEEE APWC 2021)*, 2021;
- B. A. Tribovane and R. F. Caldeirinha, “**Radio Transparency Control of Road Electromagnetic Barriers for C-V2X Communications**”, *European Conference on Antennas and Propagation 2022 (EuCAP 2022)* (submitted to the conference);
- B. A. Tribovane and R. F. Caldeirinha, “**Radio Transparency Control of Road Electromagnetic Fencing at sub-6 GHz**”, *15.º Congresso do Comité Português da URSI "Sustentabilidade ambiental no uso do espectro radioelétrico"* (URSI 2021).



## 6.4 FUTURE WORK

Regarding future work, it is possible to further study the proposed barrier with broader configurations, with the possibility of implementing new conceptualised ideas to the structure.

Future work will address the characterisation of humidity of prototype with the simulation of different weather conditions. Also, measurements on a wider frequency range of a structure composed by a multi-layer configuration will be considered, either in the anechoic chamber or *in situ*. The possibility of adding energy harvesting capabilities to the barrier through the use of piezoelectric devices for conversion of mechanical energy present in surrounding vibrations, will be explored.

This page is intentionally left blank.

## BIBLIOGRAPHY

---

- [1] P. Dietsch, S. Franke, B. Franke, A. Gamper, and S. Winter, “Methods to determine wood moisture content and their applicability in monitoring concepts,” *Journal of Civil Structural Health Monitoring*, vol. 5, no. 2, pp. 115–127, 2015.
- [2] D. Instruments, “Waveform analysis using the fourier transform,” 1995.
- [3] N. Blaunstein and C. G. Christodoulou, *Radio propagation and adaptive antennas for wireless communication links: terrestrial, atmospheric and ionospheric*. John Wiley & Sons, 2007, vol. 193.
- [4] J. Sophocles, “Orfanidis, ‘electromagnetic waves and antennas,’” 2003.
- [5] G. I. Torgovnikov, “Dielectric properties of wood-based materials,” in *Dielectric Properties of Wood and Wood-Based Materials*. Springer, 1993, pp. 9, 77–79, 178–181.
- [6] A. Dias, L. Godinho, P. Santos, and P. Mendes, “Low visual impact sound reduction wood barriers,” in *Proceedings of WCTE 2014*, 2014.
- [7] P. Mendes, L. Godinho, A. Dias, and P. Santos, “On the use of periodic arrays of timber logs as a sustainable noise mitigation solution,” in *Proceedings of ICSV22*, 2015.
- [8] L. Godinho, P. Santos, P. Mendes, A. Pereira, and M. Martins, “Experimental and numerical analysis of sustainable sonic crystal barriers based on timber logs,” in *Proceedings of EuroRegio 2016*, 2016.
- [9] P. Mendes, L. Godinho, P. Santos, A. Dias, and M. Martins, “Laboratory and full-scale experimental evaluation of the acoustic behaviour of sonic crystal noise barriers,” in *Proceedings of the 22nd International Congress on Acoustics (ICA2016)*, 2016.
- [10] L. Godinho, J. Redondo, and P. Amado-Mendes, “3d analysis of sonic crystal structures with absorbing scatterers,” in *INTER-NOISE and NOISE-CON Congress and Conference Proceedings*, vol. 259, no. 3. Institute of Noise Control Engineering, 2019, pp. 6481–6489.
- [11] J. Huang, Z. Fei, T. Wang, X. Wang, F. Liu, H. Zhou, J. A. Zhang, and G. Wei, “V2x-communication assisted interference minimization for automotive radars,” *China Communications*, vol. 16, no. 10, pp. 100–111, 2019.

- [12] W. Sun, D. Yuan, E. G. Ström, and F. Brännström, “Resource sharing and power allocation for d2d-based safety-critical v2x communications,” in *2015 IEEE International Conference on Communication Workshop (ICCW)*. IEEE, 2015, pp. 2399–2405.
- [13] T.-K. Le, U. Salim, and F. Kaltenberger, “An overview of physical layer design for ultra-reliable low-latency communications in 3gpp releases 15, 16, and 17,” *IEEE Access*, 2020.
- [14] B. A. Tribovane, W. Conniott, N. Leonor, and R. F. Caldeirinha, “Hybrid Log Shield,” *Antennas and Propagation Conference (APC 2019)*, 2019.
- [15] B. A. Tribovane, J. Louro, and R. F. Caldeirinha, “Timber log based barrier for electromagnetic site shielding,” *2021 Telecoms Conference (ConfTELE)*, 2021.
- [16] W. Conniott, J. R. Reis, N. Leonor, and R. F. S. Caldeirinha, “Shielding effectiveness of log barriers for radio exclusion zones,” in *The Loughborough Antennas Propagation Conference (LAPC 2018)*, Nov 2018, pp. 1–5.
- [17] M. Amirkhanyan and F. Bryukhan, “Shielding effect of reinforced concrete fences in electromagnetic fields of industrial frequency,” in *MATEC Web of Conferences*, vol. 251. EDP Sciences, 2018, p. 06006.
- [18] K. W. Jin, T. J. Huat, and K. C. H. Ernest, “High frequency (hf) suppression with a shielded fence,” in *2006 17th International Zurich Symposium on Electromagnetic Compatibility*. IEEE, pp. 638–641.
- [19] W. T. Simpson, “Specific gravity, moisture content, and density relationship for wood,” (*General technical report FPL, GTR-76*): 13 p.: ill.; 28 cm., vol. 76, p. 1, 1993.
- [20] V. Komarov, S. Wang, and J. Tang, “Permittivity and measurements,” 2005.
- [21] J. Krupka, “Frequency domain complex permittivity measurements at microwave frequencies,” *Measurement Science and Technology*, vol. 17, no. 6, p. R55, 2006.
- [22] A. F. Molisch, *Wireless communications*. John Wiley & Sons, 2012, vol. 34.
- [23] S. R. Saunders and A. Aragón-Zavala, *Antennas and propagation for wireless communication systems*. John Wiley & Sons, 2007.
- [24] B. B. Baker and E. T. Copson, *The mathematical theory of Huygens’ principle*. American Mathematical Soc., 2003, vol. 329.
- [25] D. B. Melrose and R. C. McPhedran, *Electromagnetic processes in dispersive media*. Cambridge University Press, 2005.

- [26] Z. Xia, C. Wang, J. Jin, S. Du, H. Lin, and H. Yang, “Novel am/fm/ask/fsk/p-sk/qam signal generator based on a digitally programmable cdta,” *Circuits, Systems, and Signal Processing*, vol. 34, no. 5, pp. 1635–1653, 2015.
- [27] D. Brandwood, *Fourier transforms in radar and signal processing*. Artech House, 2012.
- [28] J. A. Shaw, “Radiometry and the friis transmission equation,” *American journal of physics*, vol. 81, no. 1, pp. 33–37, 2013.
- [29] H. T. Friis, “A note on a simple transmission formula,” *Proceedings of the IRE*, vol. 34, no. 5, pp. 254–256, 1946.
- [30] J. C. Whitaker, *The electronics handbook*. Crc Press, 2018.
- [31] R. Bansal, “The far-field: How far is far enough?” *Applied Microwave & Wireless*, vol. 11, no. 11, pp. 59–60, 1999.
- [32] P. J. Pupalaikis, *S-parameters for Signal Integrity*. Cambridge University Press, 2020.
- [33] D. Micheli, A. Delfini, F. Santoni, F. Volpini, and M. Marchetti, “Measurement of electromagnetic field attenuation by building walls in the mobile phone and satellite navigation frequency bands,” *IEEE antennas and wireless propagation letters*, vol. 14, pp. 698–702, 2014.
- [34] D. Micheli, P. Gianola, G. Bertin, A. Delfini, R. Pastore, M. Marchetti, and R. Diana, “Electromagnetic shielding of building walls: From roman times to the present age.” *IEEE Antennas and Propagation Magazine*, vol. 58, no. 5, pp. 20–31, 2016.
- [35] M. J. Gaspar, J. L. Louzada, A. Aguiar, and M. H. Almeida, “Genetic correlations between wood quality traits of *Pinus pinaster* Ait.” *Annals of Forest Science*, vol. 65, no. 7, pp. 2–3, 2008.
- [36] S. Vogel, “Twist-to-bend ratios of woody structures,” *Journal of Experimental Botany*, vol. 46, no. 8, 1995.
- [37] *R&S®ZVRx, R&S®ZVCx, R&S®ZVM, R&S®ZVK Operating Manual*, 2005.

This page is intentionally left blank.

## APPENDICES





## SCRIPT FOR AUTOMATIC BARRIER MODELLING

The presented in Appendix A.1 is the main code to generate the model in CST along with the associated functions presented in Appendices A.2, A.3 and A.4 to introduce the trunks' material, generate poles and surface roughness, and apply bending to the trunks.

## A.1 MAIN CODE TO GENERATE THE MODEL IN CST

```

1 %%
2 % Script developed within the scope of the project "Hybrid Log Shield
   ",
3 % 2018-2021
4 % Author: Bruno Tribovane
5 %%
6 clearvars,close all;
7
8 %% Define variables
9 polarisation=90; % [deg], port polarisation
10
11 height=2270; % [mm], trunk height
12
13 inner_layers=6; %number of layers within trunk for MC
14 min_mc=10; % min MC
15 max_mc=30; % max MC
16 mc_steps=round(linspace(min_mc,max_mc,inner_layers)); %linear
   variation of moisture content
17 % mc_steps=wrev(round(logspace(log10(10),log10(60),inner_layers))); %
   exponential variation
18
19 radius_s=60; % trunks radius
20
21 dx1=180; % [mm], spacing between centre of trunks on x-axis
22 dy1=180; % [mm], spacing between centre of trunks on y-axis
23 dx2=0; % offset from first layer on x-axis [mm]
24 dx3=0; % offset from first layer on x-axis [mm]
25
26 n_S_trunks=1; % number of trunks in a layer
27 n_S_layers=1; % number of trunks' arrays/layers
28
29 %% Boundary conditions

```

```

30 xboundary=1; % boundary conditions on x-axis, 1 -> periodic, 2-> open
    expanded
31
32 %% Irregularity definitions
33 add_irr = 0; % 1-> add irregularities, 0 -> do not add
34
35 n_irr_layers=5; % number of cylinder layers [divisions]
36
37 std_dev_cyl=0; %std for number of cylinders
38 av_cyl=10; %mean for number of cylinders
39
40 std_dev_r=0.5; %std for cylinder radius [mm]
41 av_r=1; %mean for cylinder radius [mm]
42
43 std_dev_z=6; %std for min/max cylinder height [mm]
44 av_z=0; %mean for min/max cylinder height [mm]
45
46 std_dev_o=pi; %std for theta (cylinder placement around trunks)[rads]
47 av_o=0; %mean for theta (cylinder placement around trunks)[rads]
48
49 %% Bending definitions
50 add_bend = 0; % 1-> add bending, 0 -> do not add
51
52 std_dev_bend_loc=height/6; %std for bend location [mm]
53 av_bend_loc=height/3; %mean for bend location [mm]
54
55 std_dev_bend_factor=2; %std for bend factor (cylindrical bend)
56 av_bend_factor=5; %mean for bend factor (cylindrical bend)
57
58 std_dev_bend_dir=180; %std for bend direction [deg]
59 av_bend_dir=0; %mean for bend direction [deg]
60
61 %% Access CST
62 cst = actxserver('CSTStudio.application');
63 mws = cst.invoke('Active3D');
64
65 %% Add Variables to CST
66 invoke(mws, 'StoreParameter', 'radius_s', radius_s);
67 invoke(mws, 'StoreParameter', 'dx1', dx1);
68 invoke(mws, 'StoreParameter', 'dy1', dy1);
69 invoke(mws, 'StoreParameter', 'dx2', dx2);
70 invoke(mws, 'StoreParameter', 'dy2', 'dy1');
71 invoke(mws, 'StoreParameter', 'dx3', dx3);
72 invoke(mws, 'StoreParameter', 'height', height);
73 invoke(mws, 'StoreParameter', 'polarisation', polarisation);
74
75 xmin=sprintf('-radius_s');
76 invoke(mws, 'StoreParameter', 'Xmin', xmin);
77
78 xmax=sprintf('dx1-radius_s+dx1*(%i-1)', n_S_trunks);

```

```

79 invoke(mws, 'StoreParameter', 'Xmax', xmax);
80 if n_S_layers==1
81     ymax=sprintf('radius_s');
82 end
83 if n_S_layers==2
84     ymax=sprintf('radius_s+dy1');
85 end
86 if n_S_layers==3
87     ymax=sprintf('radius_s+dy1+dy2');
88 end
89 ymin='-radius_s';
90
91 invoke(mws, 'StoreParameter', 'Ymax', ymax);
92 invoke(mws, 'StoreParameter', 'Ymin', ymin);
93
94 %% Create Materials
95 create_material(inner_layers, mc_steps);
96
97 %% Create Trunks + Irregularities
98 if n_S_layers ~= 0 && n_S_trunks ~= 0
99     create_trunks_S(add_irr, inner_layers, n_S_trunks, n_S_layers, height
100         , n_irrlayers, std_dev_cyl, std_dev_r, std_dev_z, std_dev_o, ...
101         av_cyl, av_r, av_z, av_o);
102 end
103 %% Create Base
104 mws.invoke('AddToHistory', 'Base', [...
105     sprintf('With Brick\n') ...
106     sprintf(' .Reset\n') ...
107     sprintf(' .Name "Base"\n') ...
108     sprintf(' .Component "component_main"\n') ...
109     sprintf(' .Material "pinus_pinaster_1"\n') ...
110     sprintf(' .Xrange "Xmin", "Xmax"\n') ...
111     sprintf(' .Yrange "Ymin", "Ymax"\n') ...
112     sprintf(' .Zrange "0", "-20"\n') ...
113     sprintf(' .Create\n') ...
114     sprintf('End With')]);
115 %% Create Ports
116 aux=string([-20; ' 20']);
117 orientation=string(['ymin'; 'ymax']);
118
119 for port=1:2
120     mws.invoke('AddToHistory', sprintf('Port%i', port), [...
121         sprintf('With Port\n') ...
122         sprintf(' .Reset\n') ...
123         sprintf(' .PortNumber "%i"\n', port) ...
124         sprintf(' .Label ""\n') ...
125         sprintf(' .Folder ""\n') ...
126         sprintf(' .NumberOfModes "1"\n') ...
127         sprintf(' .AdjustPolarization "True"\n') ...

```

```

128     sprintf(' .PolarizationAngle "polarisation"\n') ...
129     sprintf(' .ReferencePlaneDistance "0"\n') ...
130     sprintf(' .TextSize "50"\n') ...
131     sprintf(' .TextMaxLimit "1"\n') ...
132     sprintf(' .Coordinates "Free"\n') ...
133     sprintf(' .Orientation "%s"\n',orientation(port)) ...
134     sprintf(' .PortOnBound "True"\n') ...
135     sprintf(' .ClipPickedPortToBound "False"\n') ...
136     sprintf(' .Xrange "xmin", "xmax"\n') ...
137     sprintf(' .Yrange "ymin+%s", "ymax+%s"\n',aux(port),aux(port
)) ...
138     sprintf(' .Zrange "%f", "height"\n',(-20)) ...
139     sprintf(' .XrangeAdd "0.0", "0.0"\n') ...
140     sprintf(' .YrangeAdd "0.0", "0.0"\n') ...
141     sprintf(' .ZrangeAdd "0.0", "0.0"\n') ...
142     sprintf(' .SingleEnded "False"\n') ...
143     sprintf(' .Shield "PEC"\n') ...
144     sprintf(' .WaveguideMonitor "False"\n') ...
145     sprintf(' .Create\n') ...
146     sprintf('End With']);
147 end
148 %% Bend Trunks
149 if add_bend == 1
150 bend_trunks(inner_layers,n_S_trunks,n_S_layers,...
151     std_dev_bend_loc,av_bend_loc,std_dev_bend_factor,av_bend_factor
,...
152     std_dev_bend_dir,av_bend_dir)
153 end
154
155 %% Structure boundaries
156 xbound=["periodic","expanded open"]; % boundary conditions on x-axis
157 mws.invoke('AddToHistory', sprintf('define boundaries'),[...
158     sprintf('With Boundary\n') ...
159     sprintf(' .Xmin "%s"\n',xbound(xboundary)) ...
160     sprintf(' .Xmax "%s"\n',xbound(xboundary)) ...
161     sprintf(' .Ymin "expanded open"\n') ...
162     sprintf(' .Ymax "expanded open"\n') ...
163     sprintf(' .Zmin "expanded open"\n') ...
164     sprintf(' .Zmax "expanded open"\n') ...
165     sprintf(' .Xsymmetry "none"\n') ...
166     sprintf(' .Ysymmetry "none"\n') ...
167     sprintf(' .Zsymmetry "none"\n') ...
168     sprintf(' .ApplyInAllDirections "False"\n') ...
169     sprintf(' .XPeriodicShift "0.0"\n') ...
170     sprintf(' .YPeriodicShift "0.0"\n') ...
171     sprintf(' .ZPeriodicShift "0.0"\n') ...
172     sprintf(' .PeriodicUseConstantAngles "False"\n') ...
173     sprintf('End With')]);
174
175 %% define Mesh settings

```

```

176 mws.invoke('AddToHistory', sprintf('define mesh'),[...
177     sprintf('With Mesh\n') ...
178     sprintf(' .MeshType "PBA"\n') ...
179     sprintf(' .SetCreator "High Frequency"\n') ...
180     sprintf('End With\n') ...
181     sprintf('With MeshSettings\n') ...
182     sprintf(' .SetMeshType "Hex"\n') ...
183     sprintf(' .Set "Version", 1%%\n') ...
184     sprintf(' 'MAX CELL - WAVELENGTH REFINEMENT\n') ...
185     sprintf(' .Set "StepsPerWaveNear", "8"\n') ...
186     sprintf(' .Set "StepsPerWaveFar", "8"\n') ...
187     sprintf(' .Set "WavelengthRefinementSameAsNear", "1"\n') ...
188     sprintf(' 'MAX CELL - GEOMETRY REFINEMENT\n') ...
189     sprintf(' .Set "StepsPerBoxNear", "20"\n') ...
190     sprintf(' .Set "StepsPerBoxFar", "1"\n') ...
191     sprintf(' .Set "MaxStepNear", "0"\n') ...
192     sprintf(' .Set "MaxStepFar", "0"\n') ...
193     sprintf(' .Set "ModelBoxDescrNear", "maxedge\n') ...
194     sprintf(' .Set "ModelBoxDescrFar", "maxedge\n') ...
195     sprintf(' .Set "UseMaxStepAbsolute", "0"\n') ...
196     sprintf(' .Set "GeometryRefinementSameAsNear", "0"\n') ...
197     sprintf(' 'MIN CELL \n') ...
198     sprintf(' .Set "UseRatioLimitGeometry", "1"\n') ...
199     sprintf(' .Set "RatioLimitGeometry", "20"\n') ...
200     sprintf(' .Set "MinStepGeometryX", "0"\n') ...
201     sprintf(' .Set "MinStepGeometryY", "0"\n') ...
202     sprintf(' .Set "MinStepGeometryZ", "0"\n') ...
203     sprintf(' .Set "UseSameMinStepGeometryXYZ", "1"\n') ...
204     sprintf('End With\n') ...
205     sprintf('With MeshSettings\n') ...
206     sprintf(' .Set "PlaneMergeVersion", "2"\n') ...
207     sprintf('End With\n') ...
208     sprintf('With MeshSettings\n') ...
209     sprintf(' .SetMeshType "Hex"\n') ...
210     sprintf(' .Set "FaceRefinementOn", "0"\n') ...
211     sprintf(' .Set "FaceRefinementPolicy", "2"\n') ...
212     sprintf(' \n') ...
213     sprintf(' .Set "FaceRefinementRatio", "2"\n') ...
214     sprintf(' .Set "FaceRefinementStep", "0"\n') ...
215     sprintf(' .Set "FaceRefinementNSteps", "2"\n') ...
216     sprintf(' .Set "EllipseRefinementOn", "0"\n') ...
217     sprintf(' .Set "EllipseRefinementPolicy", "2"\n') ...
218     sprintf(' .Set "EllipseRefinementRatio", "2"\n') ...
219     sprintf(' .Set "EllipseRefinementStep", "0"\n') ...
220     sprintf(' .Set "EllipseRefinementNSteps", "2"\n') ...
221     sprintf(' .Set "FaceRefinementBufferLines", "3"\n') ...
222     sprintf(' .Set "EdgeRefinementOn", "1"\n') ...
223     sprintf(' .Set "EdgeRefinementPolicy", "1"\n') ...
224     sprintf(' .Set "EdgeRefinementRatio", "2"\n') ...
225     sprintf(' .Set "EdgeRefinementStep", "0"\n') ...

```

```

226     sprintf(' .Set "EdgeRefinementBufferLines", "3"\n') ...
227     sprintf(' .Set "RefineEdgeMaterialGlobal", "0"\n') ...
228     sprintf(' .Set "RefineAxialEdgeGlobal", "0"\n') ...
229     sprintf(' .Set "BufferLinesNear", "3"\n') ...
230     sprintf(' .Set "UseDielectrics", "1"\n') ...
231     sprintf(' .Set "EquilibrateOn", "0"\n') ...
232     sprintf(' .Set "Equilibrate", "1.5"\n') ...
233     sprintf(' .Set "IgnoreThinPanelMaterial", "0"\n') ...
234     sprintf('End With\n') ...
235     sprintf('With MeshSettings\n') ...
236     sprintf(' .SetMeshType "Hex"\n') ...
237     sprintf(' .Set "SnapToAxialEdges", "1"\n') ...
238     sprintf(' .Set "SnapToPlanes", "1"\n') ...
239     sprintf(' .Set "SnapToSpheres", "1"\n') ...
240     sprintf(' .Set "SnapToEllipses", "1"\n') ...
241     sprintf(' .Set "SnapToCylinders", "1"\n') ...
242     sprintf(' .Set "SnapToCylinderCenters", "1"\n') ...
243     sprintf(' .Set "SnapToEllipseCenters", "1"\n') ...
244     sprintf('End With\n') ...
245     sprintf('With Discretizer\n') ...
246     sprintf(' .ConnectivityCheck "False"\n') ...
247     sprintf(' .UsePecEdgeModel "True"\n') ...
248     sprintf(' .GapDetection "False"\n') ...
249     sprintf(' .FPBAGapTolerance "1e-3"\n') ...
250     sprintf(' .PointAccEnhancement "0"\n') ...
251     sprintf(' .TSTVersion "0"\n') ...
252     sprintf(' .PBAVersion "2019070519"\n') ...
253     sprintf('End With')]');
254
255 release(mws);
256 release(cst);

```

Listing A.1: Main code for model construction.

## A.2 MATERIAL GENERATION

```

1 %%
2 % Script developed within the scope of the project "Hybrid Log Shield
  ",
3 % 2018-2021
4 % Author: Bruno Tribovane
5 %%
6 function [] = create_material(inner_layers, mc_steps)
7 %% Moisture content definition
8     %table
9     %Values taken from "Dielectric properties of wood-based materials"
10 MC=[10 20 30 60];
11 Er_10_9=[2.5 3.4 4.7 6.9];
12 Er_2p4_9=[2.3 2.9 3.8 6.5];
13 Er_5p8_9=[2.15 2.6 3.8 5.9];

```

```

14
15 tg_10_9=[0.1 0.16 0.22 0.21];
16 tg_2p4_9=[0.11 0.18 0.22 0.20];
17 tg_5p8_9=[0.1 0.21 0.26 0.25];
18
19 interp_Er_10_9=interp1(MC,Er_10_9,10:1:60);
20 interp_Er_2p4_9=interp1(MC,Er_2p4_9,10:1:60);
21 interp_Er_5p8_9=interp1(MC,Er_5p8_9,10:1:60);
22
23 interp_tg_10_9=interp1(MC,tg_10_9,10:1:60);
24 interp_tg_2p4_9=interp1(MC,tg_2p4_9,10:1:60);
25 interp_tg_5p8_9=interp1(MC,tg_5p8_9,10:1:60);
26
27 %% Material creation
28 cst = actxserver('CSTStudio.application');
29 mws = cst.invoke('Active3D');
30 colour=[0.5 0.4];
31
32 for i=1:inner_layers
33
34     er1=interp_Er_10_9(mc_steps(i)-9);
35     er2=interp_Er_2p4_9(mc_steps(i)-9);
36     er3=interp_Er_5p8_9(mc_steps(i)-9);
37     tg1=interp_tg_10_9(mc_steps(i)-9);
38     tg2=interp_tg_2p4_9(mc_steps(i)-9);
39     tg3=interp_tg_5p8_9(mc_steps(i)-9);
40     mws.invoke('AddToHistory', sprintf('material %i',i),[...
41         sprintf('With Material\n') ...
42         sprintf(' .Reset\n') ...
43         sprintf(' .Name "pinus_pinaster_%i"\n',i) ...
44         sprintf(' .Folder ""\n') ...
45         sprintf(' .Rho "500"\n') ...
46         sprintf(' .ThermalType "Normal"\n') ...
47         sprintf(' .ThermalConductivity "0"\n') ...
48         sprintf(' .HeatCapacity "0"\n') ...
49         sprintf(' .DynamicViscosity "0"\n') ...
50         sprintf(' .Emissivity "0"\n') ...
51         sprintf(' .MetabolicRate "0.0"\n') ...
52         sprintf(' .VoxelConvection "0.0"\n') ...
53         sprintf(' .BloodFlow "0"\n') ...
54         sprintf(' .MechanicsType "Unused"\n') ...
55         sprintf(' .FrqType "all"\n') ...
56         sprintf(' .Type "Normal"\n') ...
57         sprintf(' .MaterialUnit "Frequency", "GHz"\n') ...
58         sprintf(' .MaterialUnit "Geometry", "mm"\n') ...
59         sprintf(' .MaterialUnit "Time", "ns"\n') ...
60         sprintf(' .MaterialUnit "Temperature", "Kelvin"\n') ...
61         sprintf(' .Epsilon "3.2"\n') ...
62         sprintf(' .Mu "1"\n') ...
63         sprintf(' .Sigma "0.0"\n') ...

```

```

64     sprintf(' .TanD "0.0"\n') ...
65     sprintf(' .TanDFreq "9.4"\n') ...
66     sprintf(' .TanDGiven "True"\n') ...
67     sprintf(' .TanDModel "ConstTanD"\n') ...
68     sprintf(' .EnableUserConstTanDModelOrderEps "False"\n') ...
69     sprintf(' .ConstTanDModelOrderEps "1"\n') ...
70     sprintf(' .SetElParametricConductivity "False"\n') ...
71     sprintf(' .ReferenceCoordSystem "Global"\n') ...
72     sprintf(' .CoordSystemType "Cartesian"\n') ...
73     sprintf(' .SigmaM "0"\n') ...
74     sprintf(' .TanDM "0.0"\n') ...
75     sprintf(' .TanDMFreq "0.0"\n') ...
76     sprintf(' .TanDMGiven "False"\n') ...
77     sprintf(' .TanDMModel "ConstTanD"\n') ...
78     sprintf(' .EnableUserConstTanDModelOrderMu "False"\n') ...
79     sprintf(' .ConstTanDModelOrderMu "1"\n') ...
80     sprintf(' .SetMagParametricConductivity "False"\n') ...
81     sprintf(' .DispModelEps "None"\n') ...
82     sprintf(' .DispModelMu "None"\n') ...
83     sprintf(' .DispersiveFittingSchemeEps "Nth Order"\n') ...
84     sprintf(' .MaximalOrderNthModelFitEps "10"\n') ...
85     sprintf(' .ErrorLimitNthModelFitEps "0.02"\n') ...
86     sprintf(' .UseOnlyDataInSimFreqRangeNthModelEps "False"\n')
...
87     sprintf(' .DispersiveFittingSchemeMu "Nth Order"\n') ...
88     sprintf(' .MaximalOrderNthModelFitMu "10"\n') ...
89     sprintf(' .ErrorLimitNthModelFitMu "0.1"\n') ...
90     sprintf(' .UseOnlyDataInSimFreqRangeNthModelMu "False"\n')
...
91     sprintf(' .DispersiveFittingFormatEps "Real_Tand"\n') ...
92     sprintf(' .AddDispersionFittingValueEps "1", "%f", "%f",
"1"\n',er1,tg1) ...
93     sprintf(' .AddDispersionFittingValueEps "2.4", "%f", "%f",
"1"\n',er2,tg2) ...
94     sprintf(' .AddDispersionFittingValueEps "5.8", "%f", "%f",
"1"\n',er3,tg3) ...
95     sprintf(' .UseGeneralDispersionEps "True"\n') ...
96     sprintf(' .UseGeneralDispersionMu "False"\n') ...
97     sprintf(' .NonlinearMeasurementError "1e-1"\n') ...
98     sprintf(' .NLAnisotropy "False"\n') ...
99     sprintf(' .NLStackingFactor "1"\n') ...
100    sprintf(' .NLADirectionX "1"\n') ...
101    sprintf(' .NLADirectionY "0"\n') ...
102    sprintf(' .NLADirectionZ "0"\n') ...
103    sprintf(' .Colour "1", "%f", "0.2500"\n',colour(rem(i,2)+1))
...
104    sprintf(' .Wireframe "False"\n') ...
105    sprintf(' .Reflection "False"\n') ...
106    sprintf(' .Allowoutline "True"\n') ...
107    sprintf(' .Transparentoutline "False"\n') ...

```



```

108     sprintf(' .Transparency "0"\n') ...
109     sprintf(' .Create\n') ...
110     sprintf('End With')]);
111 end

```

Listing A.2: Function to generate material.

### A.3 TRUNKS AND IRREGULARITIES DEFINITION

```

1 %%
2 % Script developed within the scope of the project "Hybrid Log Shield
  ",
3 % 2018-2021
4 % Author: Bruno Tribovane
5 %%
6 function [] = create_trunks_S(add_irr,inner_layers,n_S_trunks,
  n_S_layers,height,n_irrlayers,std_dev_cyl,std_dev_r,std_dev_z,
  std_dev_o,...
7     av_cyl,av_r,av_z,av_o)
8 %% Define random parameters (irregularities)
9 step=height/n_irrlayers;
10 rnd_cyl = round(std_dev_cyl.*(2*abs(rand(1,n_irrlayers+1))-1) +
  av_cyl); %random value using uniform distribution
11 rnd_r = std_dev_r.*(2*rand(1,n_irrlayers*(std_dev_cyl+av_cyl+1))-1) +
  av_r; %random value using uniform distribution
12 rnd_z = std_dev_z.*(2*rand(1,n_irrlayers*(std_dev_cyl+av_cyl+1))-1) +
  av_z; %random value using uniform distribution
13 rnd_o = std_dev_o.*(2*rand(1,n_irrlayers*(std_dev_cyl+av_cyl+1))-1) +
  av_o; %random value using uniform distribution
14
15 %% Create Reference/Main Trunk
16 cst = actxserver('CSTStudio.application');
17 mws = cst.invoke('Active3D');
18
19 for j=1:inner_layers
20     mws.invoke('AddToHistory', sprintf('small_trunk%i',j),[...
21         sprintf('With Cylinder\n') ...
22         sprintf(' .Reset\n') ...
23         sprintf(' .Name "small_trunk%i"\n',j) ...
24         sprintf(' .Component "component_main/componentSL1/
  componentS1"\n') ...
25         sprintf(' .Material "pinus_pinaster_%i"\n',j) ...
26         sprintf(' .OuterRadius "(radius_s%i)/%i"\n',j,inner_layers)
  ...
27         sprintf(' .InnerRadius "(radius_s%i)/%i"\n',j-1,
  inner_layers) ...
28         sprintf(' .Axis "z"\n') ...
29         sprintf(' .Zrange "%0.6f", "height"\n', 0) ...
30         sprintf(' .Xcenter "0"\n') ...
31         sprintf(' .Ycenter "0"\n') ...

```

```

32     sprintf(' .Segments "0"\n') ...
33     sprintf(' .Create\n') ...
34     sprintf('End With']]);
35 end
36
37 % for k=2:inner_layers
38 %     mws.invoke('AddToHistory', sprintf('Add trunk inner layer %i',k
-1),sprintf('Solid.Add "componentS1:small_trunk1", "componentS1:
small_trunk%i"\n',k));
39 % end
40 %% Create irregularities on Main Trunk
41 if add_irr == 1
42     count=0;
43     for n=1:n_irrlayers
44
45         for j=1:rnd_cyl(n)
46             count=count+1;
47             name=['cylinder' num2str(count)];%%
48             minZ=step*(n-1);
49             maxZ=minZ+step;
50
51             theta=j*2*pi/rnd_cyl(n)+rnd_o(count);
52             %     rho=r-rnd_r(count)/max(rnd_r);
53             %     [x,y]=pol2cart(theta,rho);
54
55             mws.invoke('AddToHistory', name,[...
56                 sprintf('With Cylinder\n') ...
57                 sprintf(' .Reset\n') ...
58                 sprintf(' .Name "%s"\n',name) ...
59                 sprintf(' .Component "component_main/componentSL1/
componentS1"\n') ...
60                 sprintf(' .Material "PEC"\n') ...
61                 sprintf(' .OuterRadius "%f"\n',abs(rnd_r(count)))
...
62                 sprintf(' .InnerRadius "0"\n') ...
63                 sprintf(' .Axis "z"\n') ...
64                 sprintf(' .Zrange "%0.6f", "%0.6f"\n', minZ-rnd_z(
count), maxZ+rnd_z(count)) ...
65                 sprintf(' .Xcenter "radius_s*%0.6f"\n', cos(theta))
...
66                 sprintf(' .Ycenter "radius_s*%0.6f"\n', sin(theta))
...
67                 sprintf(' .Segments "0"\n') ...
68                 sprintf(' .Create\n') ...
69                 sprintf('End With']]);
70         end
71     end
72
73     %%Use for low amount of layers for boolean subtract for faster
processing

```

```

74     for i=1:count
75         mws.invoke('AddToHistory', sprintf('Cut trunk %i',i),sprintf(
'Solid.Subtract "component_main/componentSL1/componentS1:
small_trunk%i", "component_main/componentSL1/componentS1:cylinder
%i"\n',inner_layers,i));
76     end
77 end
78 %% Copy/Move Trunks
79 for trunk=1:n_S_trunks-1
80     mws.invoke('AddToHistory', sprintf('new component trunk%i',trunk
+1), sprintf('Component.New "component_main/componentSL1/
componentS%i"',trunk+1));
81     mws.invoke('AddToHistory', sprintf('Copy/MoveS%i',trunk+1),[...
82         sprintf('With Transform\n') ...
83         sprintf(' .Reset\n') ...
84         sprintf(' .Name "component_main/componentSL1/componentS1"\n'
) ...
85         sprintf(' .Vector "dx1%i", "0", "0"\n',trunk) ...
86         sprintf(' .UsePickedPoints "False"\n') ...
87         sprintf(' .InvertPickedPoints "False"\n') ...
88         sprintf(' .MultipleObjects "True"\n') ...
89         sprintf(' .GroupObjects "False"\n') ...
90         sprintf(' .Repetitions "1"\n') ...
91         sprintf(' .MultipleSelection "True"\n') ...
92         sprintf(' .Destination "component_main/componentSL1/
componentS%i"\n',trunk+1) ...
93         sprintf(' .Material ""\n') ...
94         sprintf(' .Transform "Shape", "Translate"\n') ...
95         sprintf('End With')]);
96 end
97 %% create layers
98
99 if n_S_layers>1
100     for layer=1:n_S_layers-1
101         mws.invoke('AddToHistory', sprintf('new componentSL%i',layer
+1), sprintf('Component.New "component_main/componentSL%i"',layer
+1));
102         mws.invoke('AddToHistory', sprintf('Copy/MoveS%i',layer+1)
,[...
103             sprintf('With Transform\n') ...
104             sprintf(' .Reset\n') ...
105             sprintf(' .Name "component_main/componentSL%i"\n',layer)
...
106             sprintf(' .Vector "0", "dy%i", "0"\n',layer) ...
107             sprintf(' .UsePickedPoints "False"\n') ...
108             sprintf(' .InvertPickedPoints "False"\n') ...
109             sprintf(' .MultipleObjects "True"\n') ...
110             sprintf(' .GroupObjects "False"\n') ...
111             sprintf(' .Repetitions "1"\n') ...
112             sprintf(' .MultipleSelection "False"\n') ...

```

```

113         sprintf(' .Destination "component_main/componentSL%i"\n'
,layer+1) ...
114         sprintf(' .Material ""\n') ...
115         sprintf(' .Transform "Shape", "Translate"\n') ...
116         sprintf('End With'));
117     end
118     for layer=1:n_S_layers-1
119         mws.invoke('AddToHistory', sprintf('MoveS%i',layer+1),[...
120             sprintf('With Transform\n') ...
121             sprintf(' .Reset\n') ...
122             sprintf(' .Name "component_main/componentSL%i"\n',layer
+1) ...
123             sprintf(' .Vector "dx%i", "0", "0"\n',layer+1) ...
124             sprintf(' .UsePickedPoints "False"\n') ...
125             sprintf(' .InvertPickedPoints "False"\n') ...
126             sprintf(' .MultipleObjects "False"\n') ...
127             sprintf(' .GroupObjects "False"\n') ...
128             sprintf(' .Repetitions "1"\n') ...
129             sprintf(' .MultipleSelection "False"\n') ...
130             sprintf(' .Transform "Shape", "Translate"\n') ...
131             sprintf('End With')]);
132     end
133     %% create lateral trunk for shifting purposes
134
135     % fake-remove trunks
136     for i=0:1
137         mws.invoke('AddToHistory', sprintf('new component trunk%i',
n_S_trunks+1+i), sprintf('Component.New "component_main/
componentSL%i/componentS%i"',i+2,n_S_trunks+1));
138
139         if (i == 0 && n_S_layers == 2) || (n_S_layers == 3)
140             mws.invoke('AddToHistory', sprintf('Left Copy/MoveS%i',i
+1),[...
141                 sprintf('With Transform\n') ...
142                 sprintf(' .Reset\n') ...
143                 sprintf(' .Name "component_main/componentSL%i/
componentS1"\n',i+2) ...
144                 sprintf(' .Vector "%i*dx1", "0", "0"\n',-1) ...
145                 sprintf(' .UsePickedPoints "False"\n') ...
146                 sprintf(' .InvertPickedPoints "False"\n') ...
147                 sprintf(' .MultipleObjects "True"\n') ...
148                 sprintf(' .GroupObjects "False"\n') ...
149                 sprintf(' .Repetitions "1"\n') ...
150                 sprintf(' .MultipleSelection "False"\n') ...
151                 sprintf(' .Destination "component_main/componentSL%i
/componentS%i"\n',i+2,n_S_trunks+1) ...
152                 sprintf(' .Material ""\n') ...
153                 sprintf(' .Transform "Shape", "Translate"\n') ...
154                 sprintf('End With')]);
155     end

```

```

156     mws.invoke('AddToHistory', sprintf('brick_%i',i),[...
157         sprintf('With Brick\n') ...
158         sprintf(' .Reset\n') ...
159         sprintf(' .Name "brick_%i"\n',i) ...
160         sprintf(' .Component "component_main"\n') ...
161         sprintf(' .Material "pinus_pinaster_1"\n') ...
162         sprintf(' .Xrange "-Xmax*4+(Xmax*5)*%i", "Xmin+(-Xmin+
Xmax*5)*%i"\n',i,i) ...
163         sprintf(' .Yrange "0", "Ymax"\n') ...
164         sprintf(' .Zrange "0", "height"\n') ...
165         sprintf(' .Create\n') ...
166         sprintf('End With')]);
167     end
168     for i=1:inner_layers
169         if n_S_layers == 2
170             mws.invoke('AddToHistory', sprintf('SL2 Insert brick
0 on left inner_layer %i',i),sprintf('Solid.Insert "
component_main/componentSL2/componentS%i:small_trunk%i", "
component_main:brick_0"\n',n_S_trunks+1,i));
171             mws.invoke('AddToHistory', sprintf('SL2 Insert brick
1 on right inner_layer %i',i),sprintf('Solid.Insert "
component_main/componentSL2/components%i:small_trunk%i", "
component_main:brick_1"\n',n_S_trunks,i));
172         end
173         if n_S_layers == 3
174             mws.invoke('AddToHistory', sprintf('SL2 Insert brick
0 on left inner_layer %i',i),sprintf('Solid.Insert "
component_main/componentSL2/componentS%i:small_trunk%i", "
component_main:brick_0"\n',n_S_trunks+1,i));
175             mws.invoke('AddToHistory', sprintf('SL2 Insert brick
1 on right inner_layer %i',i),sprintf('Solid.Insert "
component_main/componentSL2/componentS%i:small_trunk%i", "
component_main:brick_1"\n',n_S_trunks,i));
176             mws.invoke('AddToHistory', sprintf('SL3 Insert brick
0 on left inner_layer %i',i),sprintf('Solid.Insert "
component_main/componentSL3/componentS%i:small_trunk%i", "
component_main:brick_0"\n',n_S_trunks+1,i));
177             mws.invoke('AddToHistory', sprintf('SL3 Insert brick
1 on right inner_layer %i',i),sprintf('Solid.Insert "
component_main/componentSL3/componentS%i:small_trunk%i", "
component_main:brick_1"\n',n_S_trunks,i));
178         end
179     end
180
181
182     mws.invoke('AddToHistory', sprintf('delete brick 0'),sprintf('
Solid.Delete "component_main:brick_0"\n'));
183     mws.invoke('AddToHistory', sprintf('delete brick 1'),sprintf('
Solid.Delete "component_main:brick_1"\n'));
184 end

```

```

185
186 end

```

Listing A.3: Function to generate trunks and irregularities.

#### A.4 TRUNKS' BENDING

```

1 %%
2 % Script developed within the scope of the project "Hybrid Log Shield
  ",
3 % 2018-2021
4 % Author: Bruno Tribovane
5 %%
6 function [] = bend_trunks(inner_layers,n_S_trunks,n_S_layers,...
7     std_dev_bend_loc,av_bend_loc,std_dev_bend_factor,av_bend_factor
8     ,...
9     std_dev_bend_dir,av_bend_dir)
10 %% Local vars
11 count=1;
12 shift_y='0';
13 shift_x='dx1';
14 %% Define random parameters
15 rnd_bend_locS = std_dev_bend_loc.*(2*rand(1,n_S_trunks*n_S_layers)-1)
16     + av_bend_loc; %random values using uniform distribution
17 rnd_bend_factorS = std_dev_bend_factor.*(2*rand(1,n_S_trunks*
18     n_S_layers)-1) + av_bend_factor; %random values using uniform
19     distribution
20 rnd_bend_dirS = std_dev_bend_dir.*(2*rand(1,n_S_trunks*n_S_layers)-1)
21     + av_bend_dir; %random values using uniform distribution
22
23 cst = actxserver('CSTStudio.application');
24 mws = cst.invoke('Active3D');
25
26 %% Prepare WCS/axis
27 mws.invoke('AddToHistory', 'local coords','WCS.ActivateWCS "local"');
28 mws.invoke('AddToHistory', 'rotate coords','WCS.RotateWCS "v",
29     "-(90.0)");
30
31 %% Bend trunks
32 if n_S_trunks*n_S_layers~=0
33     for j=1:n_S_layers
34         for i=1:n_S_trunks
35
36             if i~=1
37                 mws.invoke('AddToHistory', sprintf('move coords%i%i'
38     ,j,i),sprintf('WCS.MoveWCS "global", "%s", "%s", "%f"',shift_x,
39     shift_y,rnd_bend_locS(count)-rnd_bend_locS(count-1)));

```

```

34         mws.invoke('AddToHistory', sprintf('rotate coords%i%
i',j,i),sprintf('WCS.RotateWCS "u", "%f"',(rnd_bend_dirS(count)-
rnd_bend_dirS(count-1))));
35         else
36             mws.invoke('AddToHistory', sprintf('move coords%i%i'
,j,i),sprintf('WCS.MoveWCS "global", "0.0", "0.0", %f',
rnd_bend_locS(count)));
37             mws.invoke('AddToHistory', sprintf('rotate coords%i%
i',j,i),sprintf('WCS.RotateWCS "u", "%f"',(rnd_bend_dirS(count))
));
38         end
39
40         for k=1:inner_layers
41             mws.invoke('AddToHistory', sprintf('Bend%i%i%i',j,i,
k),[...
42                 sprintf('With Bending\n') ...
43                 sprintf(' .CylindricalBend "component_main/
componentSL%i/componentS%i:small_trunk%i", "False", "0", "3500%i
", "-1"\n',j,i,k,rnd_bend_factorS(count)) ...
44                 sprintf('End With')]);
45         end
46
47         count=count+1;
48         shift_y='0';
49         shift_x='dx1';
50     end
51     shift_y='dy1';
52     shift_x=sprintf('-dx1%i',n_S_trunks-1);
53     if i ~= n_S_trunks || j ~= n_S_layers
54         mws.invoke('AddToHistory', sprintf('adjust coords%i%i',j
,i),sprintf('WCS.MoveWCS "global", "%s", "%s", %f',shift_x,
shift_y,-rnd_bend_locS(count-1)));
55     end
56 end
57 end
58
59 %% Reset vars
60 % count=1;
61 shift_x=sprintf('-dx1%i',n_S_trunks-1);
62 mws.invoke('AddToHistory', sprintf('adjust coords'),sprintf('WCS.
MoveWCS "global", "%s", "dy1", %f',shift_x,-rnd_bend_locS(end)));
63 mws.invoke('AddToHistory', 'local coords','WCS.ActivateWCS "global"')
;
64 end

```

Listing A.4: Function to bend trunks.

This page is intentionally left blank.



RECORDED STATS OF WOODEN POLES

---

Presented in Table 15 are the stats of a batch of thirty poles where height and various radial sections radius are recorded.

Table 15: Height assessment over a batch of thirty wooden poles.

Trunk n <sup>o</sup>	Radius (cm)			Height (cm)
	Top	Middle	Bottom	
1	5.3	5.6	5.7	224.0
2	5.6	5.8	6.4	233.0
3	6.0	5.9	6.2	226.0
4	5.4	5.7	5.9	223.0
5	5.7	5.6	6.5	235.0
6	5.3	5.4	5.9	230.0
7	5.4	5.3	5.5	225.0
8	6.0	6.2	6.4	226.0
9	5.6	5.7	6.5	228.5
10	5.7	6.4	6.0	222.5
11	6.2	5.9	6.0	225.5
12	6.0	6.2	6.4	226.0
13	5.6	5.9	6.3	228.0
14	5.4	5.6	5.9	222.5
15	5.6	6.0	6.8	222.5
16	5.6	5.7	6.4	229.0
17	5.6	5.9	6.5	228.5
18	5.7	6.2	6.4	228.5
19	5.4	5.7	5.9	224.0
20	5.7	5.7	6.4	232.0
21	5.4	5.9	6.0	220.5
22	5.4	5.7	6.0	227.0
23	6.0	5.6	6.2	229.5
24	5.4	5.6	6.7	231.0
25	5.5	5.5	5.7	223.5
26	5.4	5.5	6.0	235.0
27	5.1	5.4	5.7	220.0
28	5.4	5.7	5.7	221.0
29	5.3	5.8	6.4	234.5
30	5.7	6.0	6.1	231.0
Average:	5.6	5.8	6.2	227.1

## FREE SPACE MEASUREMENTS

Measurements of free space in a multi-angular setting at commercial frequencies for barrier measurements data normalisation, presented in Figures 54 and 55.

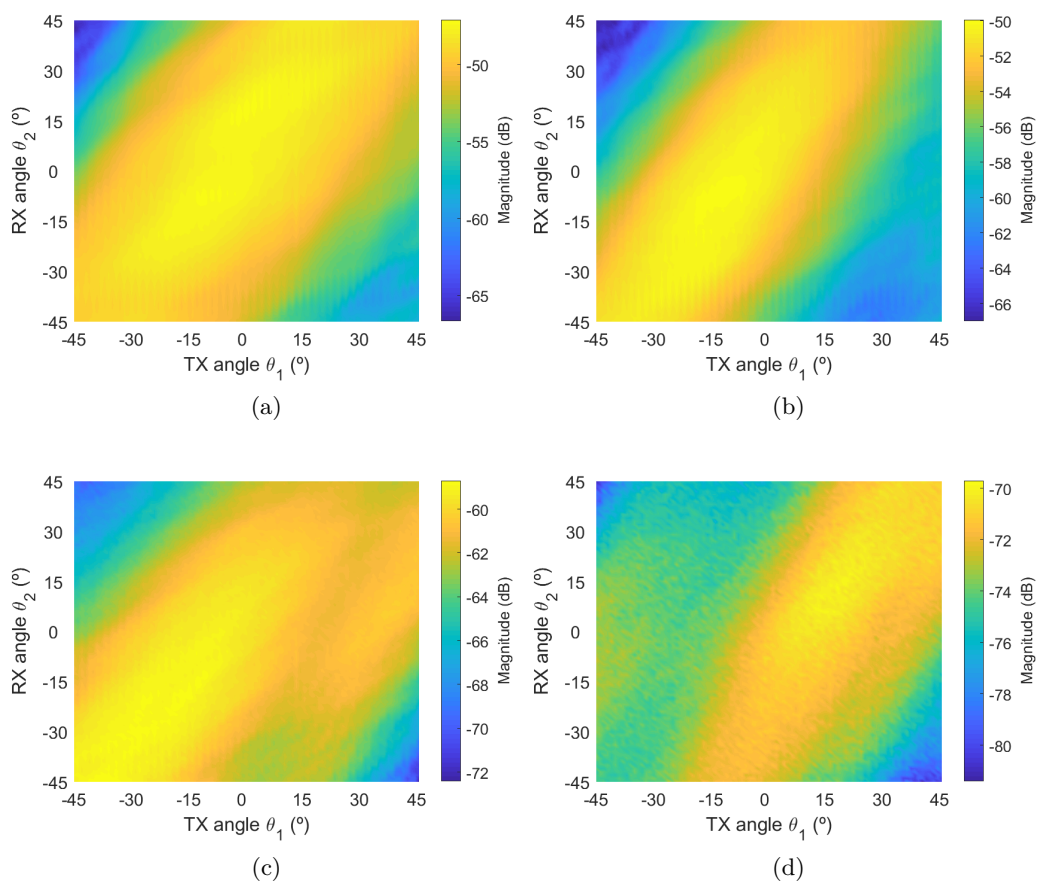


Figure 54: Free space measurement in a multi-angular setup with antennas horizontally polarised at 1.8 (a), 2.4 (b), 3.7 (c) and 5.9 GHz (d).

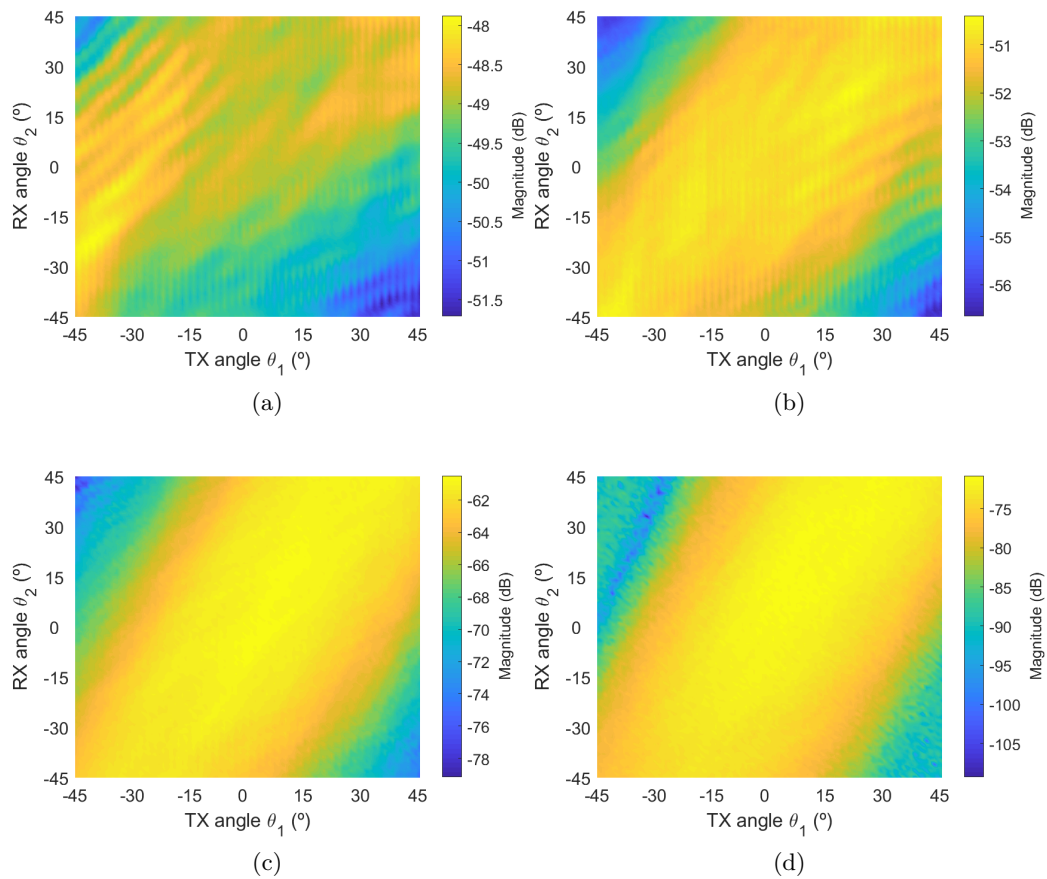


Figure 55: Free space measurement in a multi-angular setup with antennas vertically polarised at 1.8 (a), 2.4 (b), 3.7 (c) and 5.9 GHz (d).

NORMALISED BARRIER MEASUREMENTS

---

Normalised measurements with vertical and horizontal polarisation, spacing between centre of trunks from 160 to 200 mm, at the frequencies of 1.8, 2.4, 3.7 and 5.9 GHz presented in Figures [56](#), [57](#), [58](#) and [59](#), respectively.

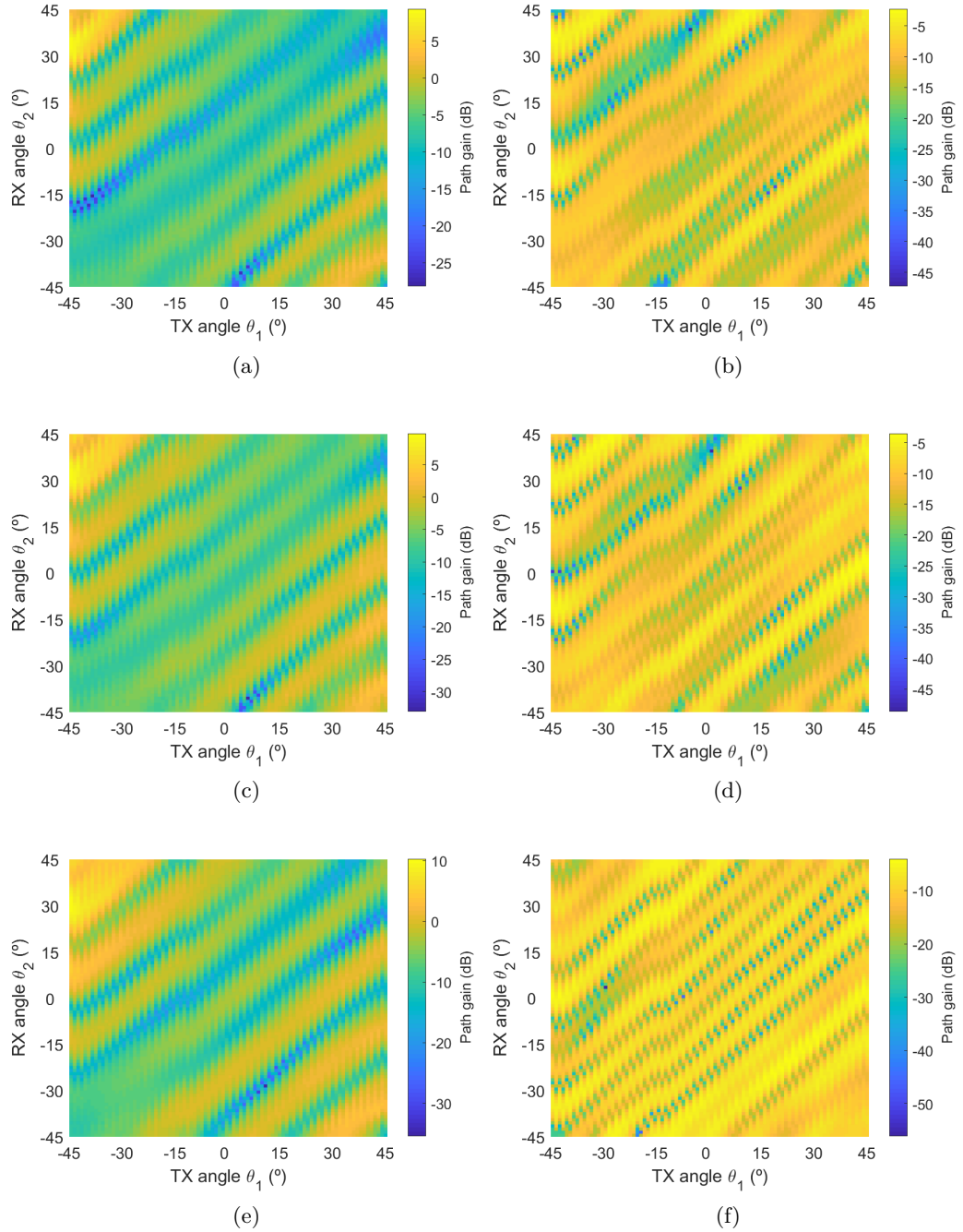


Figure 56: Graphs presenting normalised measurement results at 1.8 GHz with antennas horizontally polarised and spacing between centre of trunks of 160 (a), 180 (c) and 200 mm (e), and antennas vertically polarised with spacing of 160 (b), 180 (d) and 200 mm (f).

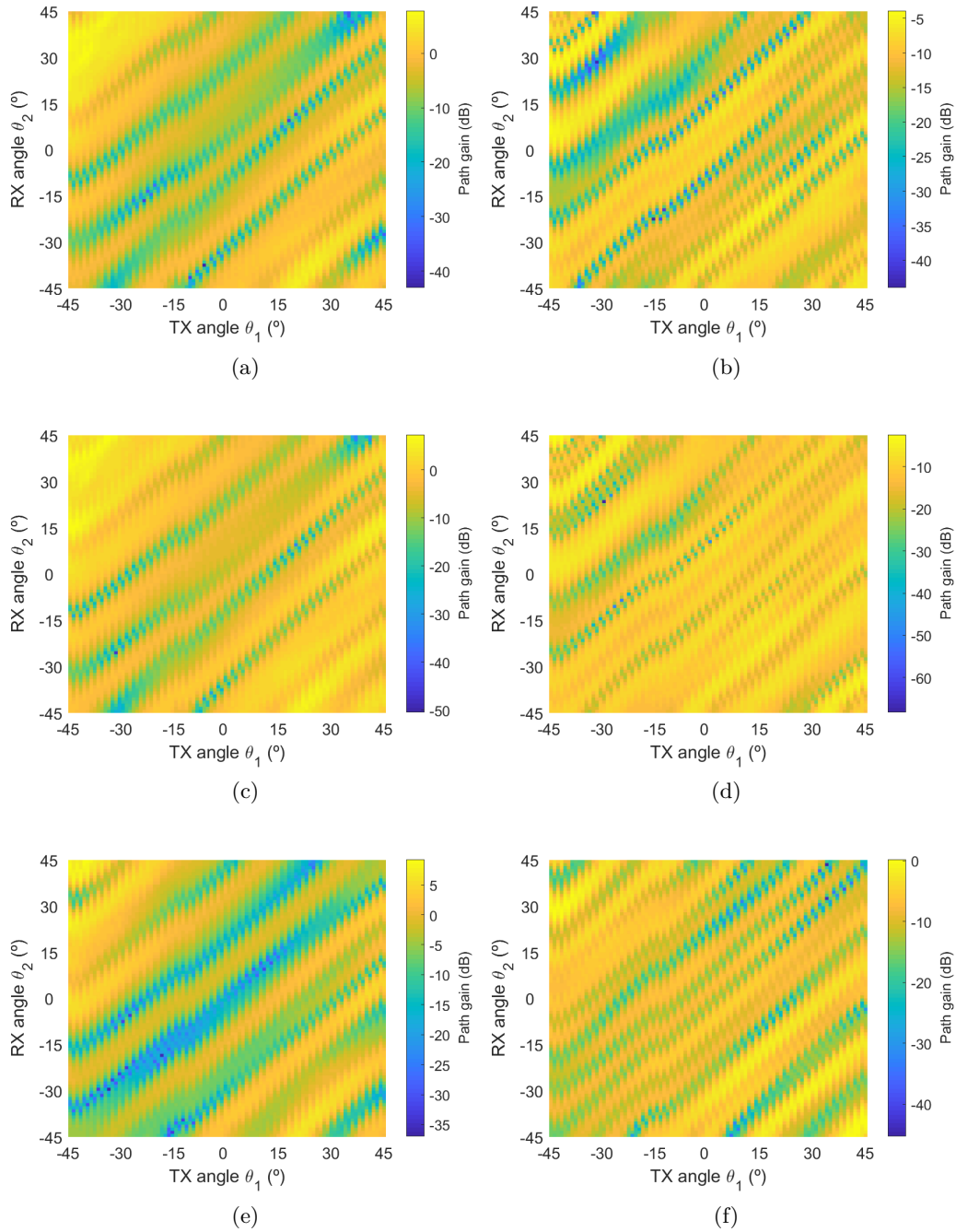


Figure 57: Graphs presenting normalised measurement results at 2.4 GHz with antennas horizontally polarised and spacing between centre of trunks of 160 (a), 180 (c) and 200 mm (e), and antennas vertically polarised with spacing of 160 (b), 180 (d) and 200 mm (f).

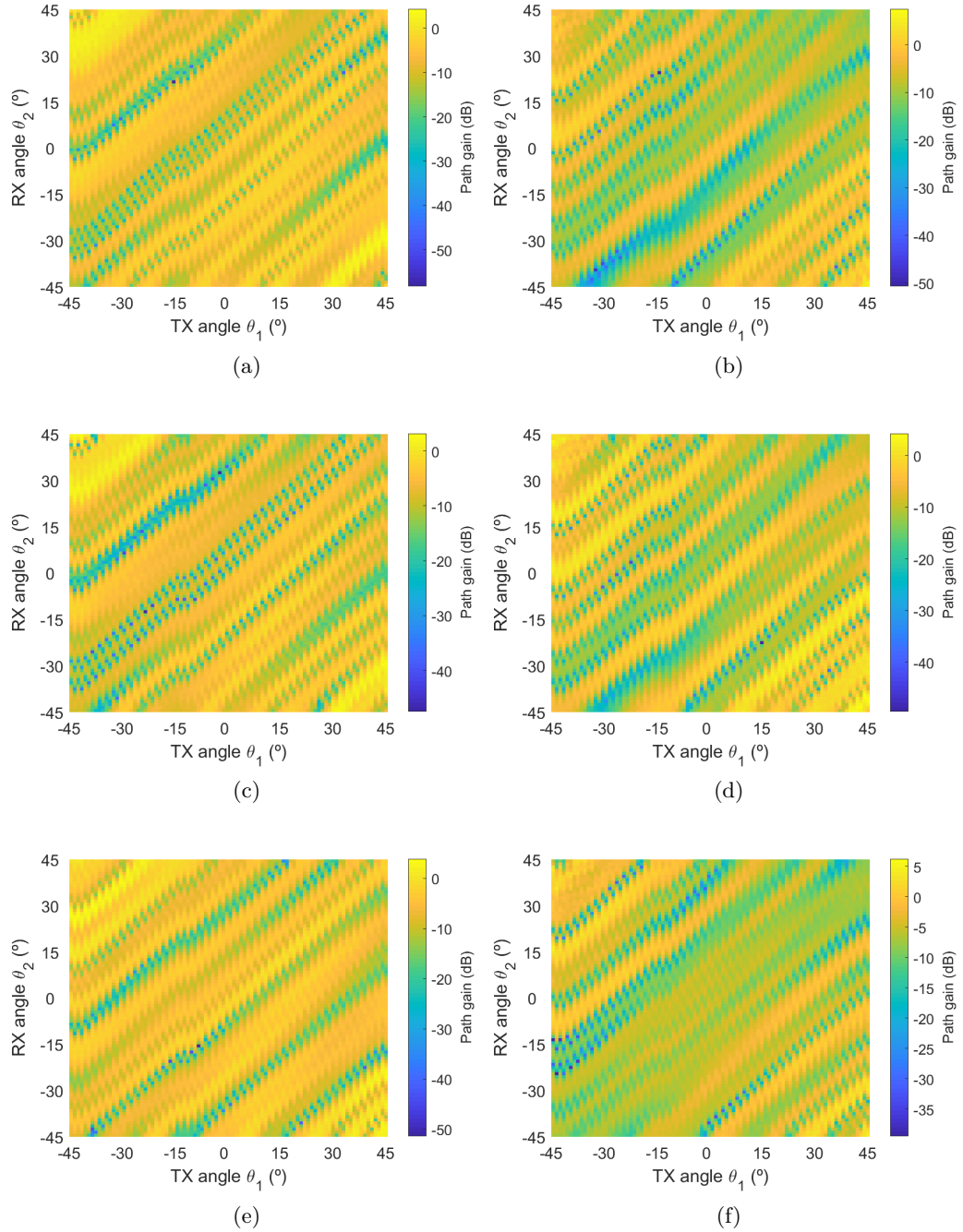


Figure 58: Graphs presenting normalised measurement results at 3.7 GHz with antennas horizontally polarised and spacing between centre of trunks of 160 (a), 180 (c) and 200 mm (e), and antennas vertically polarised with spacing of 160 (b), 180 (d) and 200 mm (f).



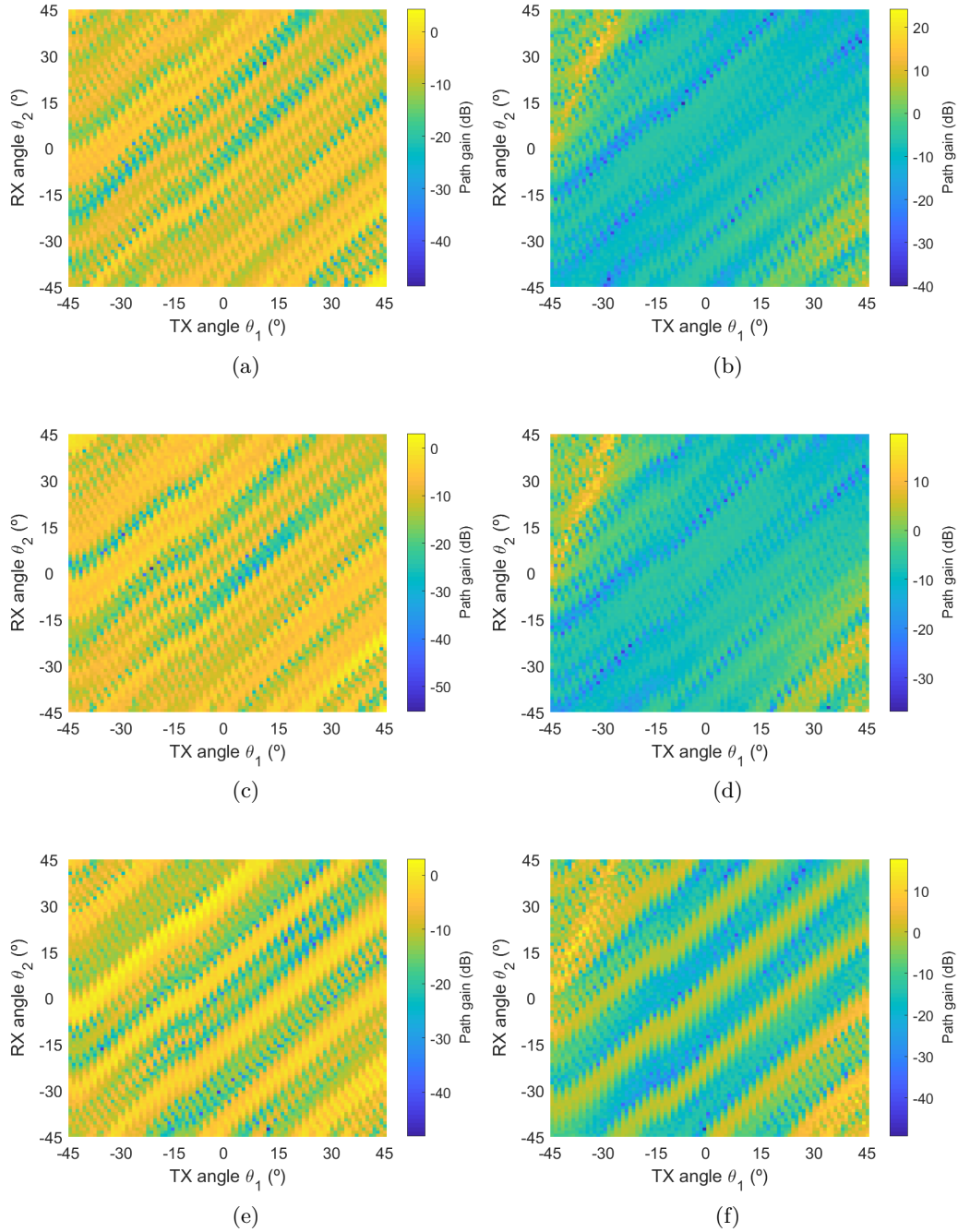


Figure 59: Graphs presenting normalised measurement results at 5.9 GHz with antennas horizontally polarised and spacing between centre of trunks of 160 (a), 180 (c) and 200 mm (e), and antennas vertically polarised with spacing of 160 (b), 180 (d) and 200 mm (f).

This page is intentionally left blank.

## DECLARATION

---

Declaro, sob compromisso de honra, que o trabalho apresentado nesta dissertação, com o título “*Electromagnetic Log Shield for Roadside Application*”, é original e foi realizado por Bruno Alves Tribovane (2182462) sob orientação de Rafael F. S. Caldeirinha ([rafael.caldeirinha@ipleiria.pt](mailto:rafael.caldeirinha@ipleiria.pt)).

*Leiria, December of 2021*

---

Bruno Alves Tribovane